

Politecnico di Torino

Politecnico di Torino

Master of Science in Energy and Nuclear Engineering

Enhancing PED evaluation through a novel discretization approach in UWG-Based microclimate modeling

Supervisor: Prof. Andrea Lanzini

Co-supervisor: Prof. Daniele Salvatore Schiera

Candidate: Caterina Greco

Student ID: 317597

March 2026

"There are two paths you can go by, but in the long run
There's still time to change the road you're on"

Stairway to Heaven – Led Zeppelin

Abstract

Achieving climate neutrality in urban areas requires tools capable of representing the interaction between the building envelope, energy systems, and the local microclimate. Although microclimatic phenomena, such as the urban heat island (UHI), are recognized for their influence on cooling loads and system performance, their explicit representation remains limited in energy simulation applications. The Urban Weather Generator (UWG), a model based on a Concentrated Parameter (CP) network, represents a computationally efficient alternative to high-fidelity numerical models, such as CFD simulations, for urban climate analysis. However, its ability to represent spatial heterogeneity remains a critical issue. This thesis analyzes the impact of spatial discretization on model accuracy, comparing a regular 200×200 meter grid-based subdivision of the domain with a discretization based on morphological blocks. The methodology is applied to a case study on a Positive Energy District (PED) in the city of Turin, using high-resolution geometric data from the Topographic Database (DBTRE). This allows for an explicit characterization of buildings and vegetation (trees and grass), as opposed to aggregated fractional estimates. Anthropogenic heat from traffic is estimated using an empirical regression between sensible heat fluxes and NO_2 concentrations at ground level, used as a proxy for vehicle emissions. The thermophysical parameters of buildings are calibrated on Italian building archetypes, showing improved performance compared to the standard DOE models commonly used in UWG. Validation is conducted by comparison with data from the ARPA Piemonte Consolata station over the full year 2024. Discretization based on morphological blocks achieves an annual RMSE of 1.114 K, compared to 1.182 K for the regular grid, corresponding to a 5.77% reduction in error. The average positive bias ($MBE = +0.263$ K) is consistent with the altitude difference between the measurement point and the simulated pedestrian level, highlighting the sensitivity of the model in representing vertical temperature gradients. At the district scale, the spatial standard deviation of UHI intensity is more than twice as large in the grid configuration ($\sigma_G = 0.162$ K) than in the morphological block approach ($\sigma_{MB} = 0.074$ K), with a monthly Dispersion Ratio consistently exceeding 1.8. Point-level biases between the two methods reach up to 0.774 K in cells where geometric aliasing distorts the estimated surface coverage and anthropogenic heat flux. This study validates the use of morphological blocks as the preferred spatial unit, offering the best compromise between physical rigour and computational burden.

Contents

Introduction **8**

1 Positive Energy Districts: The New Urban Paradigm **12**
1.1 From Zero Energy Buildings to Positive Energy Districts 12
1.2 The Functional Triad of PEDs 15
1.3 PEDs as building blocks for climate neutrality and sustainability . . 17

2 Literature review **18**
2.1 The Role of Urban Microclimate and Heat Island Effects 18
2.1.1 The UHI phenomenon and its quantification 18
2.1.2 UHI impact on energy modelling at the district scale 20
2.2 The Urban Weather Generator (UWG) 20
2.2.1 Physical architecture and operating modules 20
2.2.2 Validation and sensitivity analysis 26
2.2.3 Structural limitations and research frontiers 27
2.3 Modelling Approaches: Spatial Discretization Scale 28
2.3.1 The spatial scale problem 28

3 Aim and scope **30**

4 Methodology **32**
4.1 Data processing and pre-processing 32
4.1.1 Loading and geometric standardisation 33
4.1.2 Processing of building data 33
4.1.3 Processing of urban vegetation 39
4.1.4 Final validation and output 39
4.2 Spatial partitioning and calculation of metrics 45
4.2.1 Spatial Partitioning Strategies 45
4.2.2 Calculating metrics for Spatial Units 50

4.3 Microclimatic simulation with UWG 57
4.3.1 Generation of Rural Meteorological Dataset 57
4.3.2 Multi-Prototype Configuration for Mixed-Use Districts . . . 58
4.3.3 Configuration and calibration of simulation parameters . . . 59
4.3.4 Synthesis of the Simulation Setup 60

5 Result and Model Evaluation **63**
5.1 Model Validation: Comparison with Field Measurements 63
5.1.1 Monthly Statistical Performance: Grid vs. Morphological Discretization 65
5.1.2 Representative Day Analysis and Extreme Event Validation 69
5.2 Urban Heat Island Mapping and Spatial Characterization 72
5.2.1 Quantification of Discretization Bias 77
5.3 Sensitivity Analysis: Microclimate Drivers across Urban Archetypes 82

6 Conclusion **89**

Bibliography **93**

A Supplementary Material and Tabular Data **98**
A.1 Urban Heat Island Evidence 98
A.2 Mapping and Discretisation of the Urban Fabric 100
A.3 Validation Results 102
A.4 Mapping of urban heat island 103
A.5 Thermal Sensitivity Data 104
A.5.1 Summer Schedule (28 July) 104
A.5.2 Winter Schedule (15 December) 106

List of Figures

1.1 Evolution of the concept from ZEB to PED. 14
1.2 Key functions of PEDs 16

2.1 Urban Heat Island effect overview. 19
2.2 Four coupling modules of UWG 21

4.1 Distribution of building prototype across the study area. 41
4.2 Frequency distribution of building heights. 41
4.3 Spatial mapping of building prototypes. 42
4.4 Spatial mapping of building height. 43
4.5 Morphological map of the Turin PED area. 44
4.6 Grid discretization based on a 200x200 m resolution. 47
4.7 Morphological blocks discretization based on the urban fabric. . . . 49
4.8 Traffic Anthropogenic Heat Flux - Grid configuration. 55
4.9 Traffic Anthropogenic Heat Flux - Morphological Blocks configuration. 56

5.1 Spatial validation of the weather station location in the Consolata area. 64
5.2 Comparison of hourly RMSE and MBE across the simulation months for Grid (G) and Morphological Block (MB) configurations. 67
5.3 Monthly average hourly air temperature profiles: comparison between Grid (G), Morphological Block (MB), and observed ARPA data (Consolata). 68
5.4 Detailed validation of the Summer Heat Wave period (27–30 July 2024). 70
5.5 Detailed validation of the Winter Cold Pool period (14–16 December 2024). 71
5.6 Comparative UHI maps between G and MB. 73
5.7 Boxplot comparison of UHI: Grid vs Morphological Blocks. 75
5.8 Monthly UHI maps calculated via morphological blocks. 76

5.9 UHI Bias Analysis – Histogram and Spatial Distribution. 78
5.10 Detail of bias analysis for specific representative cells. 80
5.11 Pearson correlation matrix between morphological, radiative, and environmental parameters. 83
5.12 Monthly relative change in $\Delta UHI[\%]$ for four urban types and four control factors. 86

A.1 Experimental evidence of the UHI effect in Turin: hourly temperature comparison between urban (Consolata) and rural (Caselle) weather stations (Annual average). 99
A.2 Spatiotemporal heatmap of UHI intensity [K] in Turin, showing the hourly temperature delta between urban and rural stations across the months. 99
A.3 Grid discretisation based on a 200×200 m resolution. 100
A.4 Morphological blocks discretisation based on the urban fabric. . . . 101
A.5 Spatial mapping of the average annual UHI in the Core Area. . . . 103
A.6 Hourly thermal profile variations during the extreme heat event (July 28th). 105
A.7 Hourly thermal profile variations during the extreme cold event (December 15th). 107

List of Tables

2.1 Comparison of urban microclimate modelling approaches: trade-offs between spatial resolution, accuracy, and computational cost. 29

4.1 Classification of building stock based on construction period. 34
4.2 Mapping of DOE archetypes: dimensional thresholds and standard parameters. 36
4.3 Mapping by non-standard categories via thermophysical analogies. . 37
4.4 Surface albedo coefficients differentiated by construction period and use. 38
4.5 Summary of building metrics following the geometric dissolve procedure. 40
4.6 Internal load parameters calibrated by building prototype and construction era. 53
4.7 General simulation parameters and global physical constants set in the UWG model. 59
4.8 Building envelope thermophysical properties and infiltration rates stratified by construction era. 60
4.9 Synthesis of UWG simulation parameters: inputs, sources, and outputs. 62

5.1 Hourly validation metrics for the G and MB configurations. Values relative to ARPA 2024 measurements. 66
5.2 Comparative UHI Statistics (Core Area): Grid (G) vs Morphological Block (MB). 73
5.3 Full monthly UHI statistical metrics and Dispersion Ratio comparison (Core Area). 74
5.4 Ranking of the highest UHI Discrepancies (Top Cells by Absolute Bias). 79
5.5 Morphological and energetic drivers of overestimation in Cell 50. . . 81
5.6 Spatial smoothing effect in Cell 34: masking of local thermal hotspots. 81

5.7 Classification of Urban Archetypes based on Density and Height quartiles. 82
5.8 Morphological characteristics of the four selected urban archetypes. 82
5.9 Sensitivity Analysis: Stress Test Scenarios and Parameters. 84
5.10 Seasonal comparison of UHI intensity by morphological archetype (Baseline). 85
5.11 Summary of dominant factors impacting UHI intensity per urban archetype. 87
5.12 Comparison of thermal dynamics and critical factors between summer and winter regimes. 88

A.1 MAUP Validation results: Monthly and annual statistical comparison (RMSE and MBE) between morphological blocks (MB) and three grid-based discretizations (NC, 200m, 500m). 102
A.2 Thermal sensitivity analysis summary (July 28th - Extreme Heat). . 104
A.3 Thermal sensitivity analysis summary (December 15th - Extreme Cold). 106

Introduction

The European energy transition is unfolding within a global context defined by the **2030 Agenda** of the United Nations, which represents a significant universal political commitment on the part of all member states to pursue the **17 Sustainable Development Goals** (SDGs), defined in 169 targets to be accomplished through national programs and international cooperation actions. The SDGs have been devised to address the systemic barriers impeding international development, encompassing inequalities, unsustainable production and consumption systems, inadequate infrastructure, the absence of decent work, climate change, and the degradation of ecosystems and biodiversity [1]. Among these, SDG 11 (**Sustainable cities and communities**) and SDG 13 (**Climate action**) provide guidelines for shifting urban policies towards more resilient, low-emission models.

Although urban areas cover only 3% of the Earth's surface, they are responsible for a significant proportion of global energy consumption and climate-changing emissions. They are associated with around 75% of CO_2 emissions and 60-80% of primary energy consumption [2]. This imbalance can be attributed to the aggregation of population, economic activities, and infrastructure within urban systems, thereby establishing cities as pivotal nodes within the global energy and climate systems. Focusing on the European context, the building sector is responsible for approximately 40% of final energy consumption and 36% of total greenhouse gas emissions, confirming its role as a central pillar of energy transition policies [3]. Achieving climate goals, therefore, necessitates a fundamental rethinking of the design, management and integration of buildings into urban systems.

At the European level, this vision translates into a structured regulatory and strategic framework. Key initiatives include the SET-Plan (**Strategic Energy Technology Plan**), which coordinates technological priorities with the European **Green Deal**, net-zero industry legislation, and the **REPowerEU** plan [4]. In the Communication for an Integrated Plan, ten priority actions have been identified to accelerate the transformation of the energy system, which foresee the synergetic

action of several European countries, private actors and the European Commission itself. In particular, Action 3 aims to "**Create technologies and services for smart homes that offer smart solutions to energy consumers**". This action has been divided into two separate subactions [5]:

- Smart solutions for energy consumers (3.1);
- Smart Cities and Communities (3.2).

Subaction 3.2 introduces the innovative concept of **Positive Energy Districts** (PEDs), i.e., energy-efficient and energy-flexible urban neighbourhoods or areas of connected buildings and facilities, that produce local renewable energy, achieve net zero greenhouse gas emissions, and actively contribute to overall climate neutrality [6].

The Implementation Plan for Sub-Action 3.2 draws inspiration from the European Innovation Partnership on Smart Cities and Communities, with specific reference to the Positive Energy Blocks initiative and the concepts of zero-energy and zero-emission districts. The strategic objective of the Plan, coordinated by the **Temporary Working Group** (TWG) 3.2 established in April 2017, is to create at least 100 PEDs in Europe, initially by 2025, in line with the objectives of the Paris Agreement and the European directives on **energy efficiency** (EED) and the **energy performance of buildings** (EPBD). In this context, PEDs are crucial for achieving climate neutrality. This is understood to mean optimising not only the local subsystem but also the overall energy system, and it is achieved through an integrated approach. However, climate neutrality requires synergistic actions to mitigate and adapt to climate change, increasing the district's resilience and protecting the urban environment. The combination of increasing urbanization and the expected effects of climate change makes anthropized areas more vulnerable. In this scenario, the resilience of a PED must extend far beyond mere energy security; districts must be designed to respond to specific environmental impacts such as extreme weather events and rising sea levels [6].

A critical factor is local microclimatic change, in particular the **Urban Heat Island** (UHI) phenomenon. The UHI is characterized by significantly higher ambient temperatures in dense urban areas than in surrounding rural areas. In addition to serious impacts on public health and the vulnerability of the urban population [7], this phenomenon triggers negative feedback on the energy system. Rising outdoor temperatures reduce the operating efficiency of refrigeration machines (decrease in COP) and exponentially increase the demand for cooling energy [8]. From

this standpoint, it is evident that conventional planning methodologies, predicated exclusively on standard meteorological data – derived predominantly from rural airport stations – are inadequate in representing the actual thermal conditions of the built environment. To manage these complexities, research is moving towards the adoption of **Urban Building Energy Modelling** (UBEM) and, more recently, urban Digital Twins. These tools aim to integrate geographical and physical data to simulate the energy behaviour of districts. In this context, the **Urban Weather Generator** (UWG) acts as a microclimatic calculation engine that allows macro-scale meteorological data to be "urbanised", enabling the typical effects of the urban context, the radiative properties of materials and anthropogenic heat to be computed. The city of Turin is a relevant case study at European level, as it participates in various initiatives related to PEDs. On the one hand, the city is the Lighthouse City of the **TIPS4PED** project [9], which aims to develop advanced urban planning tools and Digital Twins to support local administrations in the design, implementation and replicability of PEDs. The project focuses on an area of approximately 260,000m^2 centred around the campus of the Polytechnic University of Turin, integrating public buildings, university residences and energy infrastructure such as the district heating network. Conversely, Turin is engaged in the **EDUPED (Education for Positive Energy Districts)** initiative [10], which employs a research-oriented, urban morphology-based systemic approach to address the energy transition of university campuses. In this context, the campus is analysed as a complex urban system, providing an ideal setting for the validation of energy redevelopment models and intervention strategies that can be replicated on a neighbourhood scale. The coexistence of initiatives such as TIPS4PED and EDUPED highlights how Turin is addressing the issue of PEDs through a multi-level strategy that combines advanced urban planning, technological experimentation and socio-behavioural aspects [11]. This approach consolidates the city's role as a reference laboratory for energy transition and provides an ideal context for the development and validation of accurate energy-environmental models — including microclimatic modelling, which is the central objective of this thesis.

The work is structured as follows:

- **Chapter 1** analyses the evolution of the Positive Energy Districts paradigm and existing models;
- **Chapter 2** presents a literature review focused on the relationship between urban microclimate and energy modelling, exploring the functioning of the Urban Weather Generator model;

- **Chapter 3** defines the objectives and scope of the thesis;
- **Chapter 4** describes the methodology developed, from data pre-processing to microclimate simulation;
- **Chapter 5** illustrates the results obtained and discusses the main simulation outputs.

Chapter 1

Positive Energy Districts: The New Urban Paradigm

1.1 From Zero Energy Buildings to Positive Energy Districts

The evolution of definitions related to energy efficiency in buildings and urban areas shows a progressive extension of the **scale of reference**, starting from individual buildings up to urban districts (see Figure 1.1). The concept of PED, in fact, derives from the previous concepts of **Zero Energy Buildings** (ZEB), **Energy Positive Neighbourhoods** (EPN), **Positive Energy Blocks** (PEB), and **Energy Neutral Districts** (END), with which it shares parameters such as geographical boundary, balancing period, interaction with the electricity grid, and supply method [11]. Initially, the focus was on Zero Energy Buildings (ZEB), buildings capable of producing as much energy as they consume over the course of a year, with different interpretations related to energy metered at the site or source, as well as emissions or energy costs. Torcellini et al. [12] distinguished four interpretations based on the accounting boundary:

1. **Net Zero Site Energy**,a building that produces as much energy as it uses annually when accounted for at the site;

2. **Net Zero Source Energy**, a building that produces at least as much energy as it uses annually when accounted for at the source, considering primary energy conversion factors and grid losses;

3. **Net Zero Energy Emissions**, a building that produces at least as much emissions-free renewable energy as it uses from emissions-producing energy sources, focusing on carbon neutrality;

4. **Net Zero Energy Cost**, a building that receives as much financial credit for exported energy as it is charged on utility bills, achieving economic balance.

Among these, the site-based definition is the most verifiable through on-site measurements, while source, emissions, and cost-based definitions depend on external factors such as grid carbon intensity and energy prices, which vary geographically and temporally.

Later, the concept of ZEBs was expanded to the **Life Cycle Zero Energy Building** (LC-ZEB), which encompasses the energy incorporated into the building and its components throughout its lifetime [13]. An LC-ZEB is defined as a building in which the primary energy used in the building and the energy embodied in the materials and systems over the life of the building is equal to or less than the energy produced by its renewable energy systems installed in the building during its useful life.

Subsequently, research was shifted to larger scales such as neighborhoods, giving rise to the concepts of **Energy Positive Neighborhoods** (EPN) and **Positive Energy Blocks** (PEB). The first consider not only the energy of buildings but also that of complementary infrastructures and services, such as waste and water management, parks, open spaces and public lighting, as well as transport demand [14]. PEBs, on the other hand, are defined as a set of at least three neighbouring buildings with an average positive annual energy balance between them, allowing for the inclusion of infrastructure and systems between buildings [15]. The PEB concept introduced the notion of energy sharing at the block scale, where surplus energy from one building can compensate for deficits in adjacent buildings, thereby reducing the need for individual building self-sufficiency.

Finally, the focus shifted to the urban district scale, with the introduction of the concepts of **Energy Neutral Districts** (ENDs) and **Positive Energy Districts** (PEDs). ENDs, i.e., districts where no net import of energy from outside is required on an annual basis, involve the interaction of a larger number of buildings, along with the interaction between users, energy networks, and ICT systems, thus promoting a more integrated and holistic approach to energy management [16]. PEDs share many of the structural and functional characteristics of ENDs, but differ in the introduction of the concept of "positive energy", which remains ambiguous and

undefined in the literature [11]. The term "Positive Energy District" consists of two key elements:

- *Positive Energy*, which can indicate a surplus of renewable energy produced over that consumed in a given period, or, in more recent acceptations, a climate neutrality in terms of net CO_2 emissions, achieved through the exclusive use of renewable sources [5];
- *District*, which refers to an urban area larger than a city block or neighbourhood, as an evolution of the previous concepts of PEBs and EPNs. However, empirical evidence suggests that the term should not be rigidly tied to a specific scale—successful implementation cases range from small neighbourhoods to entire islands [11].

The most recent definition from the PED FRAMEWORK 3.0 [6] describes a PEDs as an " energy-efficient and energy-flexible urban neighbourhoods or areas of connected buildings and facilities, that produce local renewable energy, achieve net zero greenhouse gas emissions, and actively contribute to overall climate neutrality".

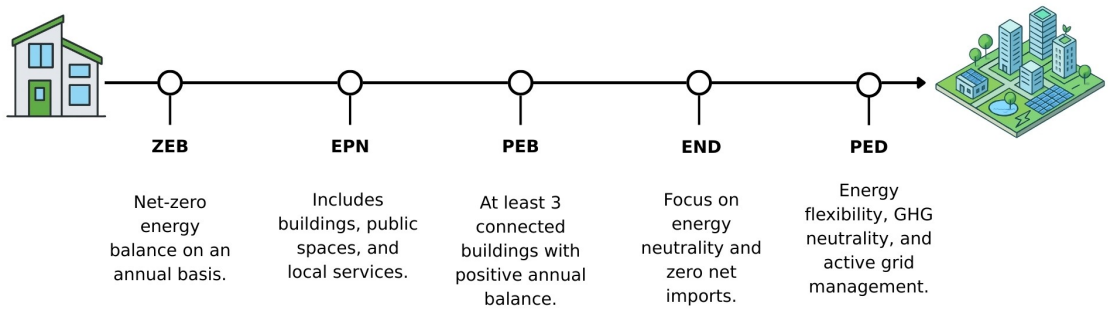


Figure 1.1: Evolution of the concept from ZEB to PED.

Despite the variety of terminologies, PED-related concepts share four consistent defining elements [11]:

- **Geographical Boundary**, the physical area (block, district, or island) treated as a single functional unit;
- **State of Interaction with an Energy Grid**, distinguishing between off-grid (autonomous) and on-grid (connected) systems;

- **Energy Supply Method**, Differentiating between on-site generation (within the building footprint or site) and off-site generation (renewable energy sources located outside the defined boundary but owned or contracted by the district);

- Balancing Period, the timeframe for the energy balance, typically annual to account for seasonal variations.

These defining elements provide a framework for understanding the progression from building-scale ZEBs to district-scale PEDs, reflecting an increasing recognition of the importance of scale, interaction, and temporal dynamics in achieving energy and climate goals. More recently, during a workshop on PED definitions organised by the European Energy Research Alliance (EERA) within the joint Smart Cities programme, three PED reference models were developed: autonomous, dynamic and virtual [17].

The **autonomous PED** is a district with well-defined geographical boundaries and is completely energy self-sufficient. In particular, it can meet its energy demand only through energy produced locally from renewable sources, with the possibility of exporting excess energy produced to other PEDs and electricity and district heating networks. However, it is not allowed to import energy from the electricity grid or from external district heating/gas networks.

In the **dynamic PED**, there is a bidirectional exchange of energy with other PEDs, as well as with the electricity grid and external district heating/gas networks. The import from outside can take place provided that the annual energy balance is positive, i.e. the district exports more energy than it imports during the year.

The **virtual PED** also has the possibility to operate outside the geographical limits of the district, with the opportunity to exploit more renewable sources and storage systems. Once again, the annual balance must be positive, i.e. the combined annual output of virtual and local renewable systems must exceed the district's annual energy demand. Furthermore, the parts of the energy system operating outside the boundaries must still be owned by the district in order to be classified within the virtual PED category.

1.2 The Functional Triad of PEDs

The definition of PEDs does not merely establish geographical boundaries, but contextualises and presents a framework outlining their most important functions,

based on the economic, cultural and climatic diversity of the countries involved [18]. In this context, three key functions emerge (see Figure 1.2):

- **Energy efficiency function**. In order to maximise the use of available renewable energy sources, priority must be given to energy efficiency. The objective is to reduce energy consumption within the district by balancing the needs of the different sectors.

- **Energy production function**. A PED should base its production exclusively on renewable energy sources. Although the availability of such sources is highly dependent on local and regional conditions, the exclusive use of renewable energy contributes significantly to the reduction of greenhouse gas emissions and ensures greater economic sustainability of the system.

- **Energy flexibility function**. PED must act optimally for the entire energy system, i.e. both on a district and regional scale. At the local level, a PED must be able to optimise its energy consumption through tools such as demand management, sector coupling and storage systems. At the same time, the district must maintain a structural flexibility to interact dynamically with the regional energy network, hence contributing to carbon neutrality and the overall stability of the energy system, also through the export of surplus renewable energy.

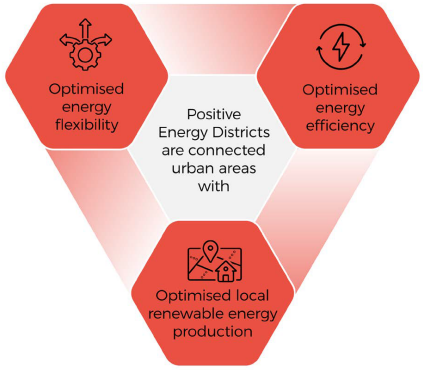


Figure 1.2: Key functions of PEDs [6].

1.3 PEDs as building blocks for climate neutrality and sustainability

Cities should be able to optimise different functions to find a balance that best represents the renewable energy resources available in the respective climate zone, take into account specific local ambitions and needs. When developing PEDs, it is crucial to consider the city's specific situation, such as urban density, building type and available local renewable energy resources. The recent political and technical evolution, codified in the PED Framework 3.0 [6], marks a significant shift in the definition of urban energy success. Moving away from a rigid "annual energy surplus," the new framework adopts a **mission-oriented** and **context-adaptive** approach. This evolution recognizes that in high-density or historical urban environments, the pursuit of energy positivity may conflict with other critical sustainability priorities:

- **Heritage Conservation**: Restrictions on renewable installations in historical centers limit local production potential and require non-invasive efficiency strategies.
- **Urban Form and Density**: Compact urban forms, while essential for reducing transport energy and land consumption, limit the available horizontal surfaces for energy generation relative to the total floor area.
- **Social Equity**: The focus on **"Energy Justice"** ensures that the transition remains affordable, accessible, and inclusive for all residents, avoiding the displacement of vulnerable populations due to rising energy costs.

Consequently, the framework redefines the role of a PED as its ability to provide a "**net positive contribution to regional or national decarbonization**" rather than achieving local self-sufficiency. In this systemic perspective, the **Energy Flexibility Function** becomes the primary tool for supporting the grid beyond the district's physical boundaries. To fulfill this mission, the Framework 3.0 explicitly integrates the concept of climate neutrality with that of climate resilience. It states that PEDs must be developed to adapt to the impacts of climate change, identifying the Urban Heat Island (UHI) and extreme weather events as primary risks to urban vulnerability. In this framework, the local microclimate is no longer a secondary environmental variable but a fundamental constraint for both the Efficiency and Flexibility functions.

Chapter 2

Literature review

Understanding the energy performance of cities requires bridging the gap between the thermal physics of individual buildings and the atmospheric processes governing the urban environment. Over the last two decades, energy modelling has progressively evolved from Building Energy Modelling (BEM), focused on single-building simulations, toward Urban Building Energy Modelling (UBEM), which enables the analysis of energy interactions across entire districts. Within this transition, the urban microclimate plays a fundamental role. In particular, the Urban Heat Island (UHI) phenomenon modifies the boundary conditions that determine building energy demand and therefore cannot be neglected in district-scale analyses.

This chapter focuses on the role of urban microclimate and the UHI effect. Particular attention is given to spatial discretization strategies used in urban energy modelling and to the Urban Weather Generator (UWG), one of the most widely adopted tools for integrating microclimatic effects into UBEM workflows. The review concludes by identifying the research gap addressed in this thesis.

2.1 The Role of Urban Microclimate and Heat Island Effects

2.1.1 The UHI phenomenon and its quantification

The Urban Heat Island (UHI) refers to the temperature differential between urban areas and their rural surroundings (Figure 2.1). This phenomenon does not merely constitute an observable thermal variation, but represents a true energy driver capable of significantly altering the heating and cooling demand of buildings. The

UHI is generated by the combination of multiple factors: the radiative and thermal properties of urban materials (roads, roofs, facades), the reduction of ventilation due to the urban canyon effect, the release of anthropogenic heat from HVAC systems and vehicular traffic, and the reduction of evapotranspirative surfaces compared to rural territory.

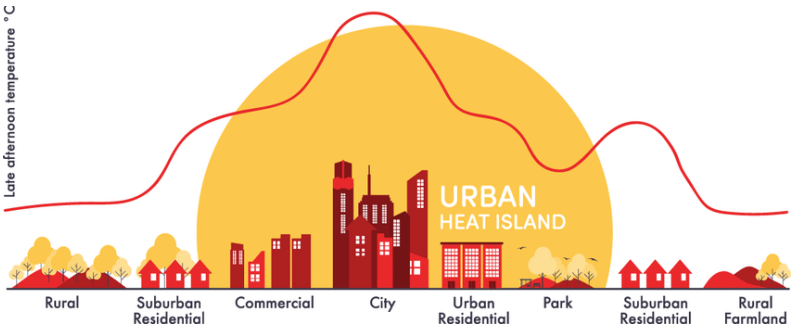


Figure 2.1: Urban Heat Island effect overview [19].

Calice et al. [20] quantified the feedback mechanism between HVAC systems and the urban atmosphere in Rome, showing that waste heat from air conditioning contributes up to 72% of the total UHI intensity during peak summer periods, increasing local temperatures by up to $+1.7°C$. Salvati et al. [21] further confirmed this complex variability in the context of Barcelona, where urban density drastically alters energy demand. The study shows that UHI intensity presents a marked seasonal and temporal dependence: in winter it is more intense in the nocturnal hours (peaks up to $5.8°C$ in December in the Raval district), whilst in summer, due to the sea breeze effect, the nocturnal intensity decreases though maintaining significant peaks. At the microclimate scale, measurements in eight urban canyons in Barcelona reveal substantial variations between sites with differing morphological characteristics, showing that the UHI is not a homogeneous phenomenon even within the same city.

Sangiorgio et al. [22] developed a holistic index (IUHII) for the evaluation and mapping of UHI intensity, calibrated on 41 urban districts across 32 European cities. The relative importance analysis of parameters — conducted through the Analytic Hierarchy Process (AHP) — assigns the greatest weight to surface albedo (29%) and vegetation cover (21%), followed by population density (12%) and urban canyon characteristics.

2.1.2 UHI impact on energy modelling at the district scale

The need to incorporate the UHI effect into building energy modelling is documented by numerous studies demonstrating that the use of standard climate files measured at extra-urban stations introduces systematic errors. Palme and Salvati [23] propose a three-stage methodology for integrating urban microclimatic data into TRNSYS: (1) calculation of UHI intensity via UWG, (2) calculation of shadows generated by surrounding buildings, and (3) calculation of urban surface temperatures and fictive sky temperature for long-wave radiation exchange. Results obtained on four typified urban morphologies in Antofagasta (Chile) show that the sole inclusion of the UHI overestimates cooling loads in dense contexts, where the mutual shading effect partially compensates for the heat-island warming. Zhao et al. [24] develop an integrated framework to analyse the impact of urban form on energy consumption in five Chinese climate zones, using UWG for urban weather data generation and DesignBuilder for energy simulations. The framework distinguishes the direct effects of urban form (solar radiation, inter-building shading via IBE) from the indirect effects (UHI intensity), validating the models against an open-science dataset with measured consumption data. The results confirm that urban morphology has a direct and quantifiable impact on consumptions, with indirect UHI influence dominating energy demand in mild climates (up to 85% of total impact), making its correct quantification critical. Natanian et al. [25] confirm that, for the resilient design of PEDs, future high-spatial-temporal-resolution climate files are needed that integrate urban climate modelling (UCM) with building energy modelling (BEM), considering the urban microclimatic conditions often neglected in standard climate files. The adoption of static Typical Meteorological Year (TMY) data risks overestimating heating requirements and underestimating cooling requirements in climate change scenarios, making the transition to actual meteorological data a methodological priority for accurate PED evaluation.

2.2 The Urban Weather Generator (UWG)

2.2.1 Physical architecture and operating modules

The Urban Weather Generator (UWG), developed by Bueno et al. [26] at the Massachusetts Institute of Technology, currently represents one of the most consolidated tools for integrating urban microclimate into district-scale energy simulation models. Conceptually, the UWG was designed to overcome the computational burden of

CFD models, enabling the transformation of standard meteorological files (EPW), typically measured at extra-urban stations, into urbanised meteorological files that reflect the real thermal conditions of the project site. The software is based on a concentrated parameter approach (Resistance-Capacitance network) that solves the coupled energy balance between buildings and the urban atmosphere [26]. According to the narrative review, the power of the model lies in its four-module structure [26] (see Figure 2.2):

- **Rural Station Model** (RSM): analyzes reference station data to isolate natural sensible heat fluxes.
- **Vertical Diffusion Model** (VDM): models vertical heat exchange above the city.
- **Urban Boundary Layer** (UBL): calculates the air temperature above the urban canopy, considering the effect of advection and atmospheric stability.
- **Urban Canopy and Building Energy Model** (UC-BEM): this is the core module that simulates the interaction between road surfaces, building facades, and HVAC systems, capturing the anthropogenic heat that fuels the Urban Heat Island.

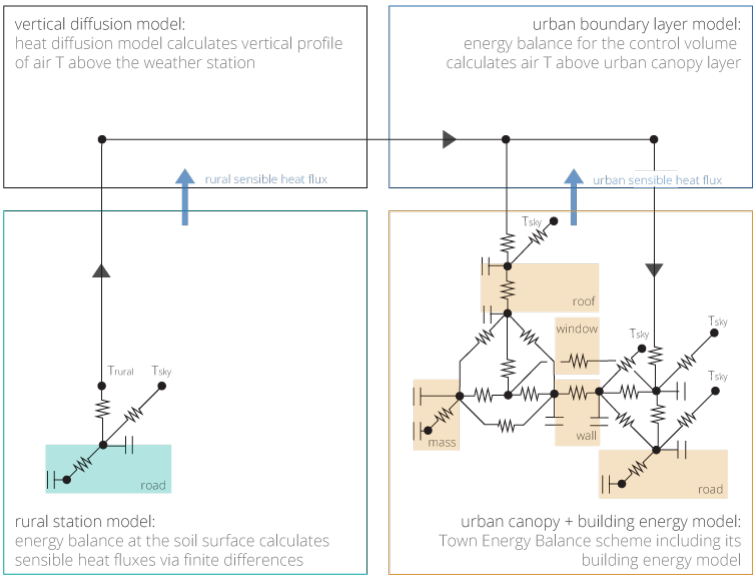


Figure 2.2: Four coupling modules of UWG [27].

RSM

The RSM is a module that calculates sensible heat fluxes at the soil surface based on hourly meteorological values measured at the rural site. These fluxes are subsequently introduced into the VDM and UBL modules. The soil is discretised into layers, and the process of heat accumulation and release is described by the transient heat diffusion equation:

$$d_1(\rho c)_1 \frac{\partial T_1}{\partial_t} = C_{1,2}(T_2 - T_1) + Q_{surf} \tag{2.1}$$

For the first layer i, the following is derived:

$$d_i(\rho c)_i \frac{\partial T_i}{\partial_t} = C_{i,i+1}(T_{i+1} - T_i) + C_{i,i-1}(T_{i-1} - T_i) \tag{2.2}$$

For any intermediate layer n, the following is derived:

$$d_{n-1}(\rho c)_{n-1} \frac{\partial T_{n-1}}{\partial_t} = C_{n-1,n}(T_{deep} - T_{n-1}) \tag{2.3}$$

where

- d is the depth;
- ρc is the volumetric heat flux;
- T_i is the average temperature of the i-th layer;
- $C_{i,j}$ is the average thermal conductivity between the i-th layer and the j-th layer;
- Q_{surf} is the sum of the net surface radiation, sensible heat flux, and latent heat flux;
- T_{deep} is the annual average temperature of the site.

The radiative contribution is derived from measurements taken at the weather station, while the sensible heat flux is estimated using the convective heat exchange coefficient. The latent heat flux associated with the presence of vegetation, if any, is instead evaluated in a simplified form as a proportion of the absorbed shortwave solar radiation, in line with the accuracy requirements of the UWG model.

VDM

The vertical diffusion model estimates the vertical profiles of the potential temperature above the weather station by solving the equation that describes heat diffusion processes:

$$\frac{\partial\theta(z)}{\partial t} = -\frac{1}{\rho(z)}\frac{\partial}{\partial z}(\rho(z)K_d(z)\frac{\partial\theta(z)}{\partial z}) \tag{2.4}$$

where

- θ represents the latent temperature in the air;
- z is the vertical spatial component;
- ρ is the air density;
- K_d is the diffusion coefficient.

UBL

The UBL model employs a representative control volume within the urban boundary layer to estimate the air temperature above the urban canopy. The volume under consideration is delimited superiorly by the height of the boundary layer (z_i) and inferiorly by the blending height (z_r). The latter is defined as the height at which the effects of individual urban elements on vertical profiles and atmospheric flows are averaged on a horizontal scale. The model differentiates between daytime and nighttime conditions in the urban boundary layer, as well as between different advection mechanisms: those related to the action of geostrophic wind (forced regime) and those associated with urban breeze circulation, governed mainly by buoyancy processes. The energy balance is expressed as follows:

$$V_{cv}\rho c_v\frac{d\theta_{urb}}{dt} = H_{urb} + \int u_{ref}\rho c_p(\theta_{ref} - \theta_{urb})dA_f \tag{2.5}$$

where

- V_{cv} is the control volume;
- ρ is the air density;
- c_v is the specific heat ratio of air at a fixed volume;
- c_p is the specific heat ratio of air at a fixed pressure;

- θ_{urb} represents the average latent temperature in the control volume;
- H_{urb} is the sensible heat flux on the surface of the control volume;
- θ_{ref} represents the reference latent temperature outside the control volume;
- u_{ref} represents the reference air velocity;
- A_f represents the cross-sectional area of heat exchange between the control volume and the surrounding environment.

UC-BEM

The UC-BEM model is predicated on the TEB (Town Energy Balance) scheme and extends its formulation by integrating a building energy model (BEM) coupled with the urban canyon. As in the TEB, it is assumed that the air inside the urban canyon is well mixed, thus allowing the canyon to be represented as a single volume of air with uniform temperature and humidity. The model utilises meteorological data from the weather station, including solar radiation, precipitation, wind speed, and air humidity, as well as the air temperature above the urban canopy layer, which is calculated by the UBL model. The energy balance of the urban canyon is determined by

- the heat flows from walls, windows, and roads;
- the sensible heat exchange between the canyon air and the atmosphere;
- the heat flows due to exfiltration;
- waste heat from HVAC systems and other anthropogenic sources;
- the radiative exchange between the canyon air and the sky.

The energy balance of the canyon air can be expressed as follows:

$$\begin{aligned} V_{can}\rho c_v \frac{dT_{urb}}{dt} = A_w h_w(T_w - T_{urb}) + A_r h_r(T_r - T_{urb}) + A_r h_{rd,skr}(T_{skr} - T_{urb}) \\ + A_{win}U_{win}(T_{in} - T_{urb}) + V_{inf/vent}\rho c_p(T_{in} - T_{urb}) \\ + u_{ex}\rho c_p(T_{ubl} - T_{urb}) + H_{waste} + H_{traffic} \end{aligned} \tag{2.6}$$

where

- T_{urb} is the urban canyon air temperature;

- T_{in} is the indoor air temperature;
- T_{ubl} is the urban boundary layer air temperature above the urban canyon;
- T_{skr} is the effective temperature;
- $h_w, h_r, h_{rd,sky}$ are the heat exchange coefficients of walls, roads, and between the air in the urban canyon and the sky, respectively;
- V_{can} is the air volume of the urban canyon;
- U_{win} is the U value of the window;
- $V_{inf/vent}$ is the ventilation rate;
- H_{waste} is the sensible heat part of the waste heat flux released into the urban canyon by the air conditioning system;
- $H_{traffic}$ is the anthropogenic heat generated by traffic, etc.;
- u_{ex} is the convective exchange rate between the air inside the canopy and above the canopy.

A similar latent balance is solved to determine the moisture content of the air in the urban canyon, considering the latent heat flows from the atmosphere, urban surfaces, and buildings. The model operates under the assumption that, at each temporal interval, the humidity of the atmosphere above the urban canyon corresponds with the measurements obtained at the meteorological station. The external surface temperatures of walls, roads, and roofs are calculated by solving a surface energy balance similar to that adopted for rural soil. The boundary conditions to which this model is subject are consistent with those which apply to rural soil, and for walls and roofs, the internal boundary condition is represented by a heat flow provided by the building energy model (BEM). The calculation of waste heat flows is determined by the building's energy consumption and energy demand. In the context of cooling, the waste heat is derived from the sum of the energy absorbed by the HVAC system and the building's cooling demand.

A significant improvement to the original model was introduced by Bueno et al. [28] in the UBL sub-model that enabled the definition of a building usage distribution within each neighbourhood (e.g. 20% commercial, 60% residential without air conditioning), improving the estimate of sensible heat fluxes released into the

urban environment. Nakano et al. [29] developed a graphical interface for the UWG integrated into the umi plugin for Rhinoceros 3D, enabling automatic extraction of morphological parameters (site coverage, average building height, facade-to-site ratio) directly from the 3D model. This parametric integration transformed the UWG from a research tool to a decision-support tool in the urban design phase. He et al. [30], in their narrative review of UWG applications, confirm that the model is currently used across very different spatial and temporal scales — from the single building to urban agglomerations, from the hour to the decade — with applications ranging from urban thermal environment simulation to outdoor comfort analysis and building energy consumption estimation.

2.2.2 Validation and sensitivity analysis

UWG validation has been conducted on a significant number of cities in different climatic contexts: Basel and Toulouse [26], Singapore, Boston, Rome, Barcelona, Mendoza, Campinas, and Abu Dhabi. The general consensus in the literature indicates expected errors of approximately $1K$ in UHI intensity, with a tendency to overestimate urban temperatures in nocturnal hours and underestimate them in afternoon summer hours. Hamdi et al. [31] conducted an in-depth evaluation of the UWG on Toulouse, comparing model performance across three different LCZs during UHI-favourable days in August 2020. Results show that the best performance is obtained in the most urbanised area (Carmes: MBE = 0.02°C, RMSE = 1.73°C), whilst performance degrades significantly in less densely built areas (Compans-Cafarelli: RMSE = 2.35°C, MBE = 0.51°C). The Morris sensitivity analysis reveals that atmospheric parameters, particularly the nighttime urban boundary layer height and reference height, dominate model sensitivity, whilst surface parameters such as building density and facade-to-site ratio show much more limited influence. A direct consequence of these observations is that the spatial variation of UWG simulations is insignificant, since surface parameters have low influence — confirming that UWG performs better in densely constructed city centres. Boccalatte et al. [32] document an hourly RMSE in the range 1.0–1.6 K when applying the model to Geneva.

Salvati et al. [33] conducted a systematic sensitivity analysis on eight key UWG parameters applied to Mediterranean contexts (Rome and Barcelona). The results show that urban morphology — particularly the vertical-to-horizontal ratio (VtH) and site coverage (SC) — generates UHI intensity variations of up to 120%,

while waste heat from HVAC systems contributes approximately 72% of summer UHI intensity. Albedo and vegetation produce much more limited variations in Mediterranean conditions. Sangiorgio et al. [22] confirm the importance of albedo at the territorial scale (29% weight in the IUHII index), suggesting that the relative role of parameters depends strongly on the scale of analysis adopted.

2.2.3 Structural limitations and research frontiers

Despite its effectiveness and widespread use, the UWG presents structural limitations that the literature has progressively documented. The primary one is the assumption of well-mixed air in the urban canyon, which implies the impossibility of representing horizontal thermal gradients within the same simulation unit. This assumption, critically analysed by Saadatjoo et al. [34] in the context of a medium-height neighbourhood in Amman (Jordan), proves particularly inadequate below 15 m in height, where wind speed shows marked variability due to surrounding buildings and local geometry invalidates the standard convective heat transfer equations.

A second structural limitation concerns the vegetation module. The UWG models tree canopies exclusively as physical obstacles to radiation, without incorporating an active module for calculating the latent heat of evapotranspiration. This simplification — as will be shown in Chapter 5 — means that increasing green cover can paradoxically worsen the local UHI, particularly in low-density scattered configurations where the vegetation acts primarily as a long-wave radiation trap at night, without the compensating benefit of evaporative cooling. This limitation is also noted by He et al. [30] as one of the main challenges for future development of the model.

A third structural limitation regards spatial discretization: since the UWG simulates the conditions of a single homogeneous urban canyon, its application at district scales inevitably requires subdivision of the territory into spatial units, each with its own input parameters. As demonstrated by Hamdi et al. [31], the application of the model on regular 200×200 m grids generates thermal homogenisation between different LCZ zones, with simulated temperature differences below 0.14°C — a value insufficient to distinguish different urban configurations. Borelli et al. [35] attempt to overcome this limitation with cadastral units, but the absence of calibrated building archetypes and the neglect of anthropogenic heat constrain the accuracy of the results.

2.3 Modelling Approaches: Spatial Discretization Scale

2.3.1 The spatial scale problem

The choice of spatial discretization scale represents one of the central problems in district-scale microclimatic modelling (see Table 2.1). Every existing approach implies a trade-off between three dimensions: spatial resolution, accuracy of results, and computational cost. Rigid **grid approaches** have obvious **limitations**: Hamdi et al. [31] found that a 200×200 m grid over Toulouse produces excessive thermal homogenization, with differences between LCZ zones of only 0.14°C — a value insufficient to distinguish the different urban configurations and analyse UHI patterns. Similarly, the 500 m grids of Li et al. [36] are unsuitable for the design of Positive Energy Districts, where local variability is crucial for optimizing the energy balance. Approaches based on cadastal blocks represent a significant advancement over regular grids. Borelli et al. [35] use cadastral blocks as aggregation units for UHI mapping in Turin. The five-step workflow — morphological metrics calculation, representative case selection via Spearman correlation, UWG simulation, correlation, and mapping — obtains an $R^2 = 0.73$ for cooling degree-days (CDD) and $R^2 = 0.74$ for heating degree-days (HDD), with VtH (vertical-to-horizontal ratio), SC (surface coverage), and GR (green ratio) as the main drivers. However, the model excludes anthropogenic heat and does not consider building archetype specificity, limiting its predictive capability to purely morphological parameters. Boccalatte et al. [32] address the problem of UHI mapping at the territorial scale in the Canton of Geneva, adopting an unsupervised clustering approach (Gaussian Mixture Model) to partition the urban territory into microclimatically homogeneous zones. The method aggregates morphological data extracted from GIS sources into representative clusters used as input for separate UWG simulations, returning average annual UHII values between 1.7°C and 2.2°C depending on morphology, with partial validation against two urban weather stations. Bedra et al. [37] add an important perspective, highlighting how the use of LOD1 models — indispensable for large-scale automation — prevents the representation of fine architectural features that influence airflow near surfaces, limiting the accuracy of the urban energy balance. Their Rhino-Grasshopper automated workflow for microclimatic evaluation and morphological optimisation through the Galapagos evolutionary algorithm demonstrates the potential of parametric integration, but confirms that geometric

resolution remains a critical factor.

Table 2.1: Comparison of urban microclimate modelling approaches: trade-offs between spatial resolution, accuracy, and computational cost.

Approach	**Spatial resolution**	**Accuracy**	**Comp. cost**	**Critical limitations**
Rigid regular grid [31]	$200 \times 200\,\mathrm{m}$	Low ($\Delta T_{LCZ} \approx 0.14\,\mathrm{K}$)	Low	Thermal homogenisation; inability to capture local temperature gradients between different LCZs.
Coarse grid [36]	$500 \times 500\,\mathrm{m}$	Very low	Very low	Imprecise for local variations; inadequate for PED-scale energy balancing.
Cadastral blocks [35]	Variable (building scale)	Medium ($R^2 \approx 0.73$)	Medium	Neglects anthropogenic heat and building archetypes; morphology-only focus.
GMM clustering [32]	Adaptive (homogeneous zones)	Medium (1.7–2.2 °C UHII)	Medium	Limited validation (2 stations); intra-cluster representativeness not verified.
Hybrid CFD-UWG [34]	Heterogeneous (refined)	High	High	Complex implementation; well-mixed air assumption invalid below 15 m .

Chapter 3

Aim and scope

The review of the scientific literature highlights that, although the Urban Weather Generator (UWG) has become one of the most widely adopted tools for incorporating urban microclimate effects into Urban Building Energy Modelling (UBEM), several methodological limitations remain when the model is applied to district-scale design problems such as Positive Energy Districts (PEDs).

As the UWG is a lumped-parameter model, the accuracy of the simulations depends directly on the average values used as inputs. Consequently, the choice of spatial discretisation scale is not merely a technical detail, but constitutes a fundamental modelling variable, as it influences the average physical parameters on which the entire simulation is based. An analysis of the state of the art reveals three main critical issues:

- **Thermal homogenisation in regular grids.** Many studies use a discretisation based on regular grids (typically of the order of 200×200 m). However, this approach acts as a spatial filter that tends to smooth out the heterogeneity of the urban fabric. This homogenising effect can prevent the identification of local heat hotspots and significant microclimatic gradients. Consequently, the use of grids that are too coarse may fail to detect local microclimatic variability.

- **Incomplete representation of urban spatial units.** The shift towards spatial units that better reflect urban morphology, such as clusters based on cadastral parcels, represents an improvement on the regular grid. However, many applications do not include a systematic link to calibrated building archetypes, such as those derived from the TABULA-IEE databases or UNI

standards. Furthermore, certain relevant dynamic drivers, such as anthropogenic heat from urban traffic, are often overlooked or represented in a highly aggregated manner, limiting the model's ability to describe the complexity of urban energy flows.

- **A limited comparative evaluation of discretisation strategies.** To date, existing studies rarely isolate the impact of spatial discretisation whilst keeping the quality and resolution of the input data constant. Consequently, the quantification of modelling error directly attributable to the choice of spatial unit geometry remains limited.

The significance of these issues is further confirmed by evidence of the Urban Heat Island phenomenon in the Turin area. A comparison between the rural weather station at Turin Caselle and the urban ARPA Consolata station reveals systematic temperature gradients between urban and rural areas, which are particularly pronounced during the night (see Appendix A.1). This discrepancy highlights the need to "urbanise" the meteorological data used in energy simulations. However, whilst the Caselle–Consolata gradient allows for an estimate of the macroscopic intensity of the UHI phenomenon, adequate spatial discretisation is necessary to represent the distribution of heat within the urban fabric, thereby avoiding errors of underestimation or overestimation of the thermal loads of buildings.

In light of the critical issues identified, the aim of this thesis is to quantify the influence of the spatial discretisation strategy on the accuracy of urban microclimate simulation. Through a controlled experiment — in which the methodology for processing input data (topography, building types, vegetation and traffic) is kept constant — the study compares two domain discretisation strategies: one based on a regular grid and one based on morphological blocks. The aim is to verify whether morphological discretisation is capable of mitigating the thermal homogenisation effects typical of regular grids and providing a representation of local heterogeneity that is more consistent with the observed data.

Chapter 4

Methodology

This study employs a workflow designed to analyse and map the urban heat island (UHI) using the Urban Weather Generator (UWG) calculation engine. The methodology consists of five steps:

i. Data processing and pre-processing;

ii. Spatial partitioning and calculation of metrics;

iii. Microclimatic simulation with UWG;

iv. Model validation;

v. Analysis of results and mapping of the UHI.

The following sections provide a detailed description of each phase of the implemented pipeline. It should be noted that the first three phases (i–iii), regarding data preparation and the core simulation setup, are discussed in this chapter. Conversely, the procedures for model validation (iv) and the subsequent analysis of the results (v) are detailed in Chapter 5.

4.1 Data processing and pre-processing

The first step is to standardise, validate, and enrich geospatial data from the City of Turin's Regional Topographic Database (DBTRE), to ensure greater geometric and attributive consistency in the inputs to the simulation model. This process is divided into four phases: (A) loading and geometric standardisation; (B) processing

of building data; (C) processing of urban vegetation; and (D) final validation and output.

The main study area is Turin's Positive Energy District (PED). To include the influence of the surrounding urban context, a 200-meter spatial buffering procedure was applied to include cadastral parcels intersecting this radius. This operation was carried out for three fundamental layers: buildings, trees and grass cover.

4.1.1 Loading and geometric standardisation

To ensure the metric accuracy required for calculating the district's morphometric parameters, all data were reprojected into the EPSG:32632 (UTM Zone 32N) system. Additionally, all linear or point artefacts (e.g. boundary lines, elevation points) and topological inconsistencies that were not useful for microclimate modelling were excluded.

All source data were acquired from the Piedmont Region WFS service (CSI node), drawing from the Geotopographic Database (DBGT) of the City of Turin, with a nominal scale of 1:1000 and a certified planimetric positional accuracy of ± 0.30 m. The resolution of vegetation layers was determined via the attribute field in the DBGT.

Topological validation was performed on all extracted datasets using the QGIS validity-check algorithm (GEOS engine v. 3.13.1), confirming the complete absence of geometric errors (*Invalid Count* = 0, *Error Count* = 0) across a sample of over 8800 geographic features. A minimum tolerance threshold of 1.0 mm was applied to eliminate numerical noise. The geometric discretisation density varies by layer: the building footprint layer presents a mean segment length of 7.14 m (0.14 vert/m), sufficient for radiative thermal flux calculations; the tree layer reaches 2.93 vert/m (mean spacing 0.34 m), ensuring accurate canopy shadow projection and Sky View Factor (SVF) estimation; the grass layer presents an intermediate resolution (0.89 m mean length).

4.1.2 Processing of building data

A semantic filter was applied to the initial building dataset to exclude non-air-conditioned volumes. Only the 2,548 main buildings were isolated, excluding 1,734 auxiliary structures, such as sheds, canopies and garages, which were not suitable for urban heat balance modelling. This enabled the UWG simulation to focus solely on volumes that actively contribute to the district's anthropogenic loads

and heat exchanges. Each building has been assigned a reference construction period, mapped in accordance with the classes provided by the UWG calculation engine: pre-1980, post-1980, and new buildings. The reference year was extracted by analyzing the time ranges in the dataset; in cases of missing or unclassified data, the default value pst80 was assigned. The distribution of the building stock resulting from this mapping is summarized in Table 4.1.

Table 4.1: Classification of building stock based on construction period.

Period	**Description**	**Buildings**	**%**
pre 80	Buildings constructed before 1980	1570	61.6
post 80	Buildings constructed between 1980 and 2003	878	34.4
new	Buildings constructed from 2004 onwards	100	4.0

The next phase involves cleaning the dataset by identifying and resolving anomalies relating to building heights, as well as missing values. To identify outliers, a physical threshold of 220 metres was set. This limit was defined by taking the Intesa Sanpaolo skyscraper as a reference point; at approximately 167 meters high, it is the tallest building in Turin. Missing data was resolved through a multi-level procedure:

1. **Reconstruction from number of floors**. When the number of above-ground floors (N_{fl}) is known, the height of the building (H_{bld}) is reconstructed using the following equation:

$$H_{bld} = N_{fl} \times h_{ifl} \tag{4.1}$$

   where h_{ifl} represents the median inter-floor height, calculated statistically for the specific pair (use category, construction period) in the urban context of Turin;

2. **Local Spatial Analysis**. Where the number of floors is also missing, the height is estimated by analyzing the "geographical neighbors". Through a spatial search within a predetermined radius, buildings with similar characteristics (same use category and period) are identified and their median height is extracted;

3. **Statistical Estimate by Category**. In the absence of suitable geographical neighbors, the median calculated on the entire dataset is applied with respect

to the building's category of use alone, ensuring consistency with its functional purpose;

4. **Global Imputation**. If it is not possible to determine the value using any of the above criteria, the global median of the entire dataset is assigned.

The number of floors above ground is a critical parameter as it influences the correct assignment of reference prototypes to each building. To ensure consistency in the dataset, the inter-floor height is initially verified. If it is inconsistent or missing, it is recalculated as follows:

$$N_{fl,corrected} = \frac{H_{bld}}{h_{target}} \tag{4.2}$$

where h_{target} is the median reference value derived hierarchically from the validated dataset (by category-era pair or by category alone). Finally, a minimum value of $N_{fl} = 1$ is guaranteed for each air-conditioned volume.

The transition from geometric data to simulation parameters is achieved by assigning energy archetypes to DOE Reference Buildings. As shown in Table 4.2, the mapping is not limited to a simple association by categorical variable, but also takes into account dimensional criteria such as total floor area and number of floors. This approach enables dynamic differentiation between subcategories of the same prototype. The size thresholds were not predetermined, but derived from calculating midpoints between the floor areas of the DOE reference models. This approach minimises approximation error by allocating each building in the district to the energy prototype that is closest in terms of area and volume.

Table 4.2: Mapping of DOE archetypes: dimensional thresholds and standard parameters.

DBTRE Category	Prototype	Logical Condition / Standard Definition
Office	Small Office	Area $< 2746\ m^2$ **AND** Floors ≤ 2
	Large Office	Area $> 25178\ m^2$ **OR** Floors > 6
	Medium Office	Outstanding cases (4982 m^2, 3 Floors)
Hotel	Small Hotel	Area $\leq 7680\ m^2$ **AND** Floors ≤ 4
	Large Hotel	Area $> 7680\ m^2$ **OR** Floors > 4
School	Primary School	Area $\leq 13242\ m^2$ (excl. University)
	Secondary School	Area $> 13242\ m^2$ **OR** University
Residential	Midrise Apt.	Area $3134\ m^2$ **AND** 4 Floors
Retail	Stand-alone	Area $2319\ m^2$ **AND** 1 Floor
	Supermarket	Area $4180\ m^2$ **AND** 1 Floor
Restaurant	Full Service	Area $511\ m^2$ **AND** 1 Floor
Health	Hospital	Area $22421\ m^2$ **AND** 5 Floors
	Outpatient	Area $3804\ m^2$ **AND** 3 Floors
Industrial	Warehouse	Area $4835\ m^2$ **AND** 1 Floor

For the remaining categories without a direct equivalent in the DOE standard, associations were made based on thermal load and/or occupancy profile similarity, as shown in Table 4.3.

Table 4.3: Mapping by non-standard categories via thermophysical analogies.

DBTRE Category	Prototype	Thermophysical Analogy
Museum	Medium Office	Regular hours and controlled internal loads.
Cinema, Theaters, Auditorium	Full Service Rest.	High crowd density and high ventilation.
Cultural activity venue	Full Service Rest.	Intermittent occupancy profile and variable loads.
Indoor swimming pool	Hospital	High energy intensity and critical humidity management.
Gyms, Sports	Secondary School	Latent loads (physical activity) and similar ventilation profiles.
Place of worship	Stand-alone retail	Large air volumes with zone heating.
Passenger station	Stand-alone retail	Large open spaces and intermittent people flows.
Social Services	Outpatient Health	Typical loads for service-intensive offices.
Multi-story Parking	Warehouse	Minimal thermal loads and no intensive air conditioning.
Unknown	Midrise Apt.	Precautionary assumption based on the prevailing category.

Albedo coefficients (see Table 4.4) were also used to reflect the characteristics of the materials under examination as accurately as possible. Values differentiated based on construction period and function allow for more accurate modelling of radiation balance and heat exchange within the urban canyon.

Table 4.4: Surface albedo coefficients differentiated by construction period and use.

Category / Period	α_{roof}	α_{wall}	Motivation
Industrial / Warehouse	0.60	0.45	Metal sheets, treated surfaces, and light-colored concrete panels [38] [39]
Pre-1980	0.30	0.35	Flat roofs paved or covered with gravel; standard plaster and concrete [38] [39]
Post-1980	0.18	0.45	Dark bituminous membranes (sheathing); modern facades in light-colored concrete [38] [39]
Default	0.25	0.45	Average values [39]

Following the reconstruction and cleaning of the dataset to increase its robustness, all elements with an area of less than $15m^2$ were removed as they typically represent acquisition errors or digitisation artefacts. This process removed 128 polygons, reducing the dataset from 2,548 to 2,420 buildings. The final step in processing the buildings involves combining those with similar thermal and construction characteristics that are adjacent to each other. The NetworkX library was used to identify buildings that met the criteria for spatial and thermal homogeneity:

- **Spatial adjacency**. Two buildings are considered adjacent if their buffers (0.1 m) intersect.
- **Thermal and construction homogeneity**. Buildings must have the same DOE prototype and construction period, and a height difference of less than 8 m (equivalent to 2–3 floors).

For each identified cluster, a weighted dissolve is performed to aggregate:

- **Total area**: sum of the areas of the individual buildings;
- **Volumes**: a weighted sum is used to calculate the average height and average number of floors;
- **Energy attributes**: retained from the first building in the cluster;
- **Albedo**: the arithmetic mean of the component values.

- **Height**: calculated as

$$H_{bld} = \frac{\sum_i A_i \times H_{bld,i}}{\sum_i A_i} \tag{4.3}$$

4.1.3 Processing of urban vegetation

The tree vegetation data is provided as point entities, each with a canopy diameter attribute. A geometric reconstruction of the canopy was then performed using radial buffering to transform each point into a circular polygon.

$$Crown = Point \oplus buffer \frac{D}{2} \tag{4.4}$$

where D is the diameter of the crown in metres. The extracted diameters showed anomalies due to errors in data entry (e.g. values exceeding 100 m). To prevent distortions in the calculation of the urban green fraction, two corrective actions were implemented:

- Outlier clipping: A physical threshold of $20m$ was set, and all diameters exceeding this value were clipped to this maximum.
- Data imputation: Missing values were replaced with a default diameter of $4m$, derived from the median dimensions of Turin's local tree heritage.

The grass-covered areas were extracted from the DBTRE in the form of two-dimensional polygons. A topological validation was then performed to resolve any inconsistencies, such as overlaps or self-intersections, before they were integrated into the model, ensuring the geometric integrity of the natural surfaces. To ensure there is no overlap between buildings, vegetation and grassland, a geospatial overlay procedure involving ordered subtraction has been implemented. First, the tree crowns are subtracted from the buildings, removing any crowns that overlap with the buildings. Next, a second subtraction is performed between grassland and the remaining geometry, excluding grassland from areas occupied by buildings or tree canopies. This hierarchy reflects physical priority: buildings occupy the ground exclusively, followed by tree crowns, and finally grassland occupies the remaining areas.

4.1.4 Final validation and output

To evaluate the effectiveness of the preprocessing workflow and ensure the physical consistency of the simplified dataset, a final validation was performed. Table 4.5

summarizes the transition from the raw DBTRE data to the optimized simulation units. The procedure consolidated 2,420 buildings into just 1,019, reducing the number of geometric units by 76.20%. Despite this significant aggregation, thermal mass conservation was 98.08%, confirming that the operation primarily involved small buildings or those with marginal characteristics, thereby preserving the volumetric integrity of the dataset. This approach improves the numerical stability of the UWG model by reducing geometric fragmentation without compromising thermal accuracy.

Table 4.5: Summary of building metrics following the geometric dissolve procedure.

Metric	**Initial**	**Final**	**Variation**
Number of buildings	4282	1019	76.20%
Total Area [m^2]	769055.61	670693.54	12.79%
Total Volume [m^3]	12380318.20	12143161.77	1.92%

Analysis of the composition of buildings (see Figure 4.1) in the area under study reveals a strong residential predominance, with over 700 buildings classified. Specifically, the midrise apartment prototype is the most common type, with 723 units identified, representing 71.0% of the total stock. The remaining categories show significantly lower frequencies: the second and third largest groups are small offices and retail outlets, with 79 and 59 buildings, respectively. These are followed by public services and educational facilities, which despite their larger individual volumes, show a low frequency. Examples include primary schools (28 units) and secondary schools (27 units). Specialised healthcare facilities, including clinics and hospitals, are the least common, accounting for less than 1% of the total.
The morphological characterization is further detailed by height analysis. The analysis of the altimetric profile (see Figure 4.2) reveals a medium compact urban fabric, with a bimodal distribution of building heights. Most building units range from 0 m to 40 m. Frequency peaks are concentrated around 10 m and 20 m, values corresponding to three- and six-story above-ground building types, respectively.

While most buildings fall within the low-to-medium height range, the neighborhood includes vertical singularities that reach a maximum height of 155.74 m. These variations are spatially mapped in Figure 4.4, providing a clear overview of the urban grain and the location of multi-story structures.
Figure 4.5 shows the geographical location and spatial extent of the case study area.

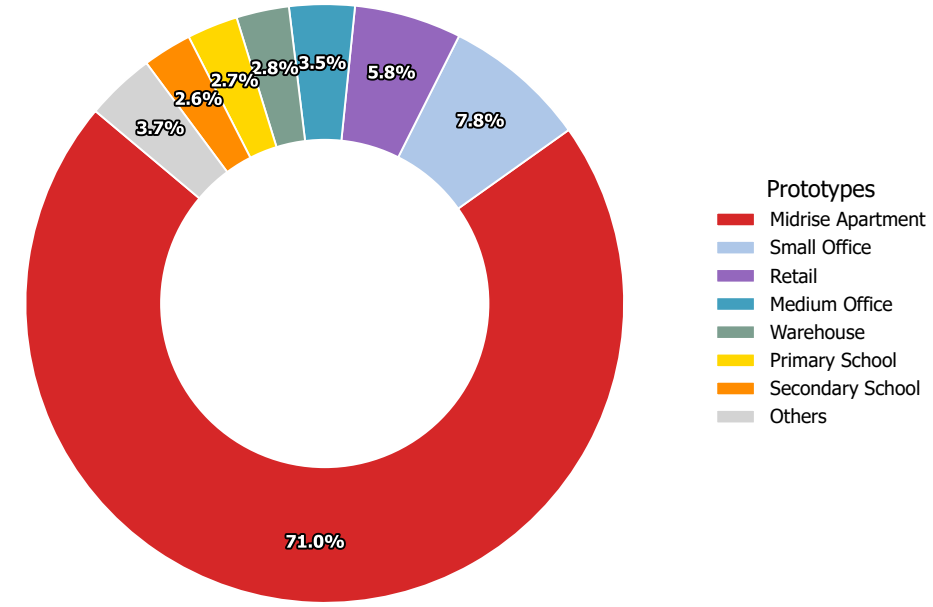


Figure 4.1: Distribution of building prototype across the study area.

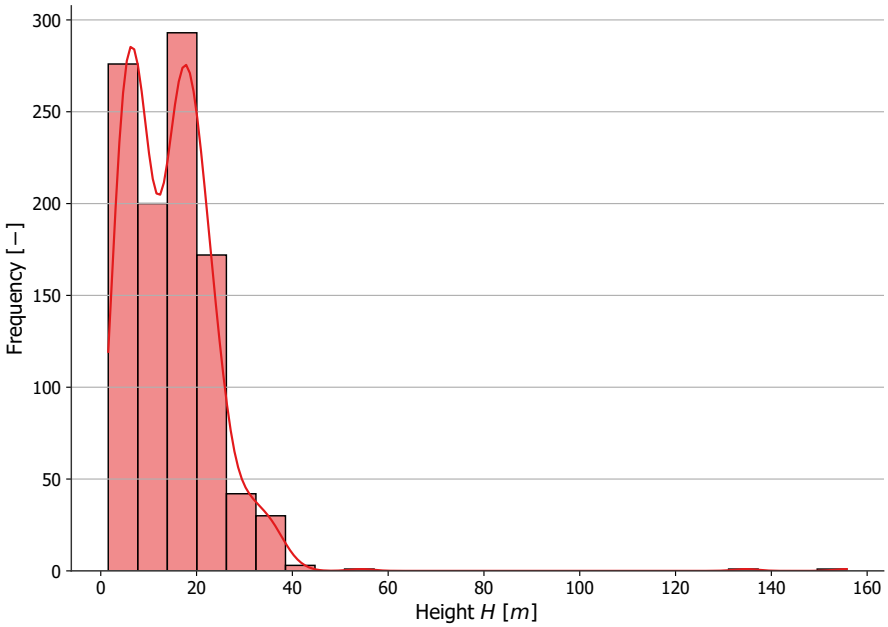


Figure 4.2: Frequency distribution of building heights.

Figure 4.3 illustrates the spatial distribution of archetypes, highlighting the functional layout of the district and showing a dense residential core.

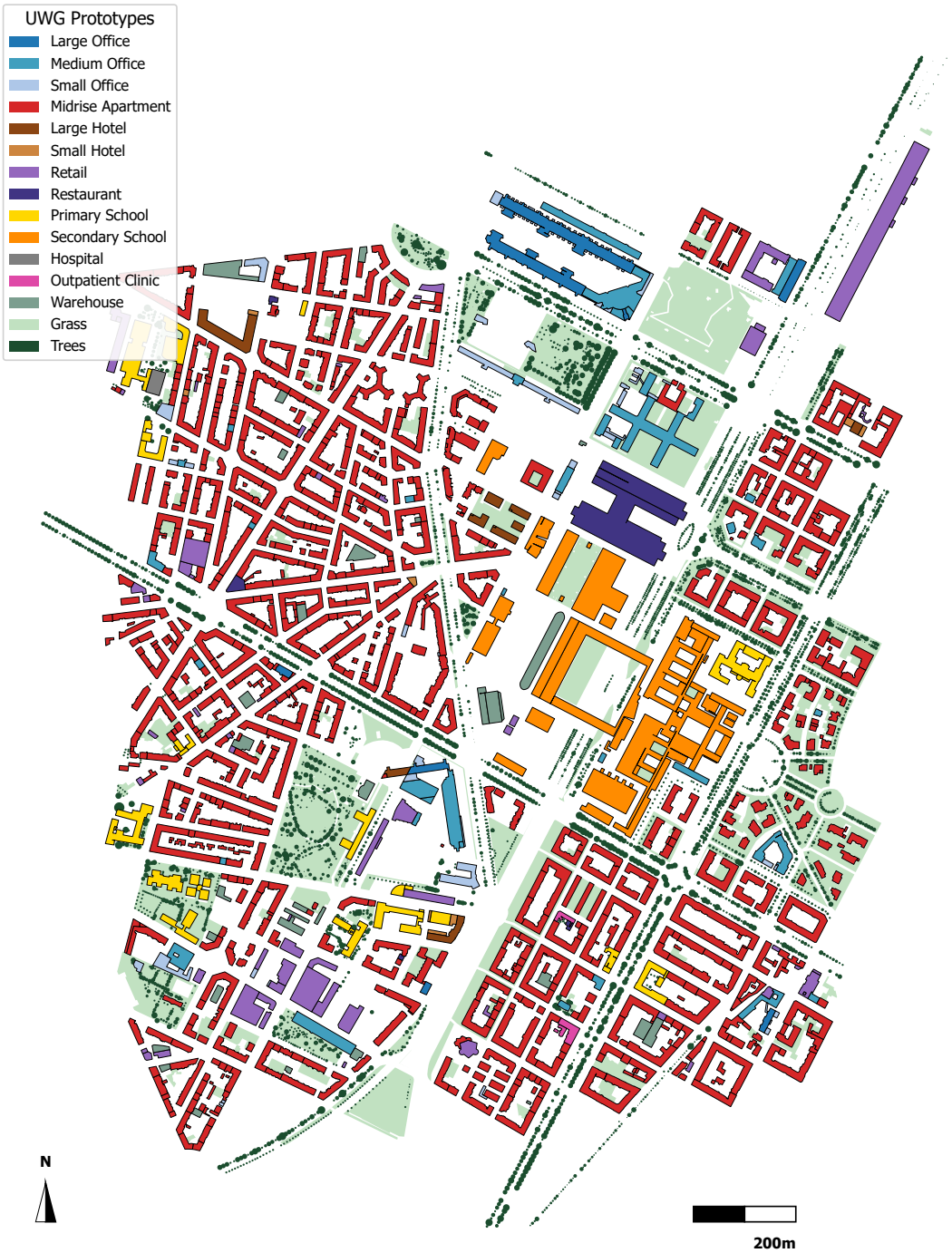


Figure 4.3: Spatial mapping of building prototypes.

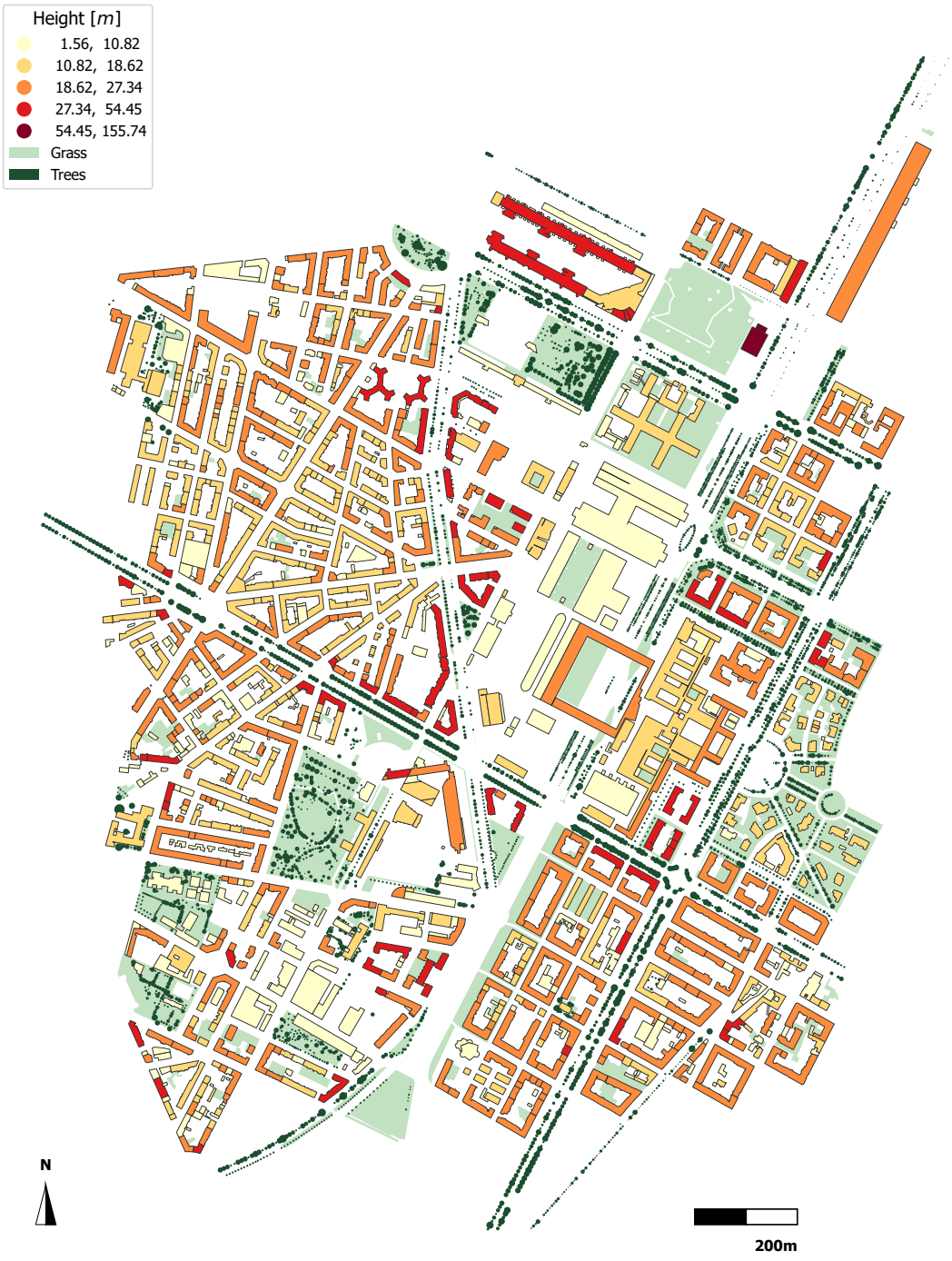


Figure 4.4: Spatial mapping of building height.



Figure 4.5: Morphological map of the Turin PED area.

4.2 Spatial partitioning and calculation of metrics

The second step of the workflow involves defining the spatial units and calculating the morphological characteristics of each unit. This phase is critical, as it determines the scale at which the input data will be aggregated for the next simulation phase using the UWG.

4.2.1 Spatial Partitioning Strategies

The partitioning process consists of subdividing the study area into discrete geometric units, which serve as the spatial basis for calculating morphometric and thermal parameters. In this study, two alternative strategies were implemented:

- **Regular Grid**: A computationally efficient approach where the domain is subdivided into square cells of fixed size, regardless of the underlying urban morphology.
- **Morphological Blocks**: A more sophisticated approach where the spatial units coincide with actual urban blocks, defined by road boundaries and built structures. This method ensures that the boundaries of the units respect the physical layout of the city, maximizing the homogeneity of the urban canyon characteristics within each partition.

Furthermore, to validate the methodology (see Chapter 5), the influence of grid size and positioning was analyzed as part of a *sensitivity analysis*. This allowed for an evaluation of how spatial resolution affects the calculation of urban metrics and the subsequent microclimatic simulation results.

Grid

The regular grid-based strategy involves dividing the spatial domain into square cells (see Figure 4.6), each with a resolution of **200 x 200 metres**. The generation process is structured into five main phases to ensure topological consistency of the data:

1. **Domain definition**. The outer perimeter of the grid is defined starting from the total bounds of the entire dataset.

2. **Mesh construction**. Starting from the minimum coordinates of the total bounds, an orthogonal mesh of square cells is generated. The geometry of the grid is projected into the EPSG:32632 reference system, ensuring perfect overlap with the cartographic layers of the DBTRE database.

3. **Preventive screening**. In order to optimise computational efficiency, a spatial join is performed between the grid and the building and vegetation layers. Only cells containing at least one physical element are retained, discarding those that are irrelevant for microclimate modelling.

4. **Assignment of buildings**. In order to prevent duplication errors in the calculation of volumes, each building is uniquely assigned to a single cell. The criterion adopted is that of maximum area intersection: a building that intersects the boundaries of several units is assigned to the cell that contains the largest fraction (usually $> 50\%$) of its surface area.

5. The process ends with the **removal of unbuilt cells** following unique assignment and sequential renumbering of cell identifiers (IDs).

Morphological blocks

The creation of morphological blocks is the most advanced approach, whereby spatial units coincide with real urban blocks (see Figure 4.7). The aim of this strategy is to preserve continuity with the existing urban fabric while maximising thermal and morphological homogeneity within each calculation unit. The procedure consists of the following stages:

1. **Exploration of the road network**. An in-depth analysis of the road network available on OpenStreetMap (OSM) was conducted using the **OSMnx** library. To ensure macro-consistency of the blocks, the extraction filter was limited to main roads, as these represent the primary backbone of the urban grid and act as natural dividing lines.

2. **Generation of cutting blades**. The linear geometry of the roads has been integrated with the outer perimeter of the urban area buffer, consisting of buildings, vegetation, and a 25-metre safety margin. These elements combine to form a set of 'cutting blades' that create the geometric cut-out mask.



Figure 4.6: Grid discretization based on a 200x200 m resolution.

3. **Tessellation and polygonisation**. By applying the cutting lines to the continuous surface of the study area, the domain is divided into polygons. Each

polygon represents a distinct morphological unit, defined by the surrounding road infrastructure.

4. **Topological screening and cleaning**.To eliminate micro-polygon residues (e.g. those present in traffic islands) and ensure domain continuity, empty areas were incorporated into adjacent blocks. This process involves taking equidistant samples (at a step size of 2.0 m) along shared boundaries and creating a constrained Voronoi diagram. Each Voronoi cell was assigned to the nearest full block and then merged using the 'dissolve' function.

5. **Attribute association**.Each morphological block inherits the physical and energy properties of the buildings within it. Thanks to the alignment of road and property boundaries, this approach virtually eliminates ambiguity in allocating buildings that straddle different calculation units.

The spatial discretization procedure resulted in 76 cells of 200×200 m in the regular grid configuration and 146 morphological blocks in the morphology-based approach. For clarity and reference, the maps showing the numbered spatial units are reported in Appendix A.2. The higher number of spatial units in the morphological approach reflects the finer representation of the urban fabric obtained by following the road network and block structure of the city.



Figure 4.7: Morphological blocks discretization based on the urban fabric.

4.2.2 Calculating metrics for Spatial Units

A set of morphological, geometric and energy parameters is calculated for each spatial unit (grid cell or morphological block). These parameters are then fed into the urban parameterisation models and the UWG engine. For this case study, only the metrics that will be overwritten in the UWG model or used in post-simulation analyses are calculated. The following can be obtained from the spatial data:

- **Surface Coverage** (SC). It is the ratio of total built-up area, A_i, to the area of the reference spatial unit, A_{block}.

$$SC = \frac{\sum A_i}{A_{block}} \tag{4.5}$$

- **Green Ratio**. It represents the total vegetative fraction of the spatial unit, calculated as the sum of the Grass Cover (GC) and the Tree Cover (TC). These parameters quantify the presence of horizontal and elevated greenery, respectively:

  - **Grass Cover (GC)**: the ratio of the total area covered by grass(A_{grass}) to the area of the reference spatial unit (A_{block}).
  - **Tree Cover (TC)**: the ratio of the horizontal projection of tree crown (A_{tree}) to the area of the reference spatial unit(A_{block}).

  The resulting equation for the Green Ratio is defined as follows:

$$GR = GC + TC = \frac{A_{tree} + A_{grass}}{A_{block}} \tag{4.6}$$

- **Average Building Height** (ABH). Arithmetic mean of building heights, H_i, within the spatial unit:

$$ABH = \frac{\sum_i^n H_i}{n} \tag{4.7}$$

- **Vertical to Horizontal** (VtH). It is calculated as the ratio between the sum of the areas of the facades, A_{vert}, of all buildings and the total area of the spatial unit.

$$VtH = \frac{\sum A_{vert}}{A_{block}} = \frac{\sum_{i=1}^n (P_i \cdot H_i)}{A_{block}} \tag{4.8}$$

  where P_i is the perimeter of the building.

- **Characteristic Length** (CL). Representative linear dimension of the spatial unit, computed as the average of the bounding box dimensions to better represent the linear urban scale compared to the square root of the area:

$$CL = \frac{\Delta x + \Delta y}{2} \tag{4.9}$$

where Δx and Δy are the bounding box dimensions. Used in UWG for turbulent length scale calculations.

Extended Morphological and Energy Parameters

Beyond the primary morphological inputs required by the Urban Weather Generator, a secondary set of environmental and geometric indicators has been calculated. These parameters are essential for the subsequent sensitivity analysis and the post-simulation validation phase, as they allow for a more granular characterization of the thermal stress of each spatial unit in relation to its physical-technical properties.

- **Road Cover (RC):** Represents the fraction of ground occupied by road surfaces or impermeable pavements within the spatial unit. In this study, it is derived by complementarity relative to the built-up and vegetated areas:

$$RC = 1.0 - (SC + GR) \tag{4.10}$$

where SC is the Surface Coverage (Eq. 4.5) and GR is the Green Ratio (Eq. 4.6).

- **Average Albedo (α_{avg}):** This represents the weighted average solar reflectance of the spatial unit's surfaces. The calculation integrates differentiated contributions based on construction era and building typology (α_{bld}), road surfaces ($\alpha_{road} = 0.12$), and green areas ($\alpha_{veg} = 0.20$):

$$\alpha_{avg} = (SC \cdot \alpha_{bld}) + (RC \cdot \alpha_{road}) + (GR \cdot \alpha_{veg}) \tag{4.11}$$

- **Height-to-Width Ratio (H/W):** Defines the urban canyon geometry. It is calculated as an effective proxy for density and average building height, normalizing the height relative to the non-built space:

$$H/W = ABH \cdot \left(\frac{SC}{1.0 - SC}\right) \tag{4.12}$$

where ABH is the Average Building Height (Eq. 4.7).

- **Compactness (C):** A dimensionless parameter describing the geometric efficiency of the block, calculated as the ratio between the built volume and the projected frontal area of the buildings (based on the maximum side L_{max} of each building):

$$C = \frac{1}{n} \sum_{i=1}^{n} \left(\frac{6 \cdot V_i^{2/3}}{A_{frontal,i}} \right) \tag{4.13}$$

- **Total Combined Anthropogenic Heat (Q_{tot}):** Represents the total anthropogenic heat density released into the urban atmosphere [W/m^2]. It combines the sensible heat from road traffic (Q_{tr}), derived from local raster data, and the heat released by buildings (Q_{bld}), estimated based on national benchmarks (UNI 10339 and UNI/TS 11300) for building prototype and era:

$$Q_{tot} = Q_{tr} + Q_{bld} = Q_{tr} + \frac{\sum(A_i \cdot N_{floor,i} \cdot q_{u,i})}{A_{block}} \tag{4.14}$$

where A_i is the building area, $N_{floor,i}$ is the number of floors, and $q_{u,i}$ is the specific thermal load per use-case.

Internal thermal loads

Internal heat gain parameters, comprising occupancy density (n_{occ}), equipment power density (q_{elec}), and lighting power density (q_{light}), were defined for each building prototype according to the technical standards and regulations effective in the Italian territory. Specifically, the values were derived from UNI 10339 [40], UNI/TS 11300-1 [41], and UNI EN 15193-1 [42].These parameters represent essential inputs for the urban parameterization of the UWG engine, as they determine the internal sensible heat gains that dictate the building energy balance. As detailed in Table 4.6, lighting loads are differentiated by construction era to account for the technological transition and the consequent reduction in internal gains.

Table 4.6: Internal load parameters calibrated by building prototype and construction era.

Prototype	n_{occ}	q_{elec}	q_{light} $[W/m^2]$			Q_{tot} $[W/m^2]$		
	$[ppl/m^2]$	$[W/m^2]$	*Pre-80*	*Post-80*	*New*	*Pre-80*	*Post-80*	*New*
Midrise Apartment	0.04	3.0	10.0	6.0	2.5	16.0	12.0	8.5
Office	0.07	7.0	18.0	12.0	5.0	30.3	24.3	17.3
Stand-alone Retail	0.30	5.0	25.0	15.0	8.0	52.5	42.5	35.5
School	0.50	4.0	15.0	10.0	4.5	56.5	51.5	46.0
Hotel	0.10	4.0	12.0	8.0	4.0	23.5	19.5	15.5
Supermarket	0.25	12.0	20.0	12.0	7.0	50.8	42.8	37.8
Warehouse	0.01	1.0	6.0	4.0	1.5	7.8	5.8	3.3

Anthropogenic heat from traffic

To calibrate energy loads in the UWG model, a spatial layer relating to the anthropogenic heat produced by vehicular traffic was integrated. Due to the difficulty of obtaining direct in situ measurements, the methodology based on environmental proxies adopted for the Geneva case study [32] was used. The approach is based on the assumption of a linear relationship between air pollution and heat released, using the concentration of NO_2 as a direct proxy. For the Turin case study, the data is sourced from the 2022 monitoring campaign conducted by the "Respira Torino" committee [43]. Following analysis of the data set, it was established that the maximum concentration value in the study area is $55\mu g/m^3$. With reference to the technical literature on the subject of dense and busy urban areas, the upper limit of the heat flux was set at $20W/m^2$. The equation for heat transfer is given by:

$$Q_{\text{sens}} = \begin{cases} \frac{NO_2}{55.0} * 20.0 & \text{if } NO_2 \leq 55.0\,\mu\text{g/m}^3 \\ 20.0 & \text{if } NO_2 > 55.0\,\mu\text{g/m}^3 \end{cases} \tag{4.15}$$

NO_2 levels should remain below $55.0\mu g/m^3$, with a corresponding heat flux not exceeding $20W/m^2$. Starting from the point values collected in the field, a continuous map was generated using ordinary kriging, with a resolution of $10m/px$ to maintain consistency with the size of the city's buildings and streets. The concentration map was converted into a heat flow map using raster algebra tools. This map was then aggregated into spatial units (blocks and grid). For each polygon, the final value indicates the spatial average of the pixels contained. This is calculated

as follows:

$$Q_{sens,i} = \frac{1}{n} \sum_{j=1}^{n} P_j \tag{4.16}$$

The following images show the average value of traffic anthropogenic heat flux for each spatial unit, analysed by grid (see Figure 4.8) and by morphological block (see Figure 4.9).

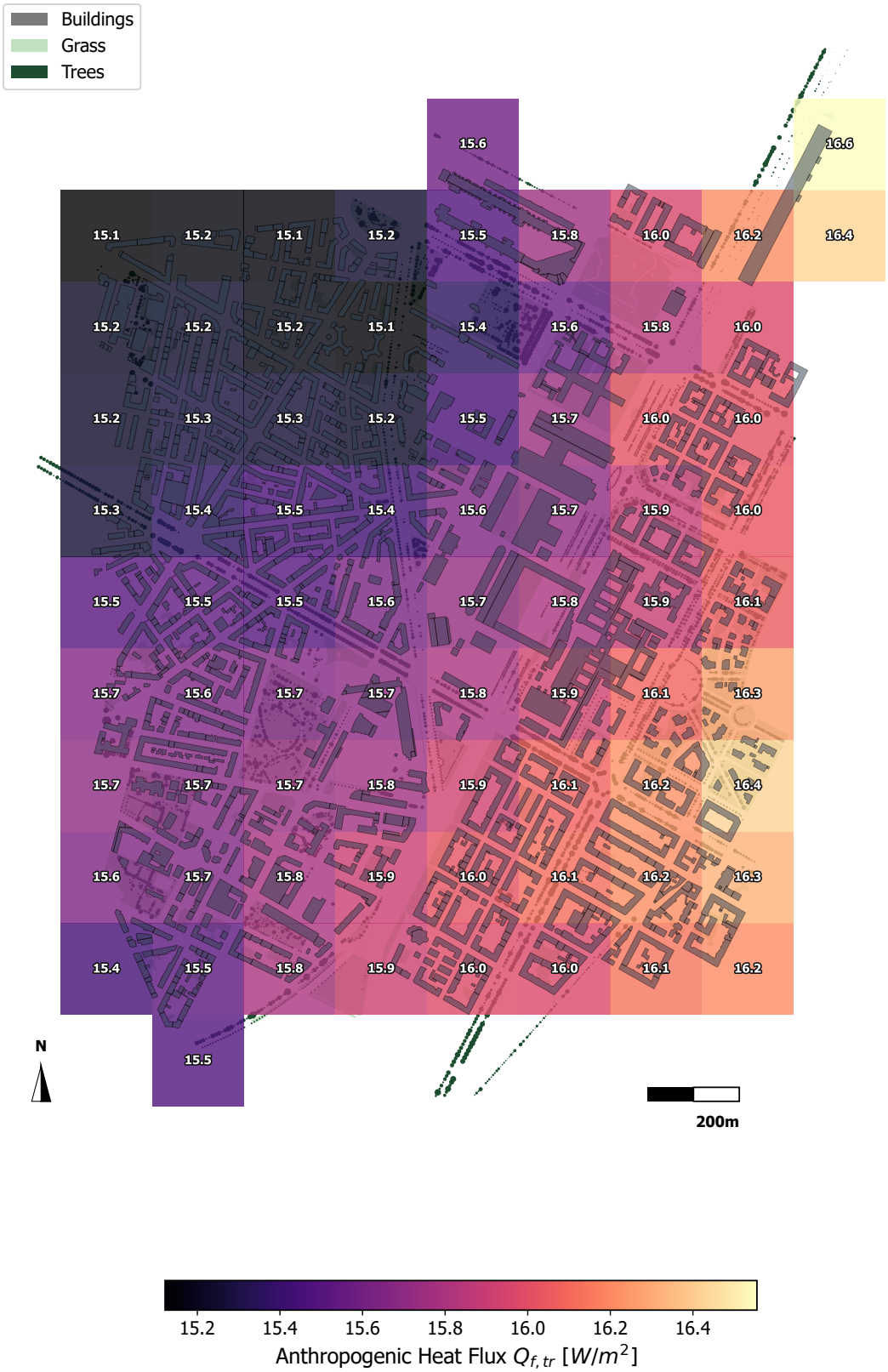


Figure 4.8: Traffic Anthropogenic Heat Flux - Grid configuration.

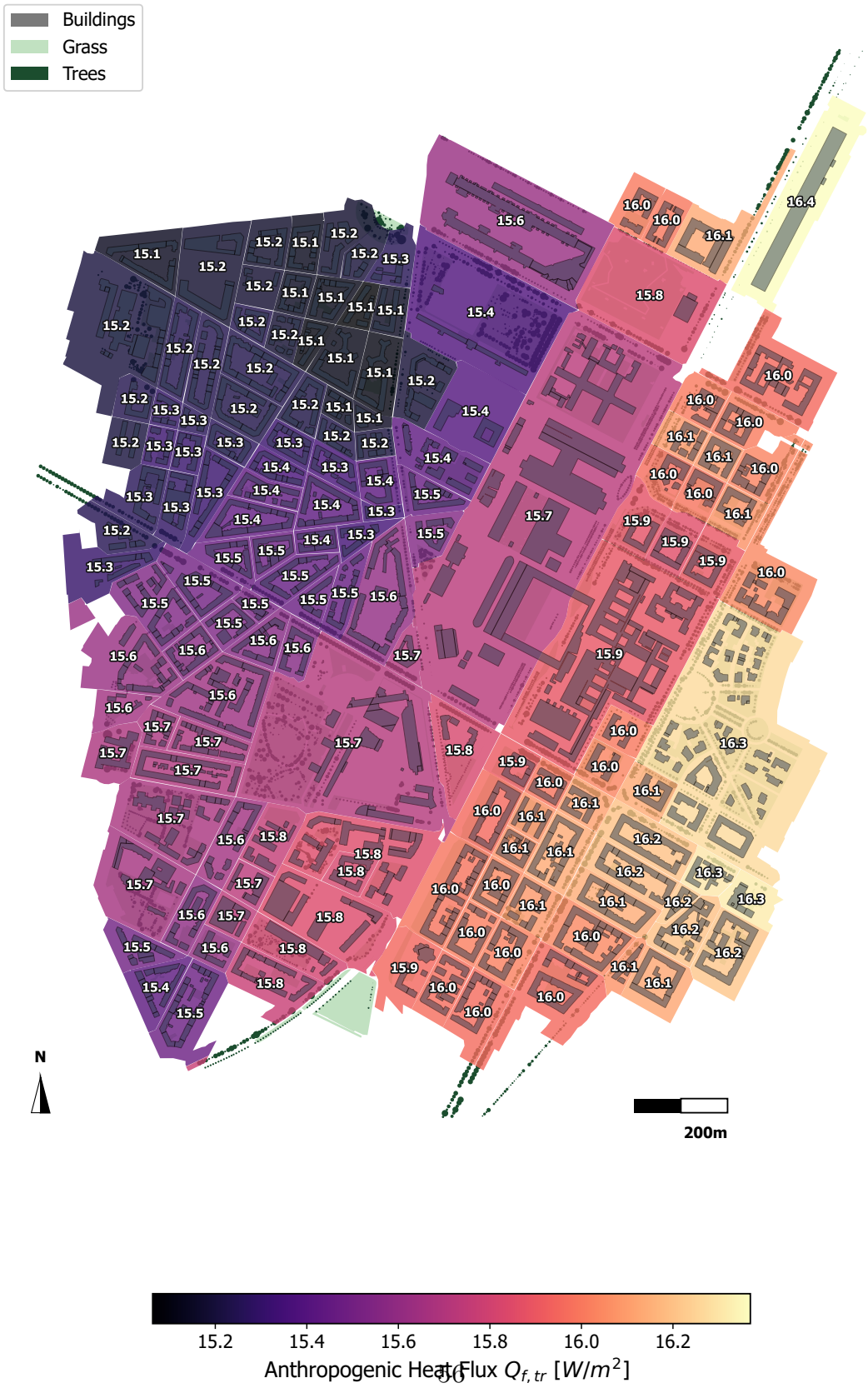


Figure 4.9: Traffic Anthropogenic Heat Flux - Morphological Blocks configuration.

4.3 Microclimatic simulation with UWG

Urban microclimate modeling is carried out using the open-source code Urban Weather Generator version 4.2. The model, developed by the MIT Building Technology Lab, enables the generation of urban weather files (EPW format) starting from reference rural conditions and morphological parameters of the built environment.

4.3.1 Generation of Rural Meteorological Dataset

The workflow begins with the generation of the rural EPW file, representing undisturbed boundary conditions for UWG simulations. A key methodological choice concerns the use of an **Actual Meteorological Year (AMY)** rather than a Typical Meteorological Year (TMY). While TMY files are statistically synthesized from multi-year datasets to represent "average" conditions, they may not capture the actual thermal dynamics of the reference year under study. The AMY approach ensures consistency between simulated urban microclimates and real-world meteorological forcing, enabling direct comparison with observed data when available.

Hourly meteorological data for 2024 were obtained from ARPA Piemonte [44] monitoring station (Caselle, 45.192°N, 7.652°E, 285 m a.s.l.) in CSV format. The dataset includes: air temperature, relative humidity, atmospheric pressure, global horizontal irradiance (GHI), and wind speed/direction. These raw observations were integrated into EPW format using a TMY3 template from Torino-Caselle airport as structural scaffold, preserving standard header metadata while overwriting all 8760 hourly data rows with 2024 measured values. Key processing steps included:

- **Leap year correction**. Year 2024 contains 366 days, so February 29th was removed to comply with EPW standard format (8760 hours);
- **Quality control** that includes physical validation of temperature, humidity, irradiance ranges and gap filling via linear interpolation for short missing data sequences (<6 hours);
- **Psychrometric calculations**. Dew point temperature, required by EPW but not measured by ARPA, calculated from dry bulb temperature and relative humidity using Magnus-Tetens approximation [45];

- **Solar radiation decomposition**. Direct normal irradiance (DNI) and diffuse horizontal irradiance (DHI) were estimated from the measured GHI using the empirical correlation of Erbs et al. [46] as implemented in the Python pvlib library [47]. The solar position was calculated using the solar position algorithm [48].

Physical coherence constraints were applied by setting the night-time irradiance and low-altitude direct normal irradiance (DNI) values to zero. Prior to UWG implementation, the resulting EPW file was verified for format conformance and physical plausibility.

4.3.2 Multi-Prototype Configuration for Mixed-Use Districts

A significant methodological challenge in urban microclimate modelling concerns the representation of functionally heterogeneous urban structures. Conventional applications of the UWG model customarily allocate a single building prototype to each spatial unit, a simplification that falls short of capturing the intricacies inherent in functional mix. In order to accurately model this heterogeneity, a multi-prototype configuration has been implemented. In this configuration, the built volume of each spatial unit (grid cell or morphological block) is disaggregated into a weighted combination of different functional types and construction periods. Therefore, each unit is defined by a set of descriptive tuples:

$$\mathrm{BLD}_i = (\mathrm{prototype}_i, \mathrm{era}_i, w_i) \tag{4.17}$$

where

- $\mathbf{prototype}_i$ is indicative of the functional destination, which has been mapped onto the DOE archetypes;

- $\mathbf{era}_i$ is employed to denote the designated construction period, categorised as pre-80, post-80, or new, respectively;

- $\mathbf{w}_i$ represents the specific fraction of that combination within the cell, subject to the normalization constraint $\sum w = 1$.

4.3.3 Configuration and calibration of simulation parameters

In order to run the model, a set of parameters must be defined to govern the thermodynamic processes within the urban canyon and the urban boundary layer (UBL). For the Turin case study, these parameters were set to reflect the properties of local materials and to ensure numerical stability in the calculations (see Table 4.7).

Table 4.7: General simulation parameters and global physical constants set in the UWG model.

Category	Parameter	Value
Simulation	Time step (Δt) [s]	300
	Duration [hours]	8760
Road Properties	Thermal conductivity (k_{road}) [W/mK]	1.2
	Volumetric heat capacity (c_{road}) [J/m^3K]	1.6×10^6
	Surface albedo (α_{road}) [-]	0.15
Boundary Layer	Daytime UBL height ($h_{\text{ubl},1}$) [m]	1000
	Nighttime UBL height ($h_{\text{ubl},2}$) [m]	80
Vegetation	Phenological period [months]	April – October
	Albedo / Leaf emissivity [-]	0.25 / 0.95

For each spatial unit, the following parameters were dynamically assigned based on local characteristics: surface coverage, average building height, vertical-to-horizontal ratio, characteristic length, green ratio, spatially-differentiated surface albedos for roofs and walls, anthropogenic heat from traffic, and the specific building prototype and construction era mix.

Unlike the software defaults based on US standards (ASHRAE), the properties of the buildings have been recalibrated to reflect the Italian building stock and national technical regulations. This operation was performed using a post-generation patch procedure, acting individually on each BEM (Building Energy Model) object instantiated in the tuples.

Building envelope properties and internal loads

The thermal performance of opaque walls and the air permeability of fixtures have been recalibrated according to the TABULA-IEE database [49] (see Table 4.8).

Thermal transmittance (U_{wall}) was obtained by modifying the thickness and conductivity of the wall layers for each period, maintaining a volumetric heat capacity consistent with Italian solid construction types.

Table 4.8: Building envelope thermophysical properties and infiltration rates stratified by construction era.

Era	U_{wall} [W/(m^2·K)]	**Infiltration** [vol/h]	**SHGC** [-]
pre-80	1.14	1.2	0.60
post-80	0.78	0.8	0.50
new	0.34	0.4	0.35

In addition to the envelope thermophysical properties, the internal heat gains (occupancy, electrical equipment, and lighting) were assigned to each building prototype using the values calibrated and discussed in the section above (specifically in Table 4.6). This integrated calibration approach ensures that both the conductive heat transfer through the building fabric and the internal sensible heat generation are representative of the Italian building stock and its operational standards.

Traffic modulation and anthropogenic heat

The sensible anthropogenic heat resulting from vehicular traffic ($Q_{traffic}$), calculated spatially as described in section , was integrated into the UWG model using a normalized time profile. The hourly variation follows a weekly matrix that distinguishes between weekdays, Saturdays, and Sundays.

4.3.4 Synthesis of the Simulation Setup

To ensure the reproducibility of the study and clarify the data flow within the simulation engine, Table 4.9 provides a comprehensive synthesis of all input parameters, their sources, and their functional role within the UWG architecture. Each parameter is classified according to its origin:

- **measured** inputs derive directly from the ARPA Piemonte AMY dataset and are ingested without modification into the Rural Station Model;
- **computed** inputs are derived through the GIS processing workflow described in Section 4.3, translating cadastral and morphological data from the DBTRE into dimensionless urban descriptors;

- **calibrated** inputs correspond to parameters for which the software defaults — based on US standards and DOE archetypes — were systematically overwritten through a post-generation patch procedure to reflect the Italian building stock, national technical regulations, and local material properties; finally,
- **default** inputs retain the original UWG parameterisation, as no site-specific data warranted their modification.

The model produces as primary output an urbanised EPW file in which the hourly rural air temperature is replaced by the simulated urban canyon temperature $\mathrm{T_{urb}}$, from which the Urban Heat Island intensity is derived at each spatial unit as $\Delta T = T_{\mathrm{urb}} - T_{\mathrm{rural}}$.

Table 4.9: Synthesis of UWG simulation parameters: inputs, sources, and outputs.

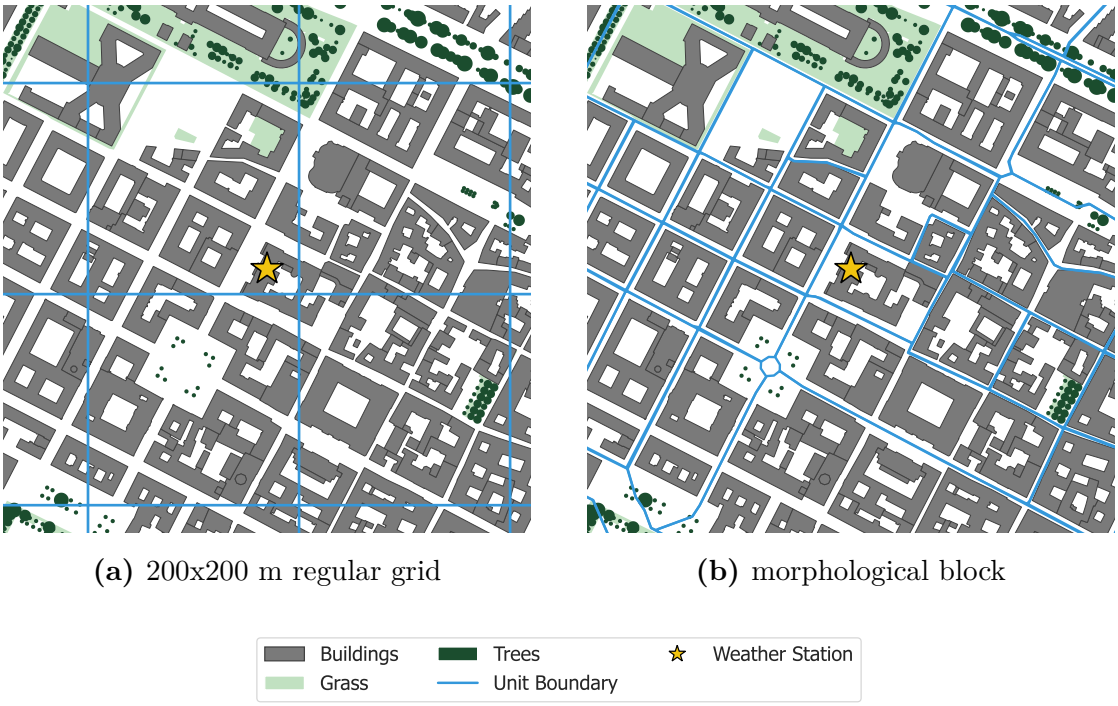
Parameter	Type	Source / Method
Rural Station Model & Vertical Diffusion (RSM – VDM)		
Air temperature, relative humidity, pressure, wind speed	Measured	ARPA Piemonte – Caselle station (AMY 2024)
Direct and diffuse solar radiation (DNI, DHI)	Computed	Erbs et al. correlation via *pvlib*
Dew point temperature	Computed	Magnus-Tetens approximation
Rural soil and vertical diffusion profiles	Default	UWG internal parameterisation
Urban Boundary Layer (UBL)		
Daytime / nighttime UBL height	Calibrated	Literature values adapted to Turin (1000 m / 80 m)
Phenological period	Calibrated	April–October
Urban Canopy & Building Energy Model (UC-BEM)		
Urban morphology (SC, VtH, ABH, characteristic length)	Computed	GIS analysis on DBTRE cadastral database
Vegetation cover (tree and grass fractions)	Computed	Radial buffering and polygon analysis (DBTRE)
Road thermal and optical properties	Calibrated	Literature values for European asphalt
Building archetypes and construction vintage mix	Computed	DOE prototypes mapped on DBTRE semantic metadata
Envelope properties (U-values, SHGC, infiltration)	Calibrated	TABULA-IEE database (Italian building stock)
Internal loads (occupancy, lighting, equipment)	Calibrated	UNI 10339, UNI/TS 11300-1, UNI EN 15193-1
Traffic sensible heat flux	Computed	NO_2 concentration proxy (Respira Torino)
Simulated Outputs		
Urban air temperature T_{urb}	Output	Urbanised EPW file (8760 hourly values)
Urban specific humidity	Output	Canyon vapour balance
UHI intensity $\Delta T = T_{\text{urb}} - T_{\text{rural}}$	Output	Derived per spatial unit, hourly resolution

Chapter 5

Result and Model Evaluation

5.1 Model Validation: Comparison with Field Measurements

The methodology was validated in Turin's historic center, specifically within the Consolata district. This site hosts the ARPA Piemonte weather station (45.07583° N, 7.67833° E, 240 m a.s.l.), providing the hourly temperature time series necessary for the analysis. The sensor is located on the roof of the host building. For this analysis, data from the entire year 2024 was extracted and processed. Specifically, the urban district was modelled using two different spatial discretisation strategies: a regular grid and a partition based on morphological blocks. A comparison was made between the simulation results and the measured data in the spatial units containing the measurement point of the station (Figure 5.1). Further analysis regarding the positioning of the station within the calculation cell is available in the Appendix A.3.



(a) 200x200 m regular grid **(b)** morphological block

Figure 5.1: Spatial validation of the weather station location in the Consolata area.

Validation requires comparing two sets of data with different time conventions: the UWG output, in .EPW format, and the ARPA measurement network, in .csv format. To ensure physical consistency, three-level harmonisation was applied:

- **Time zone unification** (from UTC to UTC+1): The ARPA data (originally in UTC) was transposed to a fixed UTC+1 reference (local solar time). This aligns with the EnergyPlus engine, which uses local solar time without seasonal adjustments for daylight saving time (DST).
- **Aggregation convention** (from the end of the hour to the beginning of the hour). The EPW format follows the 'end of hour' convention (where timestamp n represents the average of the interval [n-1, n]), while ARPA sensors provide data referring to the beginning of the hour. To resolve this discrepancy, the simulated data was shifted by -1 hour, maximising the cross-correlation ($r = 0.989$).
- **Residual daylight saving time anomaly in March**. Analysis reveals a slightly negative mean bias error (MBE) in March of -0.092 K. This is identified as a structural numerical artefact rather than a limitation of the

physical model. Switching to daylight saving time (UTC+2) in the last week of March introduces a time shift of 22 hours at the end of the month. Due to the significant hourly temperature variations in spring, this one-hour shift is sufficient to generate a negative bias in the monthly average.

To assess the reliability of the results, two error metrics were adopted:

- **Root Mean Square Error** (RMSE). The RMSE represents the standard deviation of the residuals (differences between simulated, T_{sim}, and observed values, T_{real}). It is a measure of the accuracy of the model and indicates the average magnitude of the error. It is calculated as follows:

$$RMSE = \sqrt{\frac{\sum_{i=1}^{n}(T_{sim,i} - T_{real,i})^2}{n}} \tag{5.1}$$

- **Mean Bias Error** (MBE). The MBE measures the systematic error (bias) of the model. It indicates the simulator's tendency to systematically overestimate or underestimate the actual temperature over the entire period analyzed. It is calculated as:

$$MBE = \frac{\sum_{i=1}^{n}(T_{sim,i} - T_{real,i})}{n} \tag{5.2}$$

5.1.1 Monthly Statistical Performance: Grid vs. Morphological Discretization

Table 5.1 summarizes the hourly Root Mean Square Error (RMSE) and Mean Bias Error (MBE) for the two simulated configurations, Grid (G) and Morphological Block (MB).

Table 5.1: Hourly validation metrics for the G and MB configurations. Values relative to ARPA 2024 measurements.

Month	**RMSE**$_G$ **[K]**	**MBE**$_G$ **[K]**	**RMSE**$_{MB}$ **[K]**	**MBE**$_{MB}$ **[K]**	**Improv. [%]**
January	1.508	+0.499	1.422	+0.279	5.74
February	1.297	+0.499	1.213	+0.361	6.48
March	0.989	+0.010	0.956	−0.092	3.31
April	1.213	+0.056	1.183	+0.024	2.47
May	0.988	+0.230	0.950	+0.215	3.82
June	1.037	+0.272	0.994	+0.285	4.10
July	0.970	+0.227	0.879	+0.216	9.42
August	1.496	+0.891	1.398	+0.818	6.57
September	1.057	+0.262	1.001	+0.256	5.30
October	0.779	+0.182	0.738	+0.134	5.33
November	1.503	+0.627	1.381	+0.436	8.14
December	1.350	+0.419	1.254	+0.221	7.08
ANNUAL AVG	**1.182**	**+0.348**	**1.114**	**+0.263**	**5.77**

On an annual basis, the UWG model shows an average hourly root mean square error (RMSE) of 1.182 K for the Grid (G) configuration and 1.114 K for the Morphological Block (MB) configuration. The respective annual MBE results are +0.348 K and +0.263 K, indicating a limited but systematic overestimation of air temperature compared to actual measurements taken throughout the year. These results are fully in line with the accuracy ranges documented in the literature. For example, Hamdi et al. [31] reported RMSE values between 0.9 K and 1.5 K and generally positive MBE values in the range of 0.2–0.5 K in the original validation of the UWG model in European urban sites (Basel and Toulouse). Similarly, Boccalatte et al. [32] documented an hourly RMSE in the range of 1.0–1.6 K when applying the model to the Geneva context.

As can be seen in Figure 5.2, the Morphological Block (MB) configuration offers consistently superior performance to the standard Grid (G) approach. Specifically, the MB strategy reduces the RMSE for each month of the year, achieving an improvement of 9.42% in July. The MB trend shows that, while there is slight overestimation of temperatures in both cases, the MB configuration has a reduced

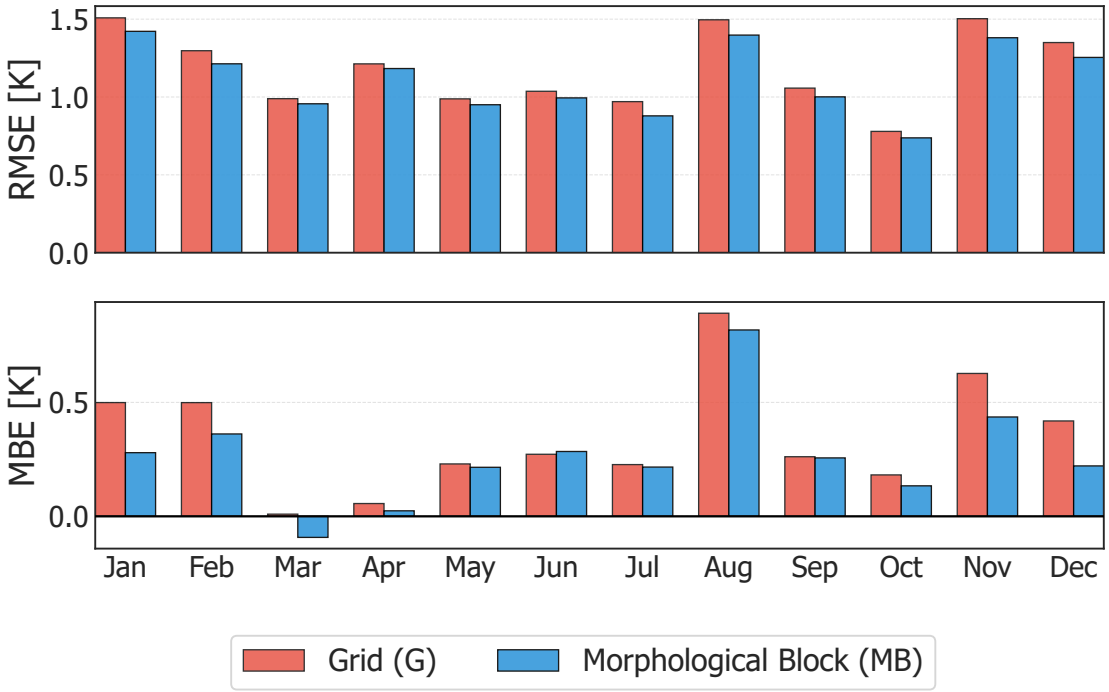


Figure 5.2: Comparison of hourly RMSE and MBE across the simulation months for Grid (G) and Morphological Block (MB) configurations.

bias for 11 out of 12 months. As mentioned above, the only instance of negative bias occurs in March, which confirms the robustness of the adopted time alignment strategy. The monthly analysis reveals significant seasonal variation in the model's accuracy. The transition months, particularly October ($RMSE_{MB}$ = 0.738 K), May ($RMSE_{MB}$ = 0.950 K) and April ($RMSE_{MB}$ = 1.183 K), show the best performance, with errors below or close to 1.0 K. In contrast, August ($RMSE_{MB}$ = 1.398 K) and the winter months, January ($RMSE_{MB}$ = 1.422 K), November ($RMSE_{MB}$ = 1.381 K) and December ($RMSE_{MB}$ = 1.254 K), show the highest deviations. The peak in August may reflect an inherent limitation in modelling anthropogenic loads. The current model configuration assumes constant heat release profiles (from traffic and HVAC systems) throughout the year. However, the significant reduction in anthropogenic activities in August may cause the model to overestimate the heat input into the system.

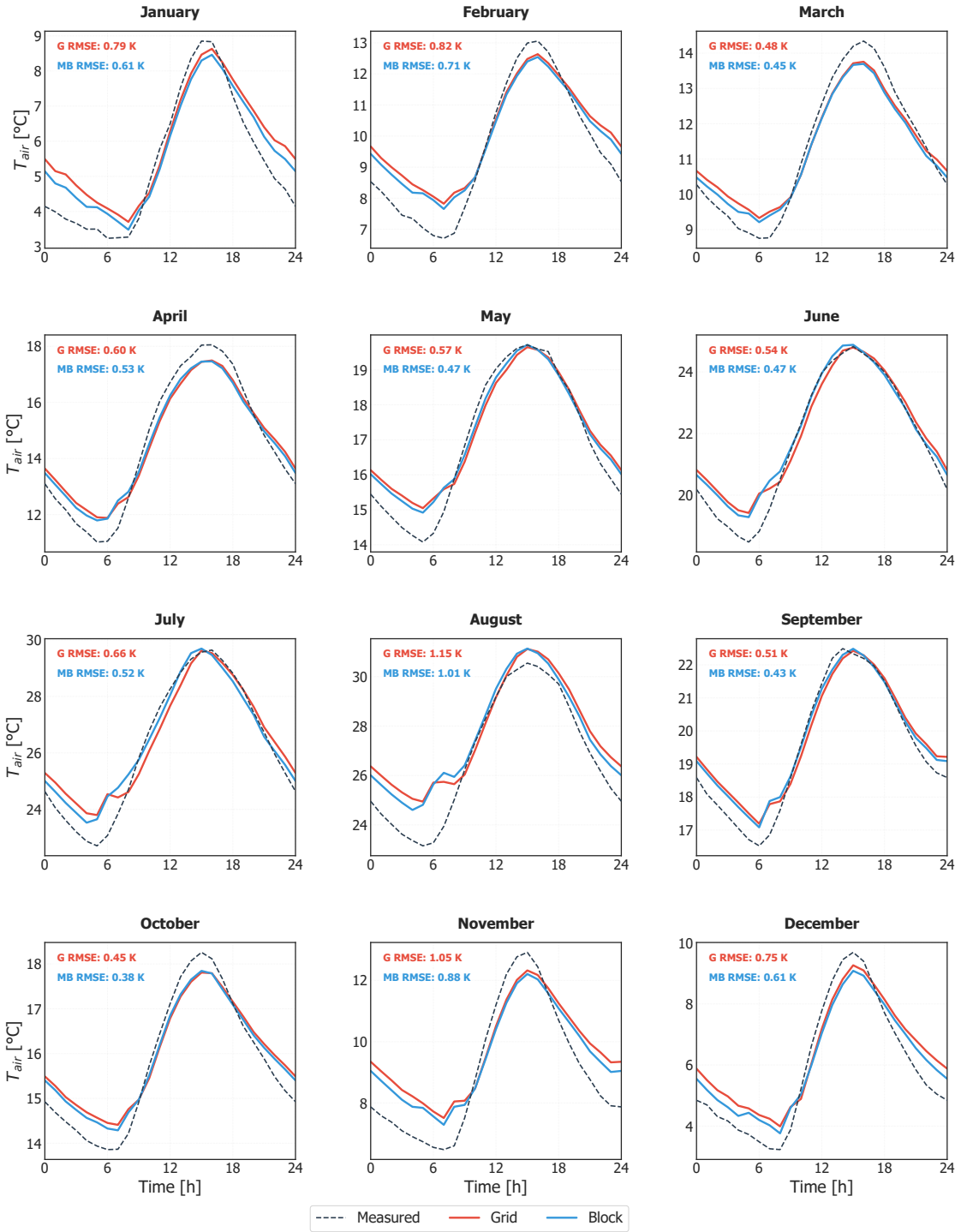


Figure 5.3: Monthly average hourly air temperature profiles: comparison between Grid (G), Morphological Block (MB), and observed ARPA data (Consolata).

Note: The RMSE and MBE values displayed within each subplot are calculated based on the monthly average profiles to evaluate the model's accuracy in replicating the characteristic diurnal thermal cycle.

The average hourly profiles (see Figure 5.3) show that the MB configuration more accurately follows the night-time cooling curve than the G configuration. This improvement in metrics (RMSE reduced by 5.77% on an annual basis) confirms that integrating morphological parameters that better capture the actual geometry allows for more accurate modelling of heat exchange between buildings and urban canyons. Nevertheless, the model still tends to underestimate daytime peaks and overestimate night-time temperatures. This phenomenon can be attributed to the difference in scale between the ARPA station's point measurement and the UWG's average temperature over the entire urban canyon volume (canopy layer). In complex urban contexts, local micro-variations in shading and different radiation regimes between street level and higher elevations can introduce discrepancies that are not reflected in the available data. Nevertheless, the overall results are fully consistent with the accuracy ranges documented in the literature for models of a similar complexity, which confirms the robustness of the validation procedure.

5.1.2 Representative Day Analysis and Extreme Event Validation

To supplement the monthly statistical analysis, the model's response was evaluated under two meteorologically contrasting scenarios: an **extreme heat event** (27–30 July 2024) and a **winter cold pool episode** (14–16 December 2024). The multi-day window was selected in both cases to assess the model's resilience under prolonged thermal stress, rather than limiting the analysis to a single representative day.

Summer Heat Wave

Figure 5.4 presents the four-day period centered on the extreme heat event of 28 July 2024, including the rural reference temperature (Caselle weather station, 45.19206° N, 7.65189° E, 285 m a.s.l.). It is observed that the spatial configuration of the morphological block reproduces the urban temperature with high fidelity over the analyzed period, achieving error metrics of RMSE = 0.802 K and MBE = +0.119 K. The rural–urban temperature differential shown in Figure 5.4 confirms the presence of a sustained nocturnal urban heat island, with the rural station at Caselle reaching minimum temperatures significantly below those recorded at the urban Consolata station. The residual analysis (lower plot in Figure 5.4) reveals a structured diurnal pattern: a nocturnal overestimation of approximately +1 K

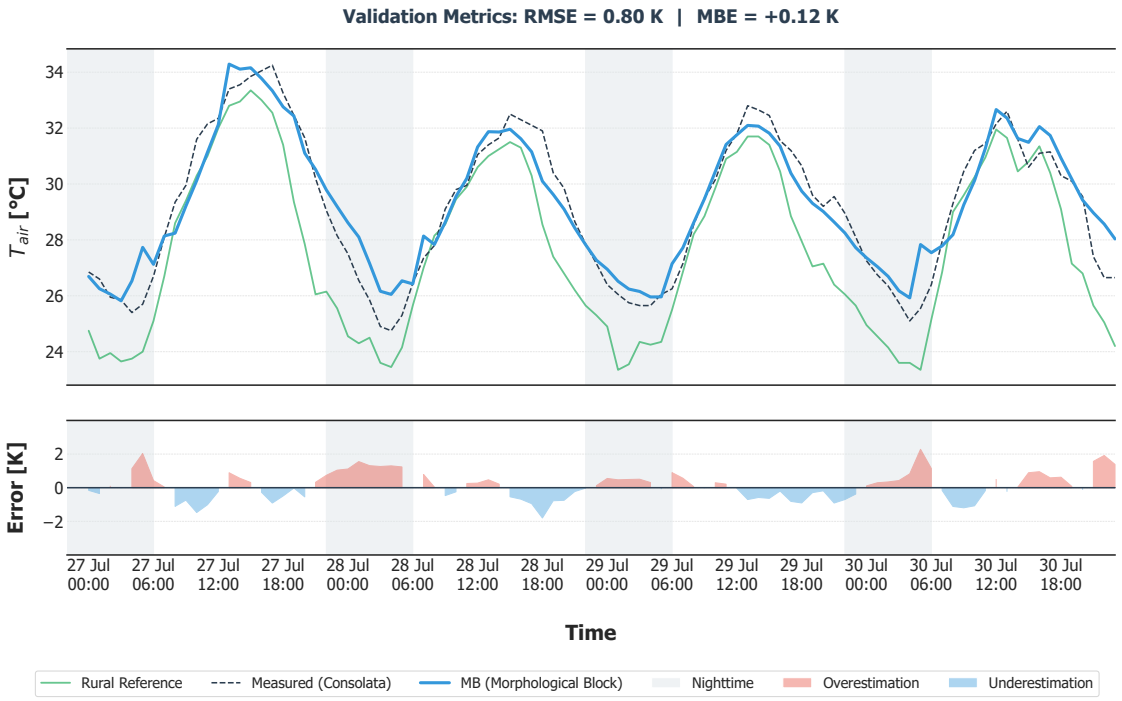


Figure 5.4: Detailed validation of the Summer Heat Wave period (27–30 July 2024).
Top: comparison between measured, rural, and simulated (MB) temperatures. Bottom: hourly residual analysis highlighting overestimation and underestimation.

is followed by a near-zero error phase during the morning transition and a slight underestimation of the afternoon peak.

This diurnal error structure is consistent with the known behaviour of single-layer canopy models under strongly convective summer conditions: the bulk-mixing parametrisation adequately captures the nocturnal thermal storage release but cannot fully resolve the peak convective boundary layer response to maximum solar forcing, leading to a systematic underestimation of the afternoon temperature maximum [30].

Extreme Cold and Winter Cold Pool

The winter validation scenario (see Figure 5.5) represents the most significant challenge for the model, showing a performance degradation compared to the summer case. During the period of 14–16 December, the measured data reveal a sharp thermal decoupling: the rural station records minimum temperatures as low as -4°C, while the urban station consistently remains above 0°C. Over this three-day period, the MB configuration achieves an RMSE of 1.528 K and an MBE of +0.658 K.

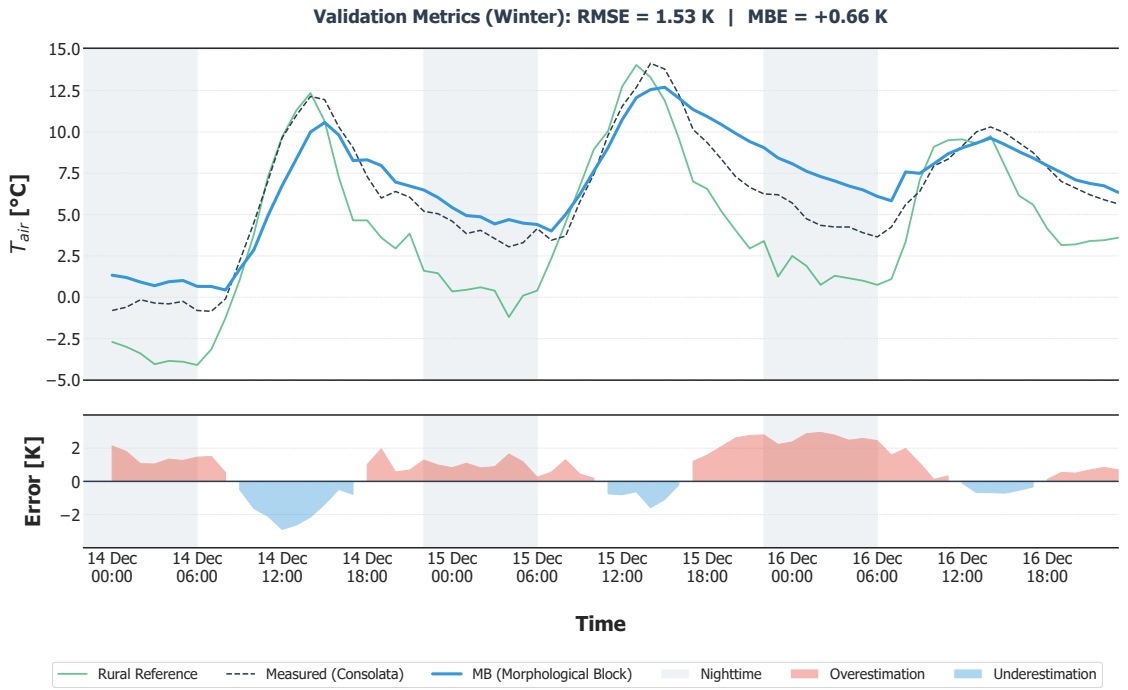


Figure 5.5: Detailed validation of the Winter Cold Pool period (14–16 December 2024).

Top: comparison between measured, rural, and simulated (MB) temperatures, highlighting the thermal decoupling between site and airport. Bottom: hourly residual analysis illustrating the systematic nocturnal overestimation during stable atmospheric conditions.

The residual analysis highlights two primary deviations from the observed data:

- **Systematic Nocturnal Overestimation**. During the night-time hours of 15 and 16 December, the model fails to replicate the observed cooling rate. While the measured temperature (dashed black line) drops sharply, the simulation (blue line) exhibits a flatter trend, resulting in a systematic warm bias that peaks at approximately +2 K.

- **The 14 December Anomaly**. A significant underestimation episode (up to -2.5 K) is observed on the afternoon of 14 December, coinciding with a sudden and sharp increase in the rural reference temperature. The model appears overly sensitive to this specific input variation, propagating the rural warming into the urban domain more aggressively than what is recorded on-site.

The evidence suggests that the model's error is functionally linked to its dependence on the rural reference station. When the rural input exhibits extreme

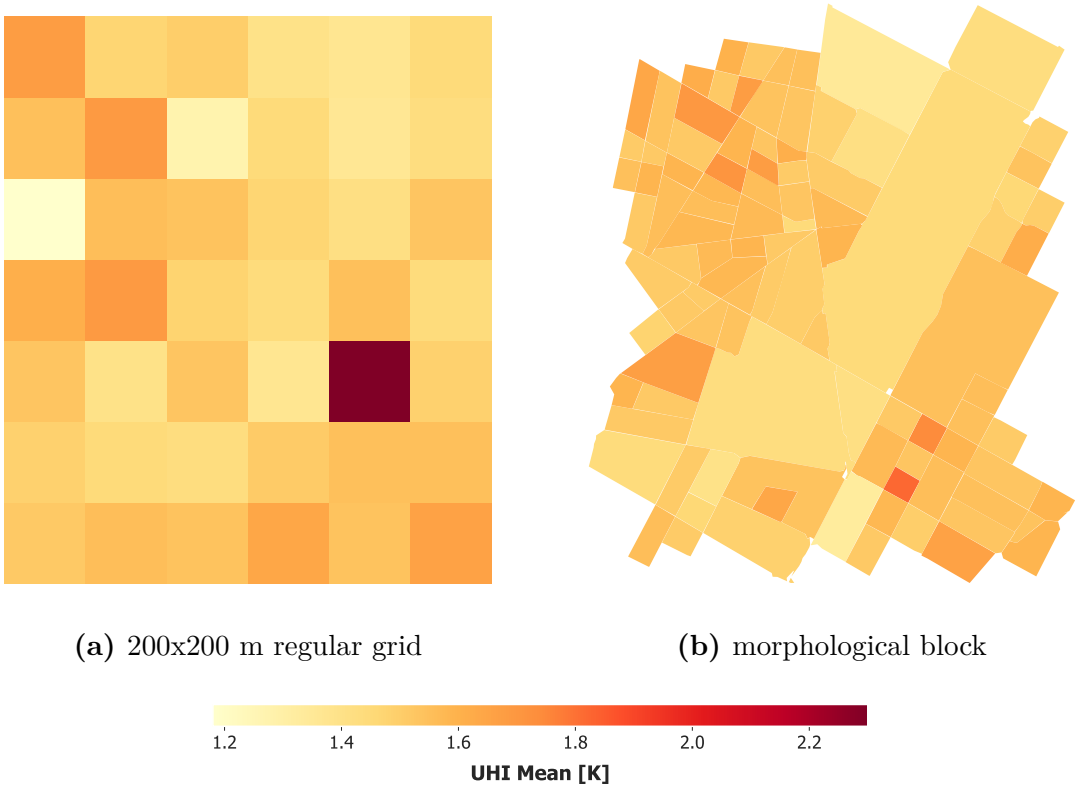
fluctuations, the simulation fails to maintain the thermal independence of the urban microclimate, leading to results that are excessively anchored to the external forcing. These findings indicate that the discrepancies are inherent to the model's response to rural inputs during winter, and cannot be fully mitigated by refining the morphological parameters of the urban block.

The comparative analysis across the two extreme seasonal scenarios reveals that the model's accuracy is governed primarily by the prevailing atmospheric stability regime rather than by the morphological parametrisation. Under convective summer conditions, where the well-mixed canopy assumption is physically appropriate, the MB configuration achieves high fidelity (RMSE = 0.802 K, MBE = +0.119 K). Under stable winter stratification, the single rural reference assumption introduces a systematic warm bias (RMSE = 1.528 K, MBE = +0.658 K) that cannot be resolved through morphological refinement alone.

A critical finding of this validation is that in both scenarios the MB model provides a substantially more accurate representation of the urban thermal environment than the rural reference station alone, which deviates from the urban measurements by over 5 K during the winter cold pool. This confirms the model's ability to bridge the urban–rural thermal gap across contrasting atmospheric regimes, and validates the MB configuration as a robust tool for urban climate assessment in Turin. The structural limitations identified — nocturnal overestimation under stable winter conditions and slight afternoon underestimation under peak summer forcing — are consistent with the known constraints of UWG-class models [30] and are addressed in the Discussion.

5.2 Urban Heat Island Mapping and Spatial Characterization

Using the UWG model for the whole PED area enabled a map of the Urban Heat Island to be created (see Figure 5.6), with the results obtained using a 200-metre regular grid (G) systematically compared with those based on morphological blocks (MB). The analysis focused on the core area of the domain to eliminate edge effects and ensure statistical comparability between the two methods.



(a) 200x200 m regular grid **(b)** morphological block

Figure 5.6: Comparative UHI maps between G and MB.

While both configurations yield similar annual average UHI values (Table 5.2), with a negligible difference of -0.029 K (2%), their spatial variability diverges considerably. The standard deviation of the grid-based simulation ($\sigma = 0.162$K) is more than double that obtained using morphological blocks ($\sigma = 0.074$ K), indicating greater dispersion of values when the urban domain is discretised using regular cells.

Table 5.2: Comparative UHI Statistics (Core Area): Grid (G) vs Morphological Block (MB).

Parameter	G	MB	Difference
Mean UHI [K]	1.514	1.543	-0.029 (-2%)
Standard Deviation σ [K]	0.162	0.074	+0.088 (+119%)

A thorough analysis of the local bias between the two methods ($UHI_{Grid} - UHI_{MB}$) reveals point-by-point deviations of up to approximately ± 0.14 K, while the area-weighted average bias is found to be close to zero (0.007 K). This finding

indicates that discretisation does not introduce systematic distortion in the overall UHI estimate, but may locally alter the representation of urban thermal heterogeneity. The grid, intersecting the urban built fabric randomly, generates cells that do not correspond to the actual functional unit. Conversely, MB (Morphological Blocks) discretization engenders a more compact distribution that is physically consistent with the built environment.

To further substantiate this methodological divergence, the analysis was extended to a monthly scale (Table 5.3). The results confirm that the UHI follows a marked seasonal cycle, peaking in the winter months (November, $\overline{UHI}_{MB} = 2.244$ K) and reaching its minimum in spring (May, $\overline{UHI}_{MB} = 1.004$ K).

Table 5.3: Full monthly UHI statistical metrics and Dispersion Ratio comparison (Core Area).

Month	**Mean**$_G$ **[K]**	**Mean**$_{MB}$ **[K]**	**Std**$_G$ **[K]**	**Std**$_{MB}$ **[K]**	**Ratio** σ	**Bias [K]**
January	1.886	1.922	0.250	0.133	1.884	−0.036
February	1.739	1.782	0.171	0.079	2.164	−0.043
March	1.157	1.197	0.153	0.068	2.246	−0.040
April	1.369	1.403	0.131	0.060	2.190	−0.034
May	0.980	1.004	0.116	0.047	2.464	−0.024
June	1.184	1.202	0.128	0.057	2.261	−0.018
July	1.290	1.314	0.170	0.087	1.949	−0.023
August	1.777	1.807	0.183	0.087	2.103	−0.030
September	1.364	1.385	0.120	0.047	2.570	−0.021
October	1.041	1.069	0.120	0.051	2.368	−0.027
November	2.216	2.244	0.199	0.108	1.839	−0.027
December	2.187	2.222	0.252	0.135	1.863	−0.035
Annual Avg	**1.453**	**1.487**	**0.166**	**0.080**	**2.160**	**-0.030**

The monthly metrics highlight a structural limitation of the regular grid: the **Dispersion Ratio** (σ_G/σ_{MB}) consistently exceeds 1.8 across all months, peaking at 2.57 in September. Furthermore, the grid exhibits a systematic negative bias (averaging −0.03 K), suggesting that regular cells tend to dilute localized thermal hotspots by averaging heterogeneous built-up volumes with open urban spaces.

The spatiotemporal evolution illustrated in the monthly maps (Figure 5.8) and the associated boxplot (Figure 5.7) confirms that while the magnitude of the UHI is seasonally dependent, the **spatial thermal hierarchy is persistent**. Densely built blocks consistently record higher intensities regardless of the season, validating

the MB approach as a more stable and physically coherent tool for capturing the intrinsic relationship between urban morphology and microclimate. In addition, a detailed spatial visualization contextualizing the UHI distribution relative to the physical urban fabric and existing greenery is provided in Appendix A.4 for further reference.

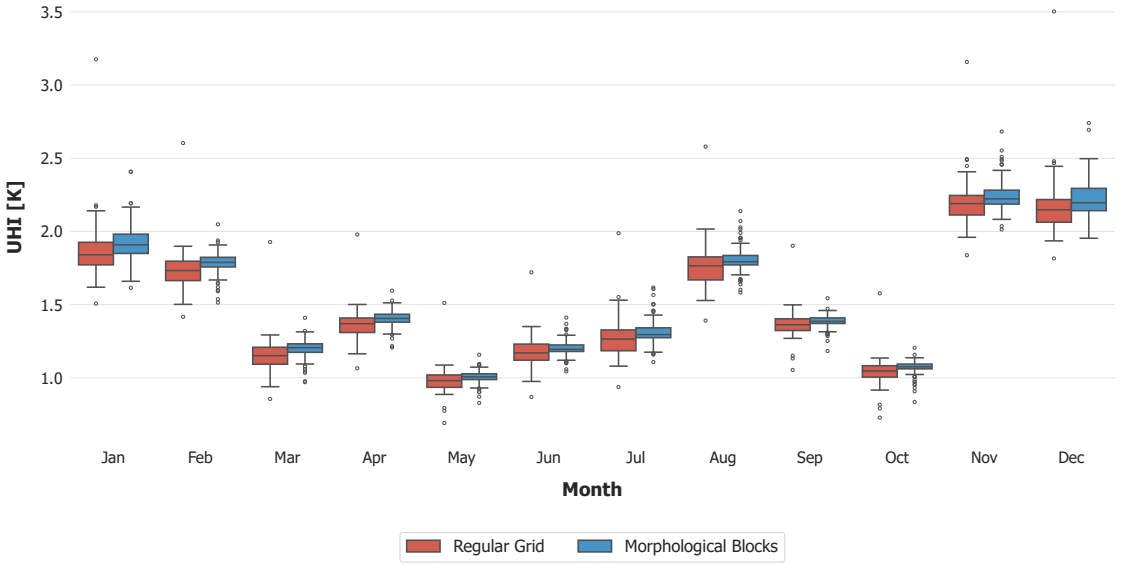


Figure 5.7: Boxplot comparison of UHI: Grid vs Morphological Blocks.

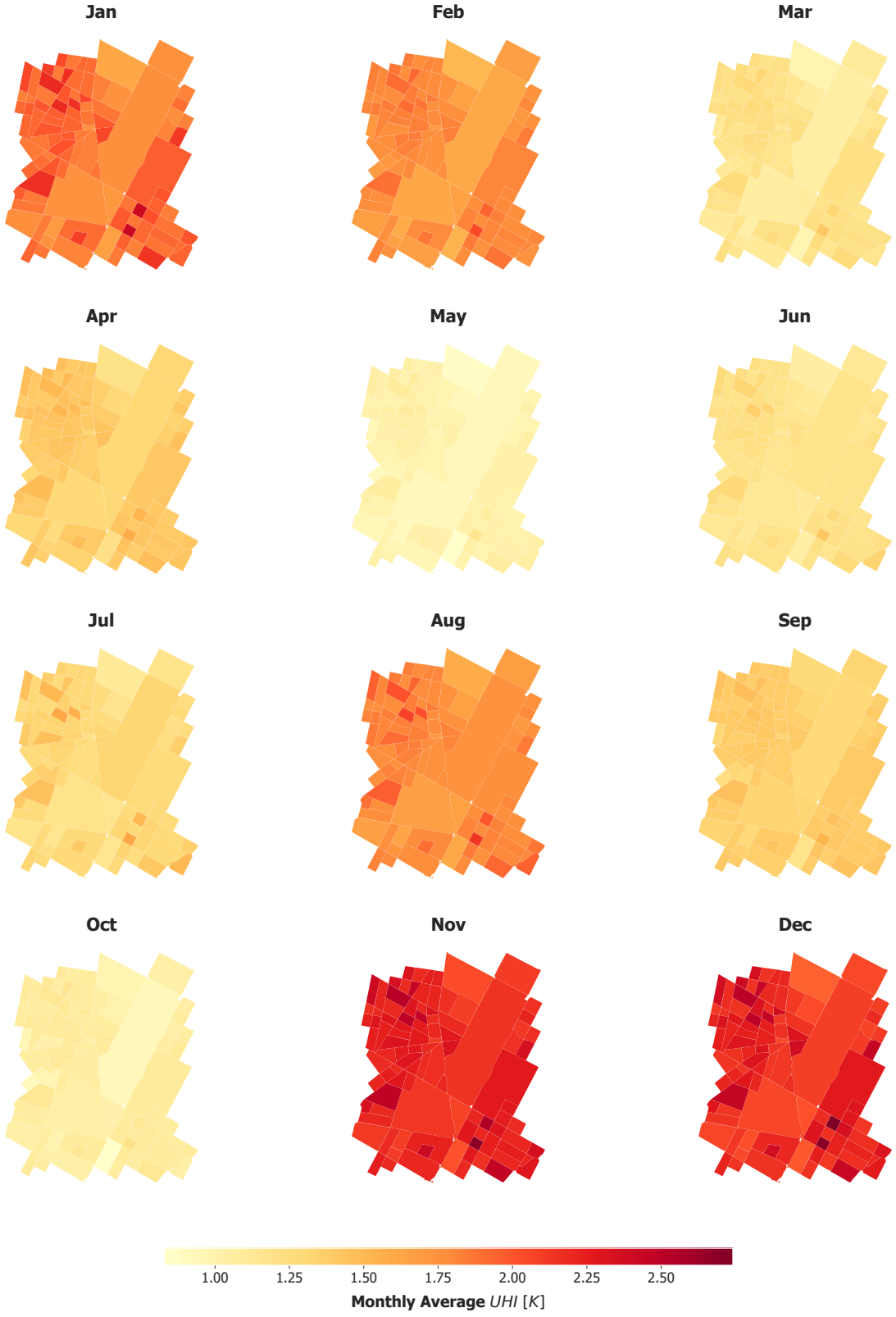


Figure 5.8: Monthly UHI maps calculated via morphological blocks.

5.2.1 Quantification of Discretization Bias

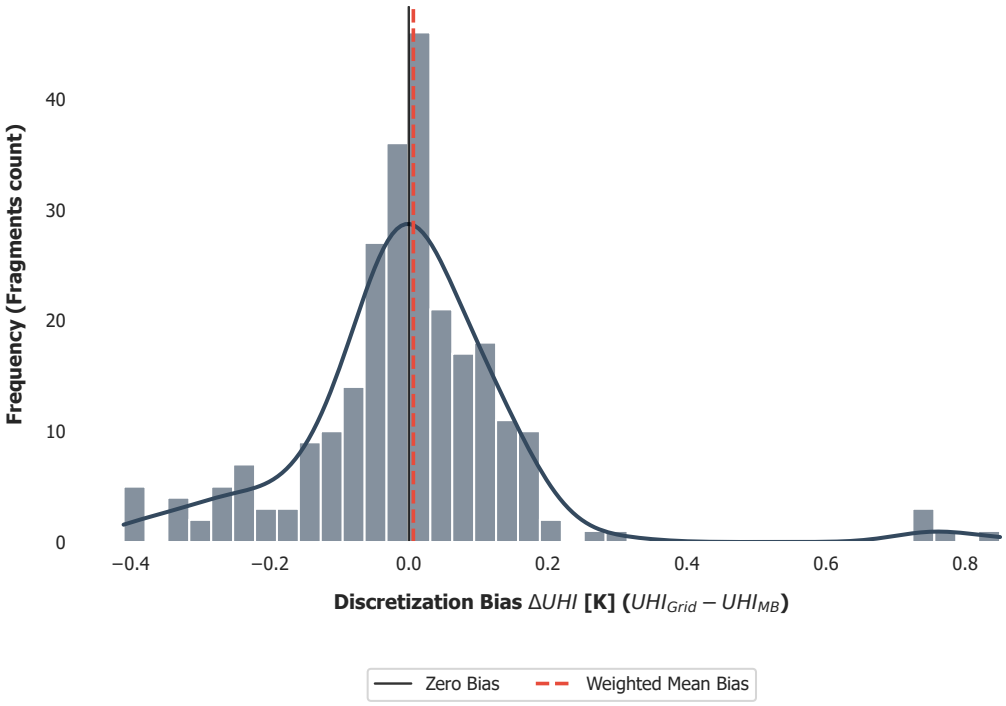
In order to rigorously quantify the bias introduced by spatial discretization, the analysis was extended to all units in the domain using a geometric overlay operation between the two partitions. Specifically, for each regular grid cell, the weighted average of the UHI of the contained morphological blocks ($\mathrm{UHI}_{\mathrm{MB,\ weighted}}$) was determined, using the intersection area as the weighting factor (w_i):

$$\mathrm{UHI}_{\mathrm{MB,weighted}} = \frac{\sum_i (\mathrm{UHI}_i \cdot w_i)}{\sum_i w_i}, \quad \text{where} \quad w_i = \frac{A_{\mathrm{intersection},i}}{A\mathrm{grid}} \tag{5.3}$$

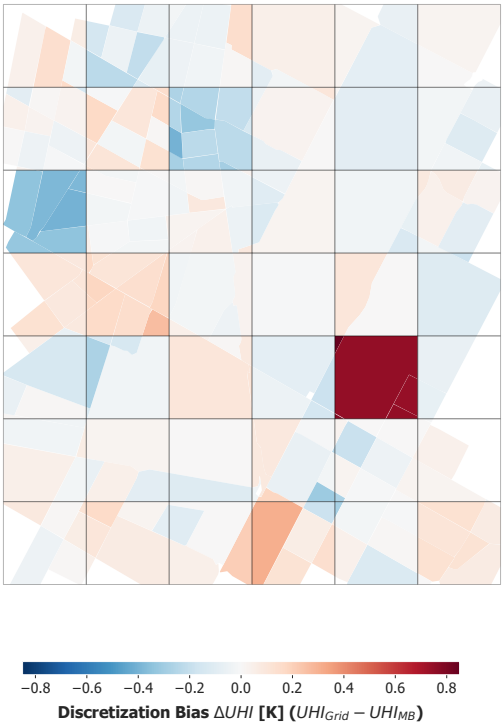
This approach ensures that the comparison is based on equivalent spatial masses, isolating the influence of geometric resolution from that of total built volume.

The local bias is therefore defined as $\Delta\mathrm{UHI} = \mathrm{UHI}_{\mathrm{Grid}} - \mathrm{UHI}_{\mathrm{MB,weighted}}$. The classification adopted distinguishes three regimes:

- overestimation ($\Delta > +0.15$ K),
- underestimate ($\Delta < -0.15$ K)
- convergence ($\Delta \leq 0.15$ K).



(a) UHI Bias Frequency Distribution



(b) Spatial Discretization Bias Map

Figure 5.9: UHI Bias Analysis – Histogram and Spatial Distribution.

The tolerance of ±0.15 K has been defined taking into account the sensitivity typical of thermo-hygrometric sensors for the monitoring of the microclimate and the intrinsic uncertainty of the models used by Urban Canopy. This value represents the limit below which the discrepancies between the two methods are considered residual noise from discretisation, devoid of impact significant on the estimate of the energy requirement of the district.

As shown in Figure 5.9, the spatial distribution of the biases highlights two systematic effects associated with the regular grid discretization. While the majority of the domain converges toward coherent results, a significant minority of units exhibits marked deviations (Table 5.4).

Table 5.4: Ranking of the highest UHI Discrepancies (Top Cells by Absolute Bias).

ID	UHI_G **[K]**	UHI_{MB} **[K]**	**Bias [K]**	**Category**
Cell 50	2.300	1.526	+ 0.774	OVERESTIMATED
Cell 15	1.180	1.549	- 0.369	UNDERESTIMATED
Cell 34	1.280	1.540	- 0.260	UNDERESTIMATED
Cell 23	1.690	1.524	+ 0.166	OVERESTIMATED
Cell 25	1.690	1.594	0.096	COHERENT

The limitation of the regular grid does not lie in a systematic computational error, but in localized failures occurring at specific morphological configurations (see Figure 5.10). The two extreme cases identified — **Cell 50** (overestimation of +0.77 K) and **Cell 34** (underestimation of −0.26 K) — represent the "corner cases" of geometric aliasing and are analyzed in detail in the following section.

Root Causes of Local Discretization Bias

Cell 50 records the largest bias within the entire domain (+0.774 K). The analysis of the morphological parameters (see Table 5.5) reveals a systematic distortion in the input representation. The regular grid estimates a Surface Coverage (SC) of 0.811, corresponding to an ultra-compact urban fabric. In contrast, the morphological blocks (MB) contained within the same cell exhibit SC values ranging between 0.193 and 0.378.

This geometric aggregation effect propagates through the UWG energy balance. Since the model estimates anthropogenic building heat emissions (q_{bldg}) as a function of built density, the grid assigns Cell 50 a theoretical emission of $123.46 W/m^2$,

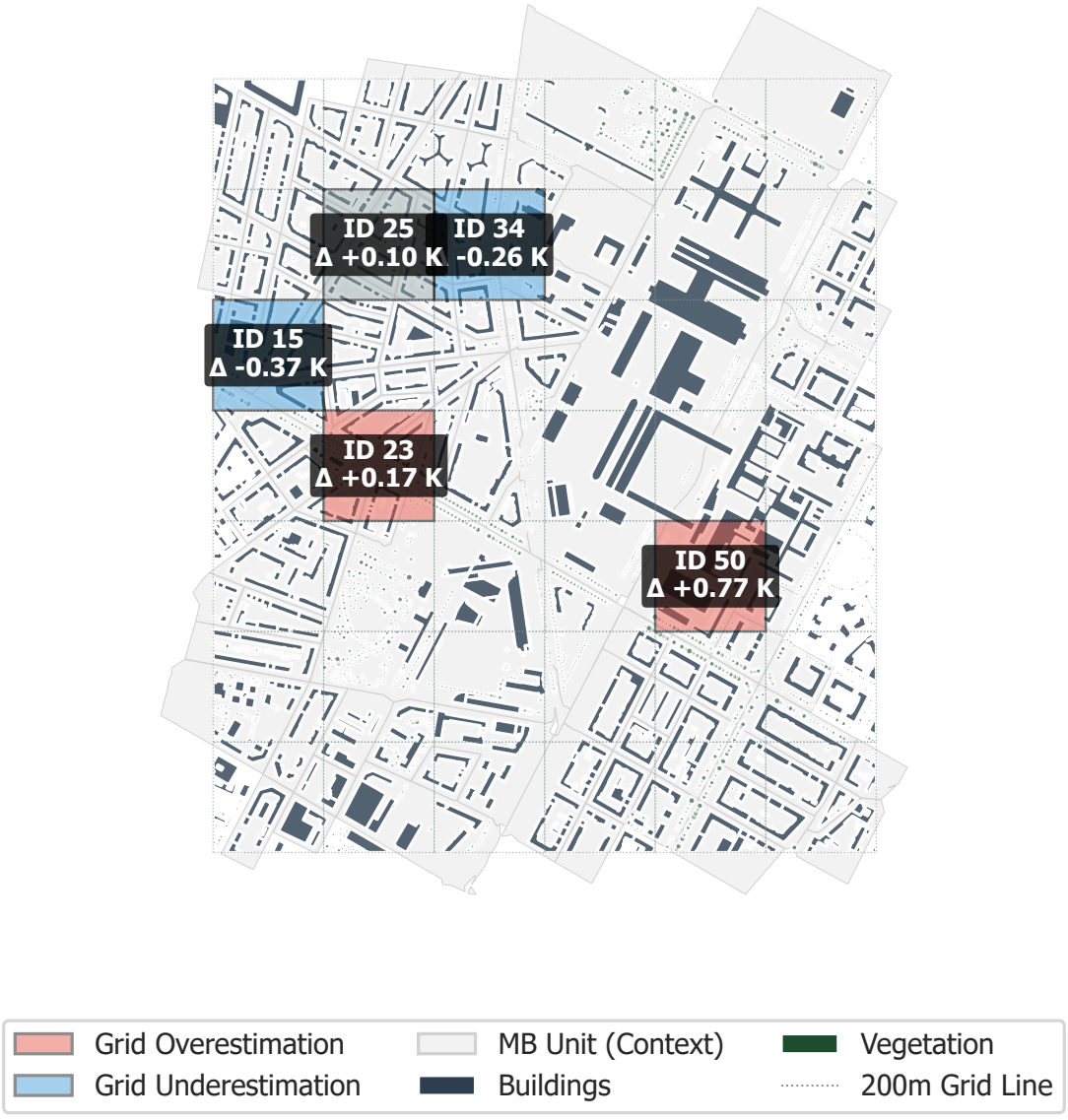


Figure 5.10: Detail of bias analysis for specific representative cells.

whereas the corresponding MB units produce values of approximately $30-50 W/m^2$. This discrepancy suggests that the limitation of the grid representation is not only related to spatial resolution but also to the geometric aggregation of urban morphology, which may lead to unrealistic anthropogenic heat loads and an amplified simulated UHI intensity.

Table 5.5: Morphological and energetic drivers of overestimation in Cell 50.

Unit ID	UHI [K]	SC [-]	V/H [-]	H/W [-]	q_{bldg} [W/m^2]
Grid 50	**2.300**	**0.811**	**1.802**	**63.495**	**123.46**
Iso 0 (Min UHI)	1.450	0.298	0.449	4.000	32.79
Iso 22 (Max UHI)	1.560	0.193	1.432	8.480	29.15
MB Weighted Avg	*1.526*	*0.312*	*0.854*	*5.842*	*46.07*

The case of Cell 34 (ΔUHI $= -0.260$ K) illustrates the tendency of the grid representation to smooth local thermal heterogeneity (see Table 5.6). In this case, the grid averages and dilutes the thermal contribution of localized hotspots. In particular, Block 141 exhibits significantly more severe morphological parameters ($V/H = 1.639$, $SC = 0.380$) and a simulated UHI intensity of 1.68 K. The grid representation, limited to a mean value of 1.28 K, masks the thermal risk associated with this specific block and may lead to an underestimation of peak cooling demand.

Table 5.6: Spatial smoothing effect in Cell 34: masking of local thermal hotspots.

Unit ID	UHI [K]	SC [-]	V/H [-]	Avg Height [m]	q_{total} [W/m^2]
Grid 34	**1.280**	**0.283**	**1.390**	**15.57**	**37.59**
Iso 141 (Hotspot)	1.680	0.380	1.639	14.73	38.17
Iso 58 (Open area)	1.420	0.130	0.337	19.33	32.21
MB Weighted Avg	*1.540*	*0.283*	*1.341*	*16.82*	*39.42*

The robustness of the comparison is further supported by a volumetric invariance test performed on an additional cell identified as having the highest agreement between the grid-estimated built volume and the aggregated volume of the morphological blocks. The discrepancy between the two volumes is below 0.4%, effectively excluding differences in bulk material inputs as the primary explanation for the remaining thermal discrepancies.

The fact that the two models generate distinct thermal responses provides strong evidence that UHI intensity is not solely governed by the total thermal mass of the urban fabric, but also by its geometric configuration. In this context, the MB discretization appears to better preserve the spatial resolution required to correctly simulate surface radiative exchanges within the urban canyon.

5.3 Sensitivity Analysis: Microclimate Drivers across Urban Archetypes

To evaluate the response of the implemented model and identify the variables that most strongly govern the urban microclimate within the analysed area, a multi-parameter sensitivity analysis was conducted. This approach is based on archetypes identified within the dataset to ensure that the simulations reflect real elements of the urban fabric. Following the OFAT (One-Factor-At-A-Time) logic, each variable was modified individually with respect to a baseline configuration to isolate its net thermal effect. To identify the four representative boundary cases (see Table 5.7), a statistical approach based on quartiles of morphological properties such as density and height was implemented. As the case study is characterised by a predominantly dense building network, this segmentation enables clear separation between the archetypes.

Table 5.7: Classification of Urban Archetypes based on Density and Height quartiles.

	Low Height (Q_1)	**High Height (Q_3)**
Compact (Q_3)	Low-Compact	High-Compact
Scattered (Q_1)	Low-Scattered	High-Scattered

To carry out the analysis under equal conditions, the thermophysical properties were normalized. All prototypes were simulated as **midrise apartments**, adopting the most frequent construction era in the dataset, namely the **pre-1980 period**. The other specific morphological and geometric properties assigned to the spatial units are summarized in Table 5.8.

Table 5.8: Morphological characteristics of the four selected urban archetypes.

Archetype	**Avg. Height** [m]	**Surface Coverage** [%]	**Vert. to Horiz.** [-]
High-Compact	18.93	38.00	1.74
High-Scattered	145.23	3.00	0.64
Low-Compact	6.25	53.00	0.41
Low-Scattered	8.59	7.00	0.08

A Pearson correlation analysis (see Figure 5.11) of nine variables extracted from the database of blocks was conducted to guide the selection of parameters for the stress test, with the aim of identifying a non-redundant set of parameters. The analysis revealed the following indicators:

- **Building morphology**: represented by the vertical-to-horizontal ratio (V/H).
- **Urban greenery**: accounted for by the vegetation density within the urban area ($green_ratio$).
- **Radiative properties**: defined by the average surface albedo ($albedo_avg$).
- **Anthropogenic emissions**: characterized by the total heat flux (q_{total}).

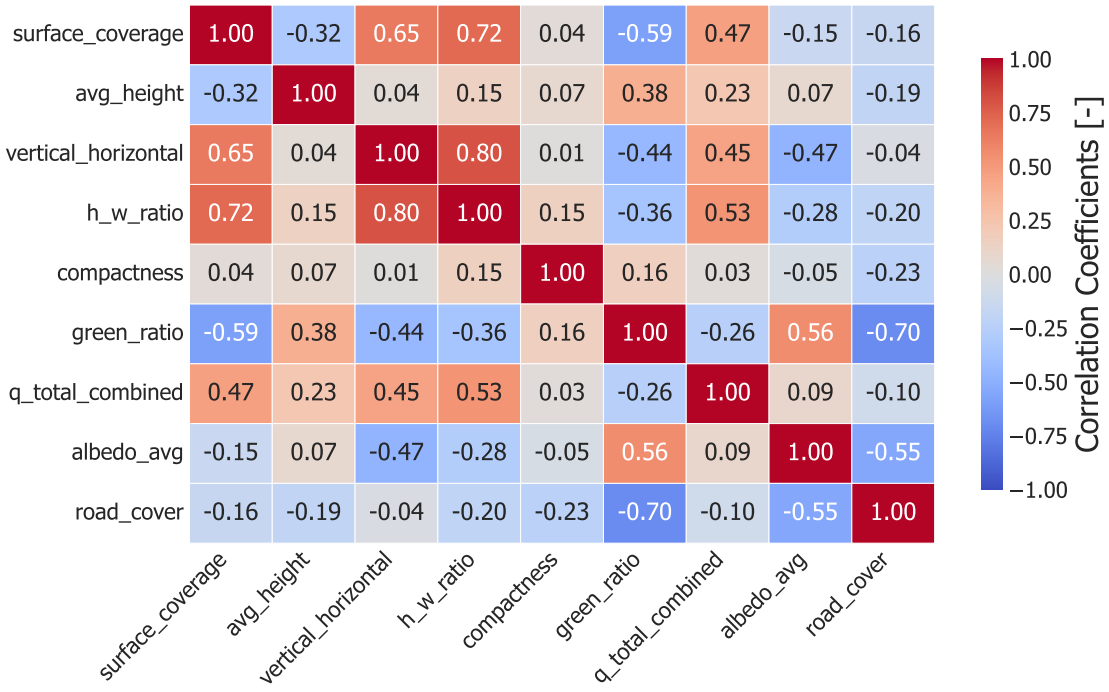


Figure 5.11: Pearson correlation matrix between morphological, radiative, and environmental parameters.

For each archetype identified, five scenarios were defined: a baseline configuration and four stress test scenarios, obtained by individually varying the critical parameters according to the values shown in Table 5.9.

The sensitivity analysis was conducted on two levels to capture the complexity of the urban microclimate; in particular, an analysis of seasonal trends on an annual

Table 5.9: Sensitivity Analysis: Stress Test Scenarios and Parameters.

Parameter	Baseline	Test Value	Engineering Rationale
Surface Albedo	0.15	0.65	Implementation of high-reflectance materials (*Cool Roofs*)
Green Cover	10% (tot)	40% (tot)	Alignment with EU Green Deal targets for urban reforestation and evapotranspiration enhancement.
Traffic Heat	20 W/m^2	+40 W/m^2	Assessment of intensified anthropogenic heat flux ($q_{total} = 60$ W/m^2) .
Morphology	V/H_{base}	+0.42	Sensitivity test based on the actual standard deviation (σ) of the Turin urban database.

scale and a stress test on critical days were carried out. As shown by ARPA 2024 data, the focus was placed on July 28 (extreme heat) and December 15 (extreme cold). Since UHI is a predominantly nocturnal phenomenon, the effectiveness of the strategies was evaluated mainly in the time window between 10:00 p.m. and 6:00 a.m. To evaluate the thermal behavior of the archetypes across different temporal scales, the following metrics were calculated:

- **Peak** (UHI_{peak}): the absolute maximum thermal differential recorded within the analyzed period.
- **Night** (UHI_{night}): the average value calculated during the nocturnal window (10:00 p.m. to 06:00 a.m.), representing the period of maximum UHI intensity.
- **Day** (UHI_{day}): the average value during the diurnal period (07:00 a.m. to 09:00 p.m.).
- **24h**: the integrated daily average, providing an overview of the total thermal surplus

To quantitatively assess the impact of the tested parameters, the Relative Variation (Δ_{UHI}) is introduced. This metric expresses how much of the original urban heat surplus is removed (or added) by the applied driver, comparing the variation to the baseline UHI:

$$\Delta_{UHI} = \left(\frac{T_{scen} - T_{base}}{UHI_{base}} \right) \times 100 \quad [\%] \tag{5.4}$$

The baseline analysis highlights a UHI that varies according to season, time of day, and archetypes. In all the analyzed archetypes (see Table 5.10), the UHI appears to be a purely nocturnal phenomenon; between 10 p.m. and 6 a.m., in fact, the temperature differential between urban and rural areas is systematically higher than the daytime average. For example, in the High-Compact archetype in winter configuration, a nighttime intensity of 3.78 K is observed compared to a daytime value of 1.22 K. The magnitude of the phenomenon reaches its peak during the cold season. The average hourly intensity (UHI_{24h}) in winter always exceeds that in summer, just as the maximum peaks (UHI_{peak}) show a shift of about 2 K in favor of winter. Finally, the geometric configuration of the urban fabric emerges as the main driver of UHI intensity. Archetypes characterized by high vertical density show consistently higher thermal values, following a monotonic hierarchy: High-Compact → High-Scattered → Low-Compact → Low-Scattered.

Table 5.10: Seasonal comparison of UHI intensity by morphological archetype (Baseline).

Archetype	**Season**	**UHI$_{Night}$ [K]**	**UHI$_{Day}$ [K]**	**UHI$_{24h}$ [K]**	**UHI$_{Peak}$ [K]**
High-Compact	Winter	3.781	1.217	2.178	9.24
	Summer	3.049	0.578	1.504	7.22
High-Scattered	Winter	3.402	0.964	1.878	9.05
	Summer	2.898	0.435	1.358	7.07
Low-Compact	Winter	3.510	1.061	1.980	9.37
	Summer	3.009	0.533	1.462	7.29
Low-Scattered	Winter	3.160	0.854	1.719	8.62
	Summer	2.670	0.429	1.269	6.78

Note: Summer = Jun-Aug | Winter = Dec-Feb | Night = 22:00-06:00

The interaction between seasonal cycle and morphological parameters defines the extremes of vulnerability in the dataset. The most critical condition occurs in the High-Compact archetype in winter, with a peak intensity of 9.24 K. Conversely, the Low-Scattered configuration in summer represents the case of least impact, with a peak of 6.78 K. The difference of approximately 2.5 K between the two extremes confirms that density planning and thermal inertia management are fundamental levers for controlling the urban microclimate.

Figure 5.12 shows the monthly relative change in urban heat island for the four archetypes extracted under different scenario parameters.

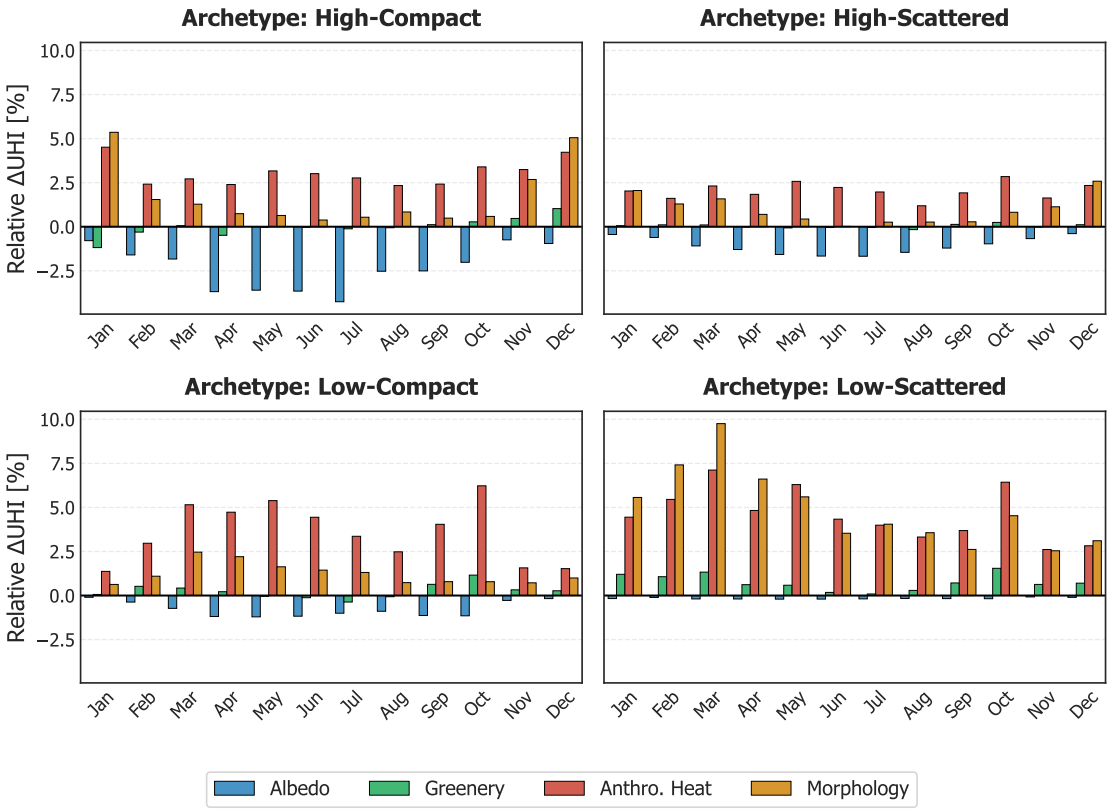


Figure 5.12: Monthly relative change in $\Delta UHI[\%]$ for four urban types and four control factors.

In the **High-Compact** prototype, increasing the albedo provides a consistent cooling effect throughout the year, especially during the spring and summer months (April–July). Anthropogenic heat, acts as a significant warming factor, remaining relatively constant but peaking in winter. Urban morphology has a limited impact, increasing in January and February but always worsens the UHI. The effect of vegetation shows the lowest contribution, if not zero.
The **High-Scattered** prototype exhibits a similar trend, but the magnitude of the impact for all parameters is noticeably attenuated, indicating a lower overall sensitivity of this specific geometry to the tested strategies.
In the **Low-Compact** configuration, anthropogenic heat due to increased traffic becomes the dominant factor, with temperatures rising by up to 6% in October. Morphology continues to contribute to UHI intensification. Once again, increasing green spaces yields no cooling benefits and, in several months, shows a slight warming effect.
Low-Scattered fabrics show the highest values of UHI increase for morphology,

with peaks of increase exceeding 9%. This highlights a strong dependence of the UHI on the spatial structure of less compact buildings. In this archetype, albedo has minimal mitigating effects, while urban greenery consistently exhibits a warming effect across all months, which is physically consistent with reduced wind permeability and long-wave radiation trapping at night.

Table 5.11: Summary of dominant factors impacting UHI intensity per urban archetype.

Urban Typology	**Dominant Factor**	**Peak Month**	**Max ΔUHI Impact**
High-Compact	Anthro. Heat	January / December	∼+5%
High-Scattered	Anthro. Heat	Uniform	∼+2.5%
Low-Compact	Anthro. Heat	October	∼+6%
Low-Scattered	Morphology	March – April	∼+9–10%

The comparative analysis reveals that the effectiveness of mitigation strategies depends heavily on the morphology of the archetype analyzed (see Table 5.11). Strategies based on surface properties, such as increasing albedo, are most effective in compact fabrics (*High-Compact*); in these configurations, high reflectance prevents massive heat accumulation in surfaces most exposed to radiation (such as roofs), limiting radiative trapping within urban canyons. However, this benefit is lost in open and scattered layouts (*Scattered*).

In all the configurations tested, morphological alterations aimed at densification and increased anthropogenic heat act as vectors of deterioration, constantly leading to an amplification of the intensity of the UHI.

Finally, the persistent ineffectiveness—or in several cases the worsening thermal contribution—of vegetation highlights a critical structural limitation of the UWG model. By not integrating an active module for calculating the latent heat of evapotranspiration, the software models tree canopies exclusively as physical obstacles.

In addition to the monthly analysis, two limit days were isolated (July 28 for summer and December 15 for winter) to evaluate the model's response under peak and heat stress conditions (more details in the Appendix A.5). The following Table 5.12 summarizes the comparison between the two regimes.

The data confirm that the UHI intensity is strictly constrained by the morphology of the analyzed urban fabric and the observed seasonal regime.

Under summer conditions, the primary critical factor is driven by anthropogenic heat emissions, particularly in compact fabrics. Consequently, mitigation policies

Table 5.12: Comparison of thermal dynamics and critical factors between summer and winter regimes.

	Hot Day (July 28th)	**Cold Day (December 15th)**
Max Intensity ΔT	∼0.42 K (Low-Compact, Anthro. Heat)	∼1.40 K (High-Scattered, Morphology)
Dominant Factor	Anthropogenic Heat	Morphology
Critical Hours	Morning and evening transitions	Nighttime period
Impact of Albedo	Marginal daytime cooling	Almost neutral
Impact of Greenery	Slight local warming	Severe morning thermal penalty
Most Sensitive Archetypes	Low-Compact, Low-Scattered	High-Compact, High-Scattered
Most Stable Archetypes	High-Scattered	Low-Compact

in these contexts should focus on cutting thermal releases during evening hours. Increasing surface albedo represents the only strategy capable of triggering a daytime cooling dynamic, albeit with a marginal absolute thermal benefit.

In winter conditions, morphology becomes the dominant factor. Urban geometry (building height and Sky View Factor) dictates the fabric's capacity to trap nighttime heat, making high-density layouts (High-Compact and High-Scattered) particularly vulnerable to morphological alterations. In this context, it is also crucial to account for the winter penalty induced by vegetation, which can exacerbate morning thermal discomfort by blocking solar radiation.

Finally, low-density fabrics (Low-Compact and Low-Scattered) exhibit a dual behavior: while recording the most severe percentage sensitivity to morphological variations on a monthly scale, their absolute daily thermal variation remains more dampened. This finding suggests that future densification policies for suburban areas will need to carefully calibrate the engineering trade-off between land-use optimization and the triggering of new localized urban heat islands.

Chapter 6

Conclusion

This thesis has analysed the role of spatial discretisation in urban microclimate modelling, with particular reference to the simulation of the urban heat island (UHI) effect in district-level contexts, such as *Positive Energy Districts* (PED). The main objective was to assess the extent to which the choice of spatial units influences both the accuracy of the simulations and the representation of urban thermal patterns.

The tool used for the analyses, the *Urban Weather Generator* (UWG), although widely used, is based on average parameters derived from a preliminary discretisation phase. In its standard implementation, this process is carried out using a regular grid that does not reflect the functional units of the urban fabric and may introduce artefacts linked to geometric discretisation. To overcome this limitation, an approach based on Morphological Blocks (MB) has been proposed, in which the spatial units follow the boundaries of the road network, parameterised using a morphological database constructed in a GIS environment based on the Regional Topographic Database (DBTRE).

Model performance and validation

Validation against the ARPA Piemonte weather station (Consolata, hourly series 2024) showed that the MB configuration provides a systematic improvement in performance throughout the year. On an annual basis, the MB approach reduced the hourly RMSE from 1.182 K to 1.114 K (+5.77%) and the mean bias error (MBE) from +0.348 K to +0.263 K. The maximum gain was recorded in July, with a 9.42% reduction in RMSE, confirming the superiority of the MB approach in capturing heat trades during the summer months.

Analysis of two extreme events confirmed the model's suitability during the summer heatwave (RMSE = 0.802 K). In contrast, during the winter stagnation episode (December 2024), performance declined (RMSE = 1.528 K) due to the systematic positive bias caused by the model's reliance on a single rural station (Caselle).

Spatial representation of the UHI

At the district level, the two approaches produce comparable average results (a difference of just 0.029 K), but diverge drastically in terms of spatial distribution. The grid shows a standard deviation ($\sigma_G = 0.162$ K) more than double that of the blocks ($\sigma_{MB} = 0.074$ K). The dispersion ratio (σ_G/σ_{MB}) consistently exceeds 1.8, highlighting how the arbitrary cell boundaries introduce numerical noise that distorts the morphological signal.

Extreme cases such as Cell 50 confirm this distortion: the grid assigns an 80 per cent coverage (0.811) and a thermal emission of 123.46 W/m^2, overestimating the UHI by +0.774 K compared to the actual morphological blocks. Conversely, Cell 34 highlights the effect of *smoothing*, where the grid dilutes a dense *hotspot* of 1.68 K with the surrounding open areas, underestimating the local thermal risk. The robustness of this comparison was corroborated by a volumetric invariance test (discrepancy $< 0.4\%$), which rules out differences in total thermal mass as the cause of the discrepancies.

Sensitivity analysis

A sensitivity analysis of four morphological archetypes has shown that the effectiveness of mitigation strategies depends heavily on urban geometry.

Traffic emerges as the dominant contributor in compact urban fabrics, with an impact of up to +6% on the UHI. Surface albedo is particularly effective in dense contexts, where radiative trapping is significant. Densification systematically amplifies the UHI, with the highest sensitivity observed in low-density urban fabrics.

As regards vegetation, an increase in the green ratio does not produce appreciable benefits or may slightly worsen the nocturnal UHI. This result should not be interpreted as evidence of the ineffectiveness of urban greenery, but reflects a structural limitation of the UWG model, which does not include an explicit representation of evapotranspiration and therefore does not capture the latent heat fluxes associated with vegetation.

Limitations

The results highlight that spatial discretisation is a modelling choice with significant physical implications. Aligning computational units with the urban morphological structure helps to reduce geometric discretisation artefacts, improve the interpretability of the results, and make the simulated energy balance more robust.

In this context, the Morphological Block approach proves more effective than grid discretisation in representing the urban fabric, ensuring greater consistency of results without significantly increasing the model's complexity.

Despite the improvements introduced, the framework has structural limitations. The UWG model simplifies vegetation, does not dynamically represent anthropogenic heat, and is heavily dependent on the rural reference station.

Furthermore, the model does not simulate lateral advection between spatial units and operates on a single-layer representation of the urban canyon, limiting its ability to capture fine-scale phenomena. In this regard, interactions or couplings between the different cells are not yet taken into account: the simulations remain independent and are not coupled with one another.

A further limitation concerns the dependence on the quality of the input data: the performance of the MB approach is closely linked to the accuracy of the morphological database and could be reduced in contexts with less reliable data.

Finally, the difference in elevation between the observed measurements (roof-mounted sensor) and the simulated variable (air within the canyon) is an aspect that warrants further investigation, in order to understand whether and to what extent it contributes to the residual bias.

Future work

Various avenues of research could further enhance the proposed modelling framework, expanding its predictive capabilities and operational applicability.

A key area for improvement concerns the dynamisation of anthropogenic loads. The integration of heat profiles derived from *Big Data* on mobility or from real-time indicators of urban activity would help overcome the static nature of current profiles. This would better reflect seasonal variations in urban metabolism, likely correcting the *bias* towards overestimation observed during the summer months. To complement this development, a more granular characterisation of building types — including a wider range of construction eras and mixed-use developments — would refine the estimation of heat rejected into the *canyon* and of internal heat

gains.

Secondly, future research should focus on interoperability with energy simulation (*BES*). Urbanised EPW files generated using the MB approach provide the natural input for advanced energy analyses in *EnergyPlus*. This workflow would enable the quantification of the *cooling energy penalty* caused by the UHI and the assessment of the cost-benefit effectiveness of targeted mitigation strategies, such as *cool roofs* or high-density urban afforestation programmes.

A third crucial aspect concerns a more detailed examination of mesoclimate interactions. It would be advisable to assess how Turin's geographical context influences the local microclimate. This analysis is essential for a correct interpretation of winter *biases*, where large-scale forcings may override local morphological characteristics.

Finally, the methodology can be extended to the assessment of future climate scenarios. By applying the workflow based on morphological blocks to projected meteorological datasets (consistent with the IPCC pathways for 2050 and 2080), it will be possible to test the resilience of current mitigation strategies under the expected increased thermal stress. This development would provide a solid quantitative basis for adaptive urban planning and for the definition of resilient guidelines within the framework of *Positive Energy Districts*.

Bibliography

[1] Ministero degli Affari Esteri e della Cooperazione Internazionale. Agenda2030 e gli obiettivi di sviluppo sostenibile. https://www.esteri.it/it/politica-estera-e-cooperazione-allo-sviluppo/cooperaz_sviluppo/obiettivi-di-sviluppo-sostenibile/.

[2] intengine the engine for good. United nations sustainable development goals. https://intengine.com/sdgs.

[3] European Council. Fit for 55: making buildings in the eu greener. https://www.consilium.europa.eu/en/infographics/fit-for-55-making-buildings-in-the-eu-greener/.

[4] ENEA Agenzia nazionale per le nuove tecnologie. Tecnologie energetiche: la commissione ue approva la revisione del set-plan. https://www.efficienzaenergetica.enea.it/vi-segnaliamo/tecnologie-energetiche-commissione-ue-approva-la-revisione-del-set-plan.html.

[5] SET-Plan Temporary Working Group 3.2. SET-Plan ACTION n. 3.2 Implementation Plan: Europe to become a global role model in integrated, innovative solutions for the planning, deployment, and replication of Positive Energy Districts. Technical report, Joint Programming Initiative (JPI) Urban Europe, 2018. Available in PDF format at: https://jpi-urbaneurope.eu/wp-content/uploads/2021/10/setplan_smartcities_implementationplan-2.pdf.

[6] Wendelius Jennifer. Ped framework 3.0: A policy guide to advance positive energy districts in europe. https://dutpartnership.eu/news/ped-framework-30-policy-guide-advance-positive-energy-districts-europe.

[7] Ufficio federale dell'ambiente (UFAM). Ondate di calore in città. Report, National Centre for Climate Services (NCCS), 2018.

[8] Zhaoyang Qiu, Qiaoqiao Yong, Jiayuan Wang, Longhui Liao, and Bo Yu. A multi-objective optimization framework for performance-based building design considering the interplay between buildings and urban environments. *Energy Conversion and Management*, 315:118793, 2024.

[9] Turning cities planning actions for positive energy districts into success. `https://tips4ped.eu/`.

[10] Educational campuses as the drivers for positive energy districts. `https://www.eduped.eu/`.

[11] Erkinai Derkenbaeva, Solmaria Halleck Vega, Gert Jan Hofstede, and Eveline Van Leeuwen. Positive energy districts: Mainstreaming energy transition in urban areas. *Renewable and Sustainable Energy Reviews*, 153:111782, 2022.

[12] Paul Torcellini, Shanti Pless, Michael Deru, and Drury Crawley. Zero energy buildings: a critical look at the definition. Technical report, National Renewable Energy Laboratory (NREL), Golden, CO., 2006.

[13] Patxi Hernandez and Paul Kenny. From net energy to zero energy buildings: Defining life cycle zero energy buildings (lc-zeb). *Energy and Buildings*, 42(6):815–821, 2010.

[14] Mia Ala-Juusela, Tracey Crosbie, and Mari Hukkalainen. Defining and operationalising the concept of an energy positive neighbourhood. *Energy Conversion and Management*, 125:133–140, 2016.

[15] Dirk Ahlers, Patrick Driscoll, Håvard Wibe, and Annemie Wyckmans. Co-creation of positive energy blocks. In *IOP conference series: earth and environmental science*, volume 352, page 012060. IOP Publishing, 2019.

[16] Bronia Jablonska, Bart Roossien, GerritJan Ruijg, Huib Visser, Eric Willems, and Ernst-Jan Bakker. Energy neutral districts in 2050–the dutch approach. *International Journal of Sustainable Building Technology and Urban Development*, 3(3):151–157, 2012.

[17] Oscar Lindholm, Hassam Ur Rehman, and Francesco Reda. Positioning positive energy districts in european cities. *Buildings*, 11(1):19, 2021.

[18] Christoph Gollner. White paper – reference framework for positive energy districts and neighbourhoods, 2020. White Paper.

[19] World Meteorological Organization. Urban heat island. url/https://wmo.int/urban-heat-island.

[20] Claudia Calice, Carola Clemente, Agnese Salvati, Massimo Palme, and Luis Inostroza. Urban heat island effect on the energy consumption of institutional buildings in rome. In *IOP Conference Series: Materials Science and Engineering*, volume 245, page 082015. IOP Publishing, 2017.

[21] Agnese Salvati, Helena Coch Roura, and Carlo Cecere. Assessing the urban heat island and its energy impact on residential buildings in mediterranean climate: Barcelona case study. *Energy and Buildings*, 146:38–54, 2017.

[22] Valentino Sangiorgio, Francesco Fiorito, and Mattheos Santamouris. Development of a holistic urban heat island evaluation methodology. *Scientific reports*, 10(1):17913, 2020.

[23] Massimo Palme and Agnese Salvati. Uwg-trnsys simulation coupling for urban building energy modeling. 2018.

[24] Yiman Zhao, Xiaotian Ding, Ziyu Wu, Shi Yin, Yifan Fan, and Jian Ge. Impact of urban form on building energy consumption in different climate zones of china. *Energy and Buildings*, 320:114579, 2024.

[25] Jonathan Natanian, Francesco Guarino, Naga Manapragada, Abel Magyari, Emanuele Naboni, Francesco De Luca, Salvatore Cellura, Alberto Brunetti, and Andras Reith. Ten questions on tools and methods for positive energy districts. *Building and Environment*, 255:111429, 2024.

[26] Bruno Bueno Unzeta. *Study and prediction of the energy interactions between buildings and the urban climate*. PhD thesis, Massachusetts Institute of Technology, 2012.

[27] Massachusetts Institute of Technology (MIT). Urban weather generator. `https://urbanmicroclimate.scripts.mit.edu/uwg.php`.

[28] Bruno Bueno, Matthias Roth, Leslie Norford, and Reuben Li. Computationally efficient prediction of canopy level urban air temperature at the neighbourhood scale. *Urban climate*, 9:35–53, 2014.

[29] Aiko Nakano. *Urban weather generator user interface development: towards a usable tool for integrating urban heat island effect within urban design process*. PhD thesis, Massachusetts Institute of Technology, 2015.

[30] Long He, Xiao-Wei Geng, Hong-Yuan Huo, Yi Lian, Qianrui Xi, Wei Feng, Min-Cheng Tu, and Pei Leng. Simulation of urban thermal environment based on urban weather generator: Narrative review. *Urban Science*, 9(7):275, 2025.

[31] Hiba Hamdi, Laure Roupioz, Thomas Corpetti, Xavier Briottet, and Antoine Lefebvre. Evaluation of urban weather generator for air temperature and urban heat islands simulation over toulouse (france). In *2023 Joint Urban Remote Sensing Event (JURSE)*, pages 1–4. IEEE, 2023.

[32] Alessia Boccalatte, Marco Fossa, Martin Thebault, Julien Ramousse, and Christophe Ménézo. Mapping the urban heat island at the territory scale: An unsupervised learning approach for urban planning applied to the canton of geneva. *Sustainable cities and society*, 96:104677, 2023.

[33] Agnese Salvati, Massimo Palme, and Luis Inostroza. Key parameters for urban heat island assessment in a mediterranean context: A sensitivity analysis using

the urban weather generator model. In *IOP Conference Series: Materials Science and Engineering*, volume 245, page 082055. IOP Publishing, 2017.

[34] Paria Saadatjoo, Hamed Moradi, Mohammad Hamdan, Mahmoud Murtala Farouq, and Parham A Mirzaei. On the oversimplification of neighborhood impact in urban microclimate and building energy models. *Building and Environment*, 283:113301, 2025.

[35] Gregorio Borelli, Ilaria Ballarini, Vincenzo Corrado, Andrea Gasparella, and Giovanni Pernigotto. Assessment and mapping of the urban heat island effect: a preliminary analysis on the impact on urban morphology for the city of turin, italy. In *Building Simulation Applications BSA 2024: 6th IBPSA-Italy Conference Bozen-Bolzano, 26th–28th June 2024*, pages 525–531. bu, press-Bozen-Bolzano University Press, 2025.

[36] Qingyu Li, Genyu Xu, and Ziqi Gu. A novel framework for multi-city building energy simulation: Coupling urban microclimate and energy dynamics at high spatiotemporal resolutions. *Sustainable Cities and Society*, 113:105718, 2024.

[37] Komi Bernard Bedra, Jian Zheng, Jiayu Li, Zhaoqian Sun, and Bohong Zheng. Automating microclimate evaluation and optimization during urban design: A rhino–grasshopper workflow. *Sustainability*, 15(24):16613, 2023.

[38] Serena Falasca, Virgilio Ciancio, Ferdinando Salata, Iacopo Golasi, Federica Rosso, and Gabriele Curci. High albedo materials to counteract heat waves in cities: An assessment of meteorology, buildings energy needs and pedestrian thermal comfort. *Building and environment*, 163:106242, 2019.

[39] Sustainability Directory. Urban albedo. `https://climate.sustainability-directory.com/term/urban-albedo/`.

[40] Ente Italiano di Normazione . *UNI 10339:1995. Impianti aeraulici a fini di benessere. Generalità, classificazione e requisiti.* Milano, Italia, 1995.

[41] Ente Italiano di Normazione . *UNI/TS 11300-1:2014. Prestazione energetica degli edifici - Parte 1: Determinazione del fabbisogno di energia termica dell'edificio per il riscaldamento ed il raffrescamento.* Milano, Italia, 2014.

[42] Ente Italiano di Normazione . *UNI EN 15193-1:2017. Energy performance of buildings - Energy requirements for lighting.* Milano, Italia, 2017.

[43] Comitato Torino Respira, 2023.

[44] ARPA Piemonte, 2024.

[45] Oleg A Alduchov and Robert E Eskridge. Improved magnus form approximation of saturation vapor pressure. *Journal of Applied Meteorology (1988-2005)*, pages 601–609, 1996.

[46] DG Erbs, SA Klein, and JA Duffie. Estimation of the diffuse radiation fraction for hourly, daily and monthly-average global radiation. *Solar energy*, 28(4):293–302, 1982.

[47] William F Holmgren, Clifford W Hansen, and Mark A Mikofski. pvlib python: A python package for modeling solar energy systems. *Journal of Open Source Software*, 3(29):884, 2018.

[48] Ibrahim Reda and Afshin Andreas. Solar position algorithm for solar radiation applications. *Solar energy*, 76(5):577–589, 2004.

[49] Vincenzo Corrado, Ilaria Ballarini, and Stefano Paolo Corgnati. Reference buildings for energy policy analysis of the national residential building stock. Technical report, Politecnico di Torino, 2014. TABULA Project.

Appendix A

Supplementary Material and Tabular Data

This appendix contains the detailed data, maps and numerical results that support the main chapters of the thesis.

A.1 Urban Heat Island Evidence

This section provides experimental evidence of the Urban Heat Island (UHI) effect in Turin, which serves as the physical basis for the subsequent numerical simulations. Figure A.1 illustrates the annual average diurnal temperature profiles, showing the divergence between the urban station (Consolata) and the rural reference (Caselle). The characteristic nocturnal heat retention of the urban fabric is further detailed in the monthly intensity heatmap (Figure A.2), which identifies the critical periods of thermal stress throughout the year.

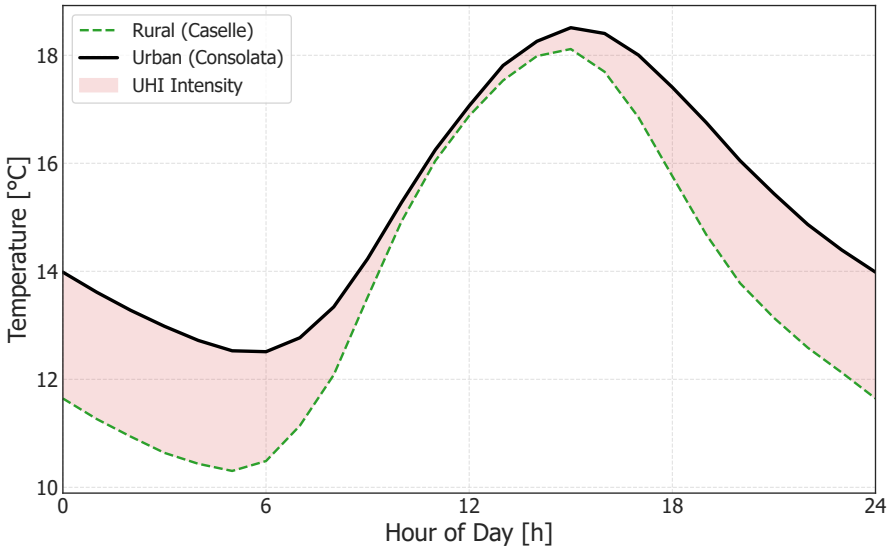


Figure A.1: Experimental evidence of the UHI effect in Turin: hourly temperature comparison between urban (Consolata) and rural (Caselle) weather stations (Annual average).

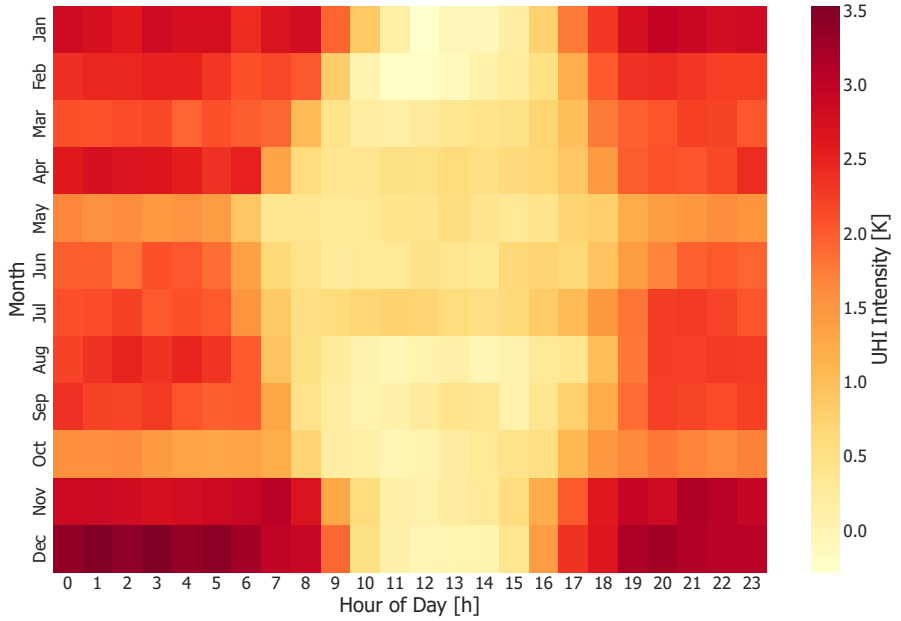


Figure A.2: Spatiotemporal heatmap of UHI intensity [K] in Turin, showing the hourly temperature delta between urban and rural stations across the months.

A.2 Mapping and Discretisation of the Urban Fabric

This section contains the maps relating to the spatial discretisation used to calculate the morphological parameters in the Turin study area.

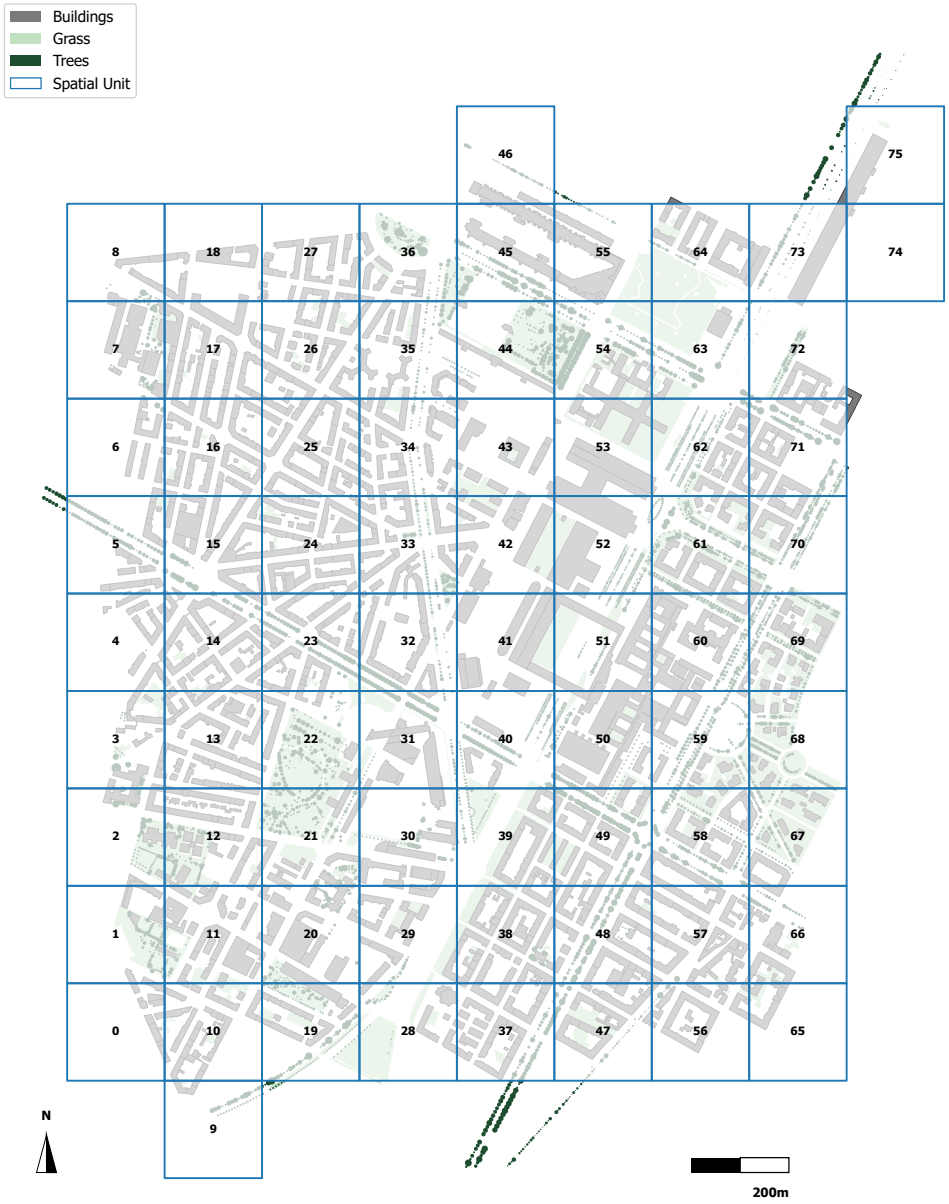


Figure A.3: Grid discretisation based on a 200 × 200 m resolution.

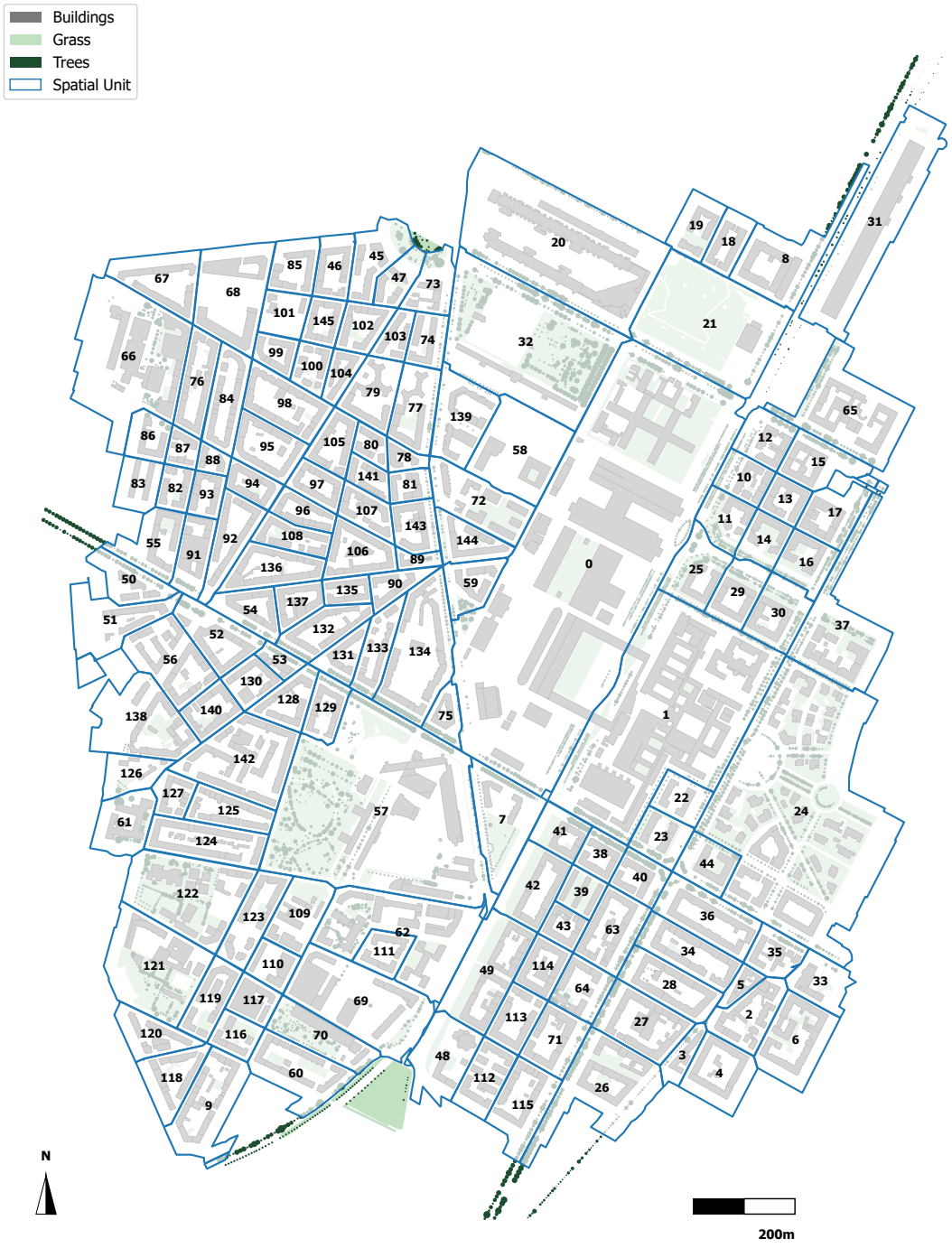


Figure A.4: Morphological blocks discretisation based on the urban fabric.

A.3 Validation Results

The tables below show the error metrics (RMSE, MBE) calculated for the various positions of the spatial unit carrying the reference station.

Table A.1: MAUP Validation results: Monthly and annual statistical comparison (RMSE and MBE) between morphological blocks (MB) and three grid-based discretizations (NC, 200m, 500m).

Month	**RMSE [K]**				**MBE [K]**			
	MB	G_{NC}	G_{200}	G_{500}	**MB**	G_{NC}	G_{200}	G_{500}
January	1.422	1.508	1.553	1.413	+0.279	+0.499	+0.644	−0.024
February	1.213	1.297	1.333	1.172	+0.361	+0.499	+0.508	+0.090
March	0.956	0.989	1.018	1.046	−0.092	+0.010	−0.021	−0.379
April	1.183	1.213	1.237	1.269	+0.024	+0.056	+0.004	−0.341
May	0.950	0.988	0.953	0.959	+0.215	+0.230	+0.153	−0.157
June	0.994	1.037	0.999	0.965	+0.285	+0.272	+0.257	−0.173
July	0.879	0.970	0.961	0.879	+0.216	+0.227	+0.242	−0.291
August	1.398	1.496	1.475	1.160	+0.818	+0.891	+0.888	+0.316
September	1.001	1.057	1.044	1.037	+0.256	+0.262	+0.207	−0.151
October	0.738	0.779	0.778	0.798	+0.134	+0.182	+0.109	−0.217
November	1.381	1.503	1.487	1.325	+0.436	+0.627	+0.640	+0.071
December	1.254	1.350	1.409	1.262	+0.221	+0.419	+0.550	−0.090
ANNUAL	**1.114**	**1.182**	**1.187**	**1.107**	**+0.263**	**+0.348**	**+0.348**	**-0.112**

Note: MB refers to discretisation by morphological blocks; G_{NC} refers to the non-centred grid; G_{200} and G_{500} to grids centred on the weather station, with dimensions of 200×200 m and 500×500 m.

A.4 Mapping of urban heat island

This section presents the spatial distribution of the urban heat island effect in relation to the physical features present.

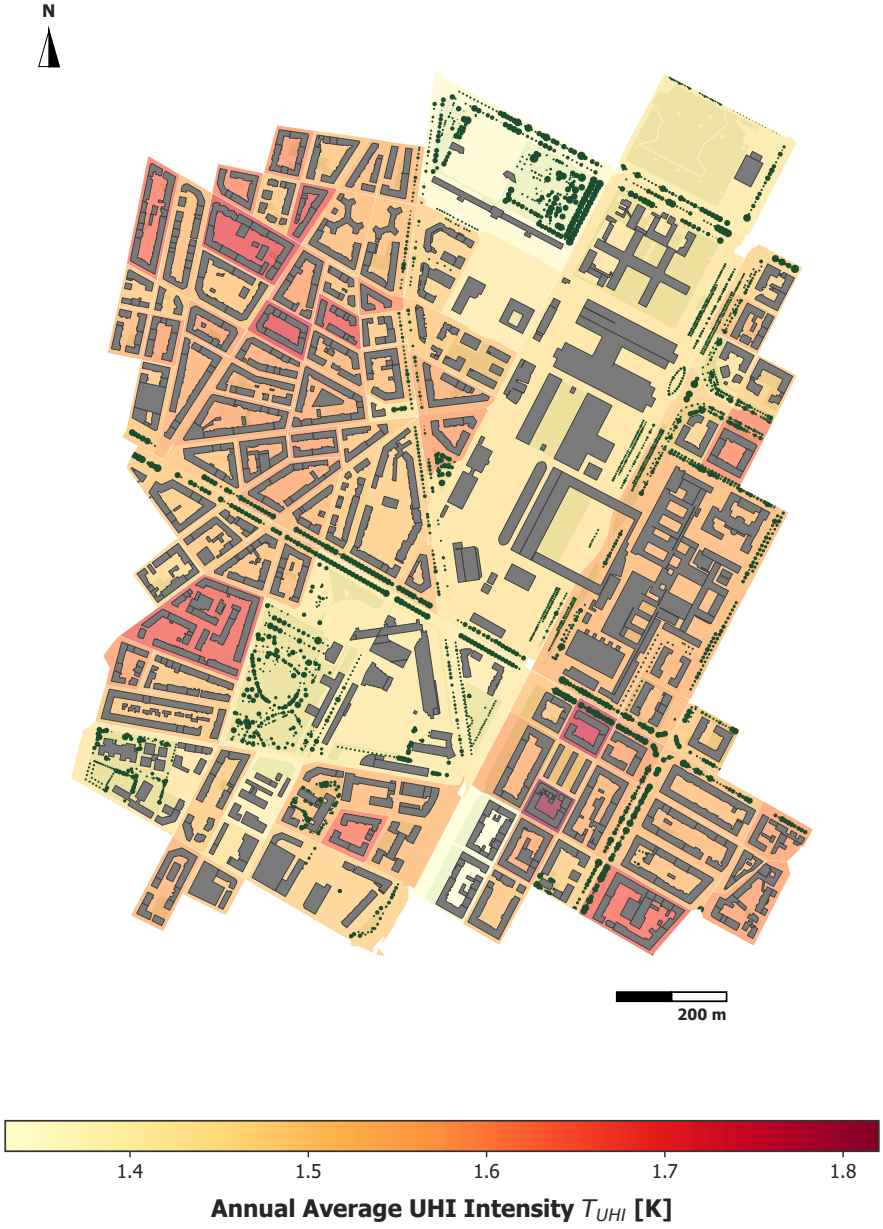


Figure A.5: Spatial mapping of the average annual UHI in the Core Area.

A.5 Thermal Sensitivity Data

This section presents the point-by-point values for the intensity of the *Urban Heat Island* (UHI) and the relative impact of mitigation strategies for the two critical days.

A.5.1 Summer Schedule (28 July)

Table A.2: Thermal sensitivity analysis summary (July 28th - Extreme Heat).

Archetype	Strategy	Peak [K]	Night [K]	Day [K]	24h [K]	Mitigation [%]
High-Compact	Albedo	−0.074	−0.032	−0.051	−0.044	+1.15%
	Greenery	−0.010	+0.002	−0.001	−0.000	−0.08%
	Anthro. Heat	+0.317	+0.017	+0.049	+0.037	−0.61%
	Morphology	+0.019	+0.013	+0.002	+0.006	−0.47%
High-Scattered	Albedo	−0.036	−0.015	−0.028	−0.023	+0.56%
	Greenery	−0.013	+0.003	−0.003	−0.000	−0.13%
	Anthro. Heat	+0.046	+0.016	+0.024	+0.021	−0.63%
	Morphology	−0.040	+0.026	−0.011	+0.002	−0.98%
Low-Compact	Albedo	−0.069	−0.042	−0.010	−0.022	+1.51%
	Greenery	+0.070	+0.035	−0.013	+0.004	−1.24%
	Anthro. Heat	+0.420	+0.087	+0.066	+0.074	−3.10%
	Morphology	+0.103	+0.054	+0.017	+0.031	−1.93%
Low-Scattered	Albedo	+0.011	−0.005	−0.000	−0.002	+0.25%
	Greenery	+0.063	+0.035	−0.012	+0.005	−1.57%
	Anthro. Heat	+0.288	+0.084	+0.045	+0.060	−3.69%
	Morphology	+0.264	+0.209	−0.001	+0.077	−9.15%

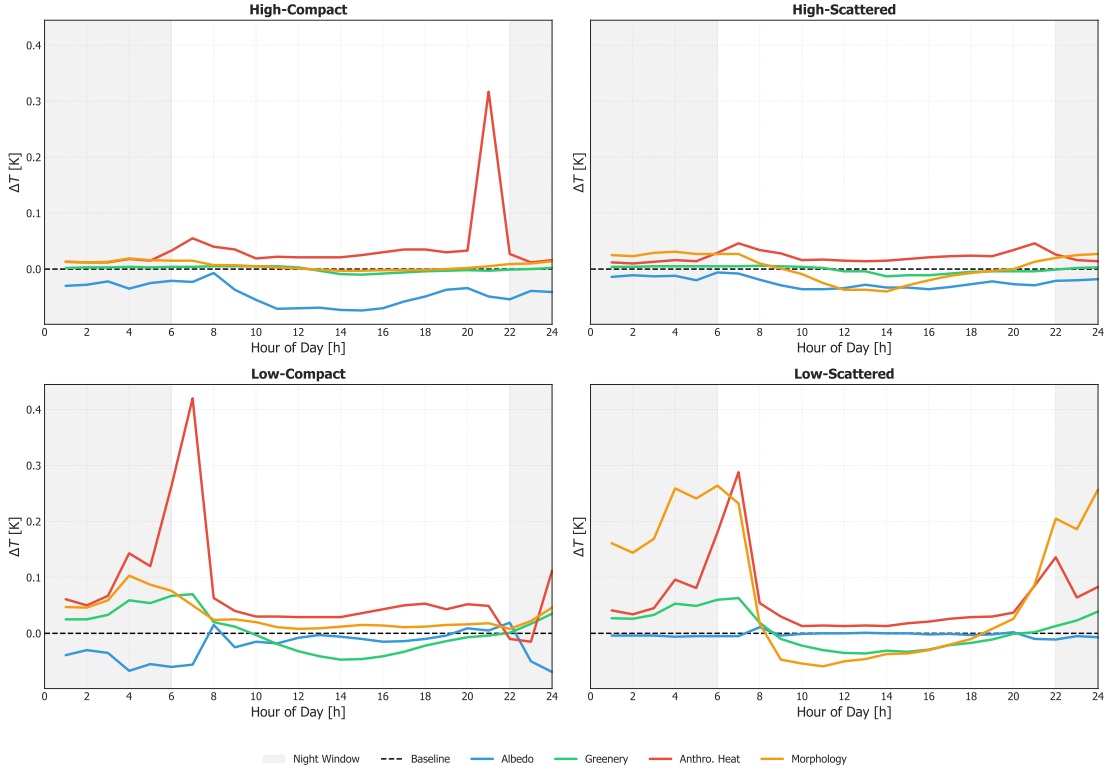


Figure A.6: Hourly thermal profile variations during the extreme heat event (July 28th).

A.5.2 Winter Schedule (15 December)

Table A.3: Thermal sensitivity analysis summary (December 15th - Extreme Cold).

Archetype	Strategy	Peak [K]	Night [K]	Day [K]	24h [K]	Mitigation [%]
High-Compact	Albedo	+1.203	+0.130	−0.017	+0.038	−2.68%
	Greenery	+1.216	+0.137	+0.000	+0.051	−2.81%
	Anthro. Heat	+1.228	+0.149	+0.033	+0.076	−3.07%
	Morphology	+1.238	+0.157	+0.013	+0.067	−3.21%
High-Scattered	Albedo	−0.038	−0.001	−0.013	−0.009	+0.05%
	Greenery	−0.768	+0.003	−0.050	−0.030	−0.09%
	Anthro. Heat	+0.386	+0.015	+0.080	+0.055	−0.39%
	Morphology	+1.399	+0.466	+0.196	+0.297	−12.01%
Low-Compact	Albedo	+0.072	−0.000	−0.007	−0.004	+0.02%
	Greenery	+0.012	+0.007	+0.002	+0.004	−0.20%
	Anthro. Heat	+0.125	+0.021	+0.047	+0.038	−0.55%
	Morphology	+0.058	+0.040	+0.021	+0.028	−1.03%
Low-Scattered	Albedo	−0.007	−0.000	−0.002	−0.001	+0.02%
	Greenery	+0.040	+0.018	+0.000	+0.007	−0.48%
	Anthro. Heat	+0.262	+0.031	+0.067	+0.053	−0.83%
	Morphology	+0.122	+0.068	+0.023	+0.040	−1.84%

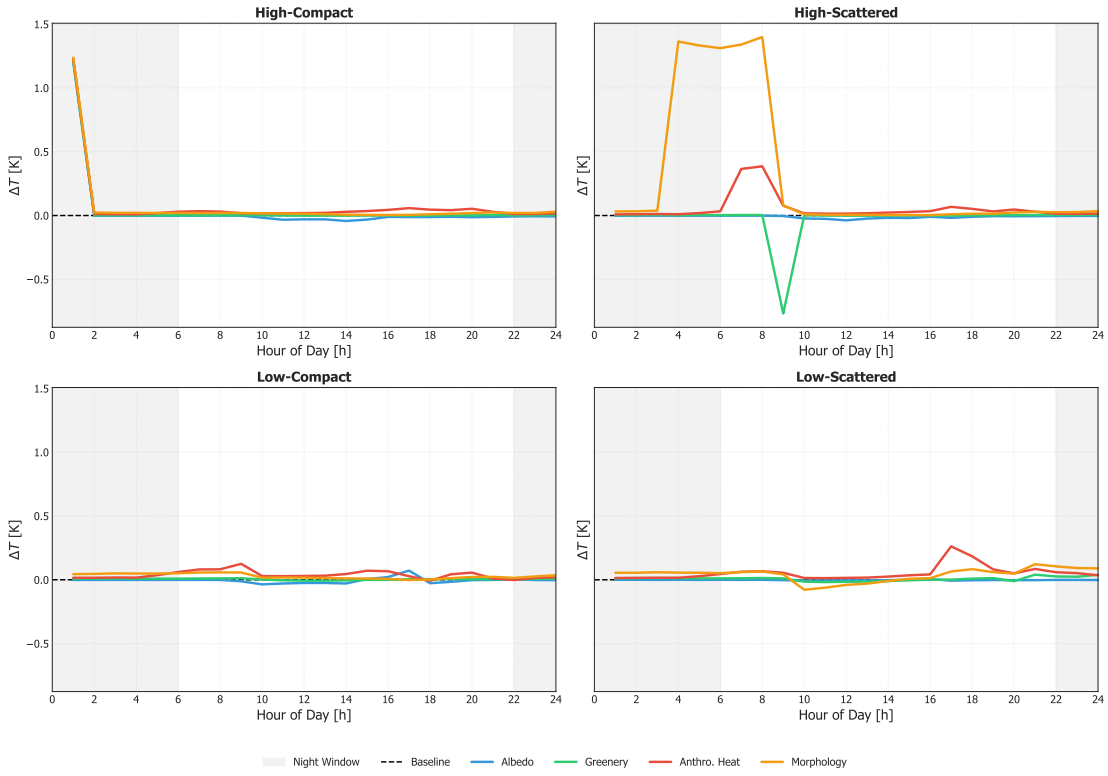


Figure A.7: Hourly thermal profile variations during the extreme cold event (December 15th).